Title	DARK MATTER SEARCH WITH CaF2 SCINTILLATOR
Author(s)	硲, 隆太
Citation	大阪大学, 1998, 博士論文
Version Type	VoR
URL	https://doi.org/10.11501/3143742
rights	
Note	

DARK MATTER SEARCH WITH CaF$_2$ SCINTILLATOR

RYUTA HAZAMA

DISSERTATION IN PHYSICS

THE OSAKA UNIVERSITY
GRADUATE SCHOOL OF SCIENCE
TOYONAKA, OSAKA

January 1998

ACKNOWLEDGMENTS

Contents

LIST OF TABLES

LIST OF ILLUSTRATIONS

ABSTRACT ∘

A segmented CaF_2 detector equipped by active and passive shields has been developed to search for rare and tiny signals from hypothetical particles of which generic name is WIMPs (Weakly Interacting Massive Particles) by measuring elastic scattering from F nuclei in the scintillators. CaF_2 scintillators are surrounded by 4π active shield with active light guides and CsI(Tl) scintillators. The CaF_2 scintillator-complexes is a key detector, not only for having the fluorine target with large cross section for spin coupled WIMPs, but also for 4π active shield from huge backgrounds in the low energy region of the present concerns.

The nuclear recoil energy in the dark matter - nucleus scattering is as small as $E_R = 0 \sim 100$keV and the signal is very rare because the dark matter interaction is weak and the flux is small. Therefore direct measurements of WINPs led us to develop a low-noise, low-background and large-volume detector system 'ELEGANT VI'(ELEctron- GAmma- ray- Neutrino- Telescope VI) whose naming is partly historical. This thesis describes mainly the background reduction in the low energy region, in which the background is not so clear compared with that of a few MeV region for the study of the double beta decays, and so on.

This system has three major characteristics for background rejection in the low energy region. First, 4π active shield; the central CaF_2(Eu) crystal has light guide of pure CaF_2 crystal which are also sensitive to gamma rays. This design is quite effective to reduce the background from PMTs. Secondly, segmentation; CaF_2 detectors are divided into small segments with dimension of 45mm cube. True event due to dark matter scattering is confined in a small region. Thirdly, hermeticy & energy loss; CaF_2 and CsI were chosen to make active shield as hermetic as possible since no container is necessary due to non-hygroscopic. Besides, the active veto is effective even for X-rays, which has been lossed in energy at housing in the case of NaI. As for passive shield, two independent systems has been installed. The first is a conventional photon attenuation shield of lead and copper. The second is a Cd sheet, a LiH-loaded paraffin, and a water tank moderator loaded with H_3BO_3.

In order to treat properly the low energy signal, high gain amplifiers with integration circuit and low noise discriminators have been developed. The energy threshold of CaF_2

detector is below 1keV. The efficiency of the low energy signal has been determined by using the signal from a light emitting diode(LED). It is found that the detector system is sensitive to 2keV signal with 40% efficiency.

The scintillation efficiency of recoiling calcium and fluorine nuclei produced in the $CaF_2(Eu)$ crystal was measured in the 25-91 keV and 53-192 keV recoil energy intervals, respectively. The scintillation efficiency was found to be 11~ 20%, and 9~ 23% for F and Ca respectively. This measurement is a key to derive the limit on the existence of the dark matter.

The full operation of ELEGANT VI was carried out at the Osaka University sea-level laboratory. Our detector can set similar limit as DAMA(BPRS) Collaboration at Gran Sasso underground laboratory on the upper limit of the spin coupled dark matters. These measurements demonstrate that passive shielding, used for photon attenuation, act as a strong neutron source, with the neutrons being produced primarily by cosmic ray muon interactions within the shields. The sea-level measurements makes it possible to evaluate the effect of these cosmic-ray induced background.

It is noted that ELEGANT VI system has been developed not only for the dark matter search, but also for studying the $\beta\beta$ decays of ^{48}Ca simultaneously.

Chapter 1

INTRODUCTION

1.1 Dark Matter

1.1.1 Evidence for dark matter

There is perhaps no current problem of greater importance to astrophysics and cosmology than that of "dark matter". The controversy, as the name implies, is centered around the notion that there may exist an enormous amount of matter in the Universe which does not emit detectable quantities of electromagnetic radiation; it nevertheless manifests itself through its gravitational pull. Evidence for this kind of dark matter was first collected in the 1920's and 30's, but its existence became widely accepted only in the 1970's [1]. Its presence is inferred indirectly from the motions of astronomical objects, specifically stellar, galactic, and galaxy cluster/supercluster observations. The least controversial evidence comes from "galactic rotation curves". Here one measures the rotational velocity of globular clusters, hydrogen clouds, or other objects, around spiral galaxies. Assuming that these objects are in stable orbits, around spiral galaxies. Kepler's law tells us that the rotational velocity v_{rot} should decrease $\propto 1/\sqrt{r}$ at large distance r to the center of the galaxy, if the mass of the galaxy is concentrated in its visible part. However, observationally all rotation curves become essentially independent of r at large r, out to the largest observable distances; this implies that the mass inside the radius r grows linearly with r, i.e. the mass density drops $\propto 1/r^2$ [2]. There is also mounting evidence for dark matter in elliptical galaxies as well as clusters of galaxies coming from X-ray observations of these objects. Also, direct evidence has been obtained through the study of gravitational lenses.

In theory, we believe there is much more matter because 1) inflation tells us so (and

there is at present no good alternative to inflation) and 2) our current understanding of galaxy formation only makes sense if there is more than matter than we see. One can also make a strong case for the existence of non-baryonic dark matter in particular. The recurrent problem with baryonic dark matter is that not only is it very difficult to hide baryons, but the standard model of primordial nucleosynthesis would have to be discarded if all of the dark matter is baryonic.

Before embarking on the subject of dark matter, it will be usefull to review the relevant quantities from the standard big bag model. In a Friedmann-Robertson-Walker Universe, the expansion rate of the Universe (the Hubble parameter) is related to the energy density ρ and curvature constant k by

$$H^2 = (\frac{\dot{R}}{R})^2 = \frac{8\pi G}{3}\rho - \frac{k}{R^2} \qquad (1.1)$$

assuming no cosmological constant, where $k = \pm 1, 0$ for a closed, open or spatially flat Universe, and R is the cosmological scale factor. When $k=0$, the energy density takes its "critical" value,

$$\rho = \rho_c \equiv \frac{3H^2}{8\pi G} = 1.9 \times 10^{-29} h_0^2 \text{g/cm}^3 = 11 h^2 \text{keV/cm}^3 \simeq 1 \times 10^{-5} \text{GeV/cm}^3 \qquad (1.2)$$

where distances are measured in parsecs (1 pc= 3.09×10^{18}cm = 3.26 light year), and $h_0 \approx 0.5$-1 is the Hubble parameter H in units of 100 km/s/Mpc. The cosmological density parameter is defined by $\Omega \equiv \rho/\rho_c$ and by rewriting eq. (1.1) we can relate k to Ω and H by

$$\frac{k}{R^2} = (\Omega - 1)H^2 \qquad (1.3)$$

so that $k = +1, -1, 0$ corresponds to $\Omega > 1, < 1, = 1$. If $\Omega = 1$, then we know two things: Dark matter exists, since we don't see $\Omega = 1$ in luminous objects, and most (at least 90%) of the dark matter is not baryonic. The latter conclusion is a result from big bang nucleosynthesis (BBN) [3], which constrains the baryon-to-photon ratio $\eta = n_B/n_\gamma$ to

$$1.4 \times 10^{-10} < \eta < 3.8 \times 10^{-10} \qquad (1.4)$$

which corresponds to a limit on Ω_B

$$0.005 < \Omega_B < 0.09 \qquad (1.5)$$

for $0.4 \sim< h_0 \sim< 1.0$ [4]. Thus $1 - \Omega_B$ is not only dark but also non-baryonic. If the mass density was essentially that observed in stars and other luminous matter, the epoch of structure formation would be very short, theoretically requiring fluctuations in the microwave background to be much larger than observed by COBE. In fact $\Omega = 1$ is the only stable value for most cosmological models.

2

As the minimum amount of baryons allowed in the universe by BBN is larger than the luminous mass, dark baryons are needed. On the other hand, the large values of Ω at increasing scales, certainly larger than the maximum Ω_B permitted by BBN, imply that non-baryonic dark matter is needed in proportions much larger than the baryonic dark matter. These are shown in Fig. 1-1 [5].

Fig. 1-1 Measured effective values of Ω versus scale.

1.1.2 Dark matter candidates

Dark matter (DM) candidates are usually split into two broad categories, with the second category being further sub-divided: (see Fig. 1-2 [5])

1) Baryonic

2) Non-Baryonic

i) hot dark matter (HDM)

ii) cold dark matter (CDM),

depending on their respective masses and speeds. CDM candidates have relatively large mass and travel at slow speeds (hence "cold"), while HDM candidates include minute-mass, rapidly moving (hence "hot") particles.

Dark Matter

$\Omega < 0.1$

$\Omega > 0.1$ **large**

+ COBE
scale structure

Baryonic

Non baryonic

gas

clumped H$_2$?

exotic
particle

?

dust

MACHOs

thermal equilibrium

non−thermal

light ν

WIMPs

Axions

?
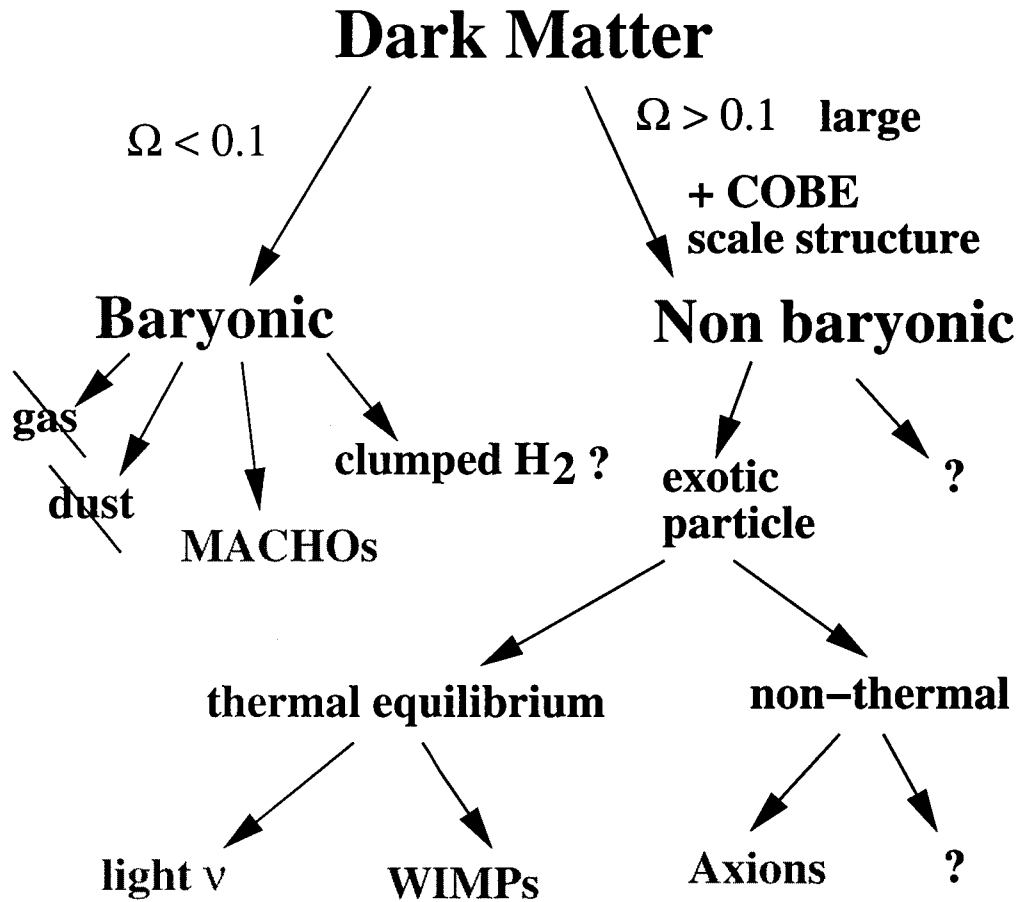
Fig. 1-2 Nature of dark matter.

1) Baryonic

Accepting the dark matter hypothesis, the first choise for a candiate should be something we know to exist, baryons. The main baryonic candidates are massive compact halo objects (MACHOs) [6]. These include, for example, brown dwarfs, jupiters, steller black-hole remnants, white dwarfs, and neutron stars.

4

The gravitational lensing searches for Massive Compact Halo Objects (MACHOs) and the searches for dark matter particles in the halo of our galaxy are complementary strategies. The present running experiments are listed in Table 1-1. The observed order of masses of MACHOs are $0.08M_\odot$ and $10^{-3}M_\odot$ so far (The Jupitor and Earth correspond to $\sim 10^{-3}M_\odot$ and $\sim 3 \times 10^{-6}M_\odot$, respectively). The future search are mainly planning to detect the mass order of $10^{-7}M_\odot$(Earth type) and $10^4M_\odot$(the Black Hole type) in the direction of our Galactic-Center [7]. Up to now the search towards the galactic buldge, the Large Magellanic Cloud and M31 have been carried out.

Table 1-1 The gravitational lensing searches for MACHOs

Collaboration	Location	telescope	CCD camera
MACHO	Australia	1.27 m	3x3x4cm(0.7x0.7°)
	Chile	1.8 m (in 2000)	
EROS	Chile	0.4 m	1x0.4°
		1.0m	Large CCD in preparation
OGLE	Chile	1.3 m	Large CCD
MOA	New Zealand	1.3 m	1.6x0.7°

Fully taking into account the current observational and theoretical uncertainties, the fraction of MACHOs can be as high as 100% of the halo or as low as 10%. Because the statistics are still too poor to securely eliminate MACHOs as the primary halo component. Conversely, the combination of these MACHO results with the rest of the cosmological evidence favors a low value for the MACHO fraction [8].

Other, less popular, baryonic possibilities, include fractal or specially conditioned neutral-hydrogen or molecular clouds [9].

2) Non-Baryonic

The rest of the dark matter candidates are nonbaryonic. This categorization has important ramifications for structure formation, and studies of galaxy formation may provide clues as to whether the dark matter is hot or cold. Recent simulation on the development of the structure of the universe in various scale suggests strongly relevance of the cold dark matter [10]. Hot dark matter cannot cluster on galaxy scales until it has cooled to nonrelativistic speeds, and so gives rise to a considerably different primordial fluctuation spectrum [11]. The measurements of primordial fluctuations in the cosmic microwave background radiation energy by

5

COBE combined with other measurements allows us to estimate the power spectrum of fluctuations in the Universe from Gigaparsec scale down to Megaparsec scale. There seems to be now a consensus that a simple cold dark matter canont match the power spectrum on both large and small scales. Either there is too little power on large scales or too much power on small scales. In vogue recently has been the idea that the mixed dark matter scenario woth 70% cold dark matter and 30% neutrinos (in energy density) might fit all scales. As a result we would have;

$$\Omega_{CDM} = 0.65, \Omega_{HDM} = 0.30 \text{ and } \Omega_{baryons} = 0.05 \qquad (1.6)$$

Although this fit is in agreement with all the data, one must recognise that it is now a three parameter fit which sounds a little bit artificial and suspicious. There are no known deep reasons to have $\Omega_{CDM}, \Omega_{HDM}$ and $\Omega_{baryons}$ of the same magnitude.

i) hot dark matter (HDM)

The leading hot dark matter candidates is a light neutrino. If a light $(m_\mu \sim< 100$ eV) Majorana neutrino exists, its cosmological density would be $\Omega_\mu h^2 \simeq (m_\mu/93$ eV). However, N-body simulations of structure formation in a universe dominated by hot dark matter do a poor job of reproducing the observed structure [11]. If we take $\Omega_\mu = 0.30$ seriously, the prime cadidate is a 7 eV neutrino. Present limits from direct mass measurements are shown in Table 1-2 [12].

Table 1-2 Present neutrino mass limits.

	Method	Reaction	Limits(95%C.L.)
ν_e	Tritium decay endpoint	T$\rightarrow^3$He+e+ν_e	7.2 eV
ν_μ	π momentum +mass	$\pi_{stop} \rightarrow \mu + \nu_\mu$	270 keV
ν_τ	τ decay endpoint	$\tau \rightarrow 5\pi^\pm + \nu_\tau$	31 MeV

Although ν_e, ν_μ and ν_τ are all compatible with 7 eV mass, there is a theoretical prejudice that the ν_τ would be the heaviest and then the preferred candidate.

ii) cold dark matter (CDM),

The nonbaryonic cold dark matter candidates are basically elementary particles which has not yet been discovered. The two leading candidates from particle theory are the axions [13], which arises in the Peccei-Quinn solution to the strong-CP problem, and a weakly interacting massive particles (WIMPs), which may arise in supersymmetric (or other) extensions of the standard model [14]. Those discussed most often are heavy fourth-generation

Dirac and Majorana neutrinos and the neutralino and sneutrino in supersymmetric models. WIMPs masses are typically in the range fro 10 GeV to few TeV, and they have interactions with ordinary matter which are characteristic of the weak interactions. The most promising WIMP candidate is the neutralino.

The study of these ideas are no longer exclusively the domain of theorists; there are now a number of experiments aimed at discovery of axions and WIMPs. If axions populate the Galactic halo, they can be converted to photons in resonant cavities immersed in strong magnetic fields. An experiment to search for axions in this fashion is currently being carried out. If WIMPs populate the halo, they can be detected either directly in low background laboratory detectors or indirectly via observation of energetic neutrinos from WIMPs which have accumulated and then annihilated in the Sun and/or Earth.

1.2 WIMP search

I will focus here on the WIMP search and briefly outline the status of the experiments. It is likely that the cold dark matters are unknown particles that interact weakly with matters. Such particles are classified by interactions of vector and axial vector couplings. So far experiments have far below the necessary sensitivity to exclude the dark matters that have axial vector coupling with matters (spin coupled dark matters), while ultrapure germanium detectors have already ruled out vector coupled one like heavy Dirac neutrino [15]. One reason is that one has to use nuclei that have nonzero spin to search for spin coupled dark matters which constrains materials to be used as the detector. Another reason is that the cross section of vector coupled dark matters with a nucleus are coherent sum of scatterings with nucleons in the nucleus (see Fig.1-3(a)). The coherence, however, is not expected for the cross section of spin coupled dark matters (see Fig.1-3(b)). Among such spin coupled dark matters, the lightest neutral super partner (neutralino) is one of the promising candidates, since the supersymmetry seems to be quite attractive theory beyond the standard model. These considerations make the search for the spin coupled dark matters quite interesting. Search for spin coupled dark matters has been made firstly by using NaI scintillators of ELEGANT V [16].
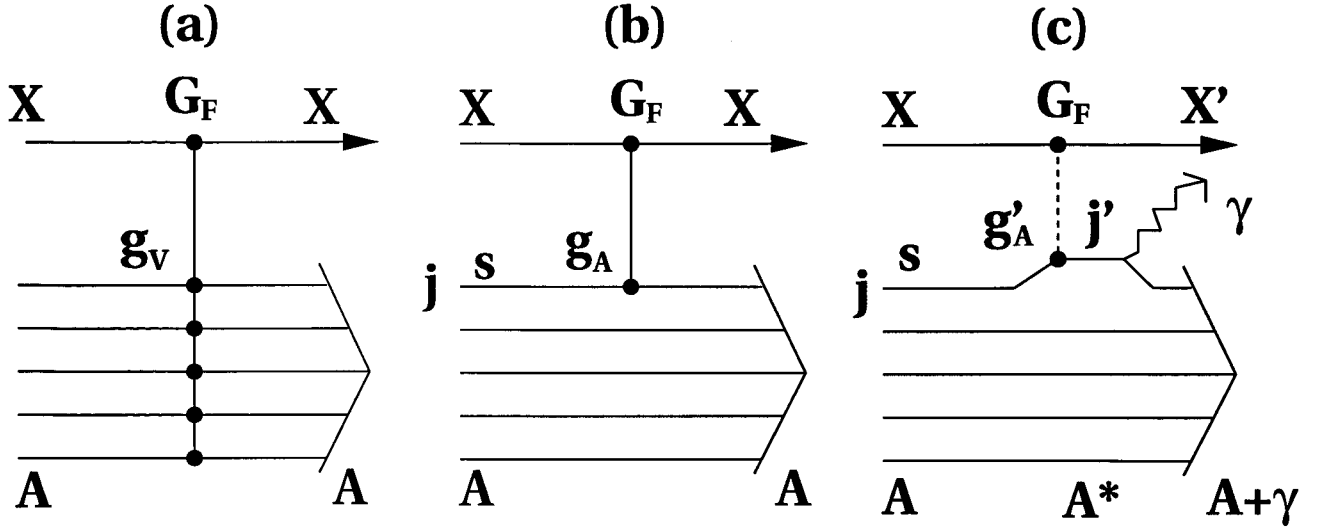
Fig. 1-3 Scattering of WIMP (X) from a nucleus A. (a) Elastic scattering of vector-coupled dark matter. (b) Elastic scattering of axial-vector (spin-coupled) dark matter interacting with one valence nucleon in j orbit. (c) Inelastic scattering of axial-vector (spin-coupled) dark matter, exciting one valence nucleon from j to j' orbits.

Up to now the experimental teams interested in the direct detection are adopting five different strategies, which is shown in Fig. 1-4 [5]. And the present WIMP-hunting experiments are summarized in Table 1-3 [17].
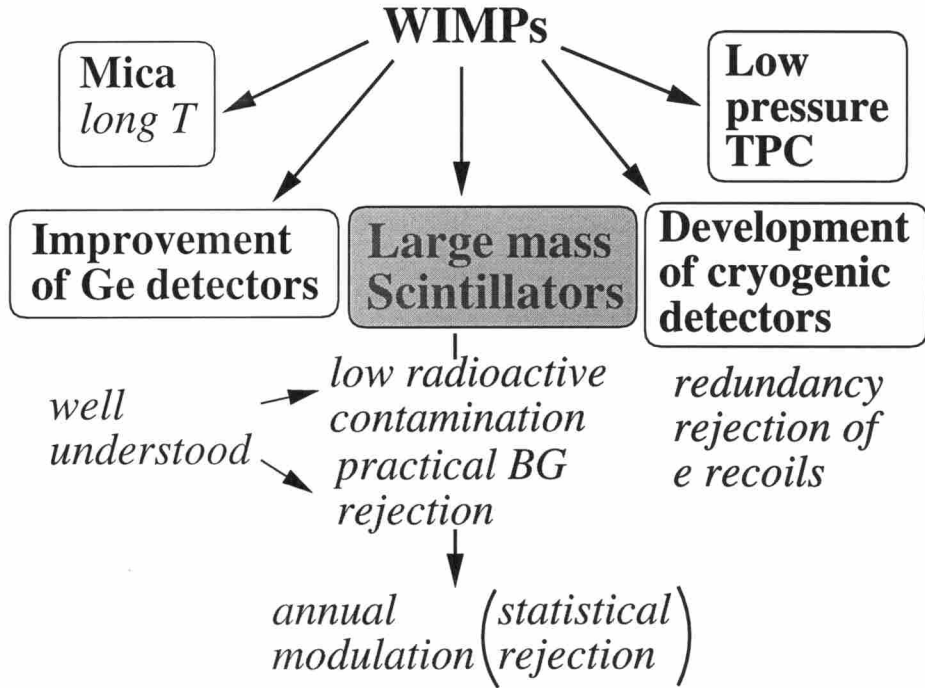
Fig. 1-4 Current approaches to the search for Weakly Interacting Massive Particles.

The ionization and scintillation detectors suffer from the inherent problem that at the very low recoil energies ($\sim$ 10-100keV) most of that energy is turned into heat, resulting in the small efficiencies, which is desribed in detail in Chaper 5. This fact plus the potential of very good energy resolution, has promoted widespread work on cryogenic detectors (see Table 1-3). Cooper pairs in a superconductor have binding energies of the order of 10^{-3}eV, and phonons in a crystal at 100 mK have energies of 10^{-5}eV. Hence the excitation energies are much smaller than atomic electrons or electrons and holes in a semiconductor, which leads to potentially very low threshold. The problem is to minimize microphonics, electronic nise, radioactive background at low energy and operating stability not only in the heat detection, but also for the ionization detection.

In spite of their poorer resolution compared to Ge and cryogenic detectors, scintillators play at present an important role in this field for several reasons. Scintillation detection is a well known and simple technique (usually no cooling needed), the ratio cost/mass is reasonably low, and there is a wide choise of target nuclei. Quite low radioactive backgrounds appear to be achievable as well. In particular some of the scintillators such as NaI(Tl) have a good light output and a possible (although problematic at low energy) Pulse Shape Discrimination (PSD). In addition scintillators include non zero spin target nuclei such as ^{23}Na, ^{127}I, ^{19}F and ^{129}Xe. And a great advantage of the

9

Table 1-3 WIMP Searches

Experiment in Progress	Location	Detector Type
Baksan	Prielbrusye, Russia	Ge ionization
Canfranc-NaI	Canfranc, Spain	NaI scintillator
COSME	Canfranc, Spain	Ge ionization
DAMA	Gran Sasso, Italy	NaI, Liq. Xe, CaF_2 scintillator
DEMOS	Sierra Grande, Argentina	Ge ionization
Milan	Gran Sasso, Italy	Cryogenic TeO_2 bolometer
UKDMC	Boulby mine, U.K.	NaI scintillator
Starting		
CDMS	Stanford, U.S.A.	Cryogenic Ge/Si bolometer with ionization
CRESST	Gran Sasso, Italy	Cryogenic sapphire bolometer
EDELWEISS	Fréjus, France	Cryogenic Ge bolometer with ionization
ELEGANT VI	Oto cosmo obs, Japan	CaF_2 scintillator
ELEGANT V		NaI scintillator
Tokyo	Nokogiri-yama, Japan	Cryogenic LiF bolometer
Under Construction		
HDMS	Heidelberg, Germany	Ge ionization
PICASSO	Montreal, Canada	Superheated Freon droplets
ORPHEUS	Bern, Switzerland	Superconducting transition in tin granules
ROSEBUD	Canfranc, Spain	Cryogenic sapphire bolometer
SALOPARD	Canfranc, Spain	Superconducting transition in tin granules
SIMPLE	Paris	Superheated Freon droplets
UKDMC	Boulby mine, U.K.	Liq. Xe scintillator

scintillator approaches is that large detector masses may allow the use of the annual modulation signature.

1) annual modulation

Nuclear recoil of WIMPs produce a continuous distribution with a roughly exponential peak at the low end of the spectrum. What are the signatures that would permit distinguishing them from the background ? The most convincing signature would be the observation of the expected annual modulation of 10 % in rate and mean energy deposition [18]. This modulation of known phase is due to the fact that depending on the time of the year, Earth is adding or subtracting part of its velocity to that of the Sun. However a 5 σ effect would require 5000 events; this would be obtained in 1 yr with one $CaF_2(Eu)$ module of ELEGANT VI (0.29kg), if the event rate was greater than 50 events/kg/day. The required rates are listed for several other effects in Table 1-4.

Table 1-4 The required rates for annual modulation in one year measurement with one $CaF_2(Eu)$ module of ELEGANT VI (0.29kg).

effect	total event for 1 yr	event rate(events/kg/day)
5 σ	5000	70
4 σ	3000	30
3 σ	2000	20
2 σ	800	8
1 σ	200	2

At present searching for annual modulations have been carried out by Canfranc-NaI(see Table 1-3) [19] and ELEGANT V-NaI [20], however, no positive evidence has been observed yet.

2) inelastic scattering

Another important signature would be inelastic processes $\chi N \rightarrow \chi N^*$ followed by the deexcitation of the nucleus N^* (see Fig. 1-3(c)) would provide two coincident signals, which has been proposed by M. W. Goodman and E. Witten [21] in addition to elastic scattering. The actual rates for favored nuclei are calculated by J. Ellis, R. A. Flores and J. D. Lewin [22]. Unfortunately, this rate is unlikely to exceed 10^{-4} counts/kg/day. In order to excite the transition, it is necessary that an excited state energy $\triangle E \leq 1/2\mu v$. They only consider isotopes with $\triangle E \leq 100$ keV, since for larger excitation energies, inelastic rates would be suppressed by more than a factor of 10.

11

Two experiment of this kind has been carried out by ELEGANT V [23] looking for the low-lying state (57.6 keV) of ^{127}I in huge NaI(Tl) and DAMA [24] looking for that (39.6 keV) of ^{129}Xe in enriched at 99.5% in liquid ^{129}Xe scintillator. It is noted here that these excited states are predominantly both M1 (magnetic dipole) transition, because whose spin matrix element can be evaluated from the inverse process of the M1 γ deexcitation. In the case of CaF$_2$(Eu) detector, the favored low-lying state would be the first excited state (21.5 keV) of ^{151}Eu. However, total amount of ^{151}Eu in all 25 CaF$_2$(Eu) modules are only $\sim$ 6g. The level scheme of ^{19}F is shown in Fig.1-5 and not favored.
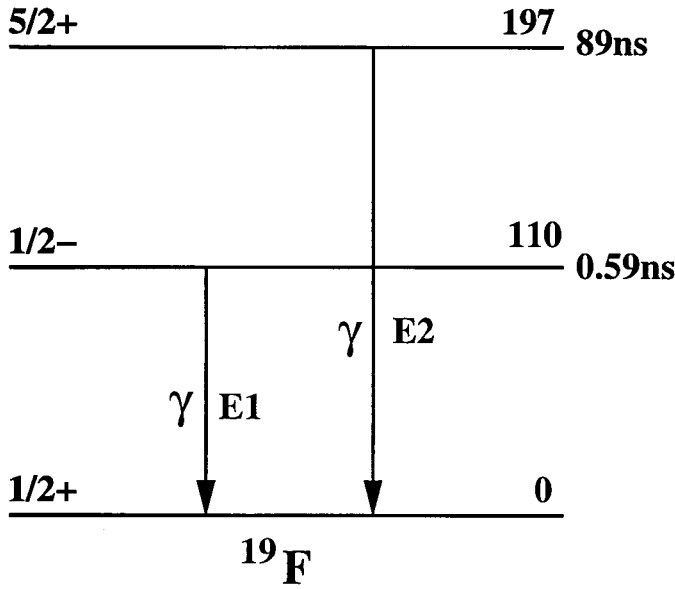
Fig. 1-5 Level diagram of ^{19}F. The level energies are given in keV.

3) **indirect search**

High energy particles are produced by the annihilation of dark matter particles in our galaxy. These are presently searched for using baloon-borne antiproton and positron detectors [25] and large area, deep underground neutrino telescopes [26].

The antiproton and positron flux of WIMP origin is proportional to the square of their halo density and to their confinement time in the halo. The latter is unfortunately uncertain by roughly four orders of magnitude. Due to such astrophysical uncertainties the detection of WIMPs in these experiments can be no means guaranteed. This is contrast with searches using the Sun and Earth rather than the halo as the source of WIMPs.

WIMPs with galactic orbits that happen to intersect an astronomical object will be trapped if the elastic scattered WIMPs velocity be lower than the escape veloc-

ity from the object. As the number of WIMPs in the object gradually increases, the capture rate is balanced by the annihilation rate. The leptonic decays from annihilation channels such as W^+W^- turn the Sun into a source of high energy neutrinos. Their energies are in the GeV to TeV range. The best signature comes from ν_μ interacting in the rock below the detector yielding muons observed in the detector ("upward going muons"). These muons can be distinguished statistically from those due to the interactions of atmospheric neutrinos because their momenta point in the direction of the Sun or the Earth's center. These limits are complementary to those obtained in direct detection experiments. Nevertheless, they must be considered with some cautions about the annihilation cascade processes leading to the observable neutrinos, on the detailed composition of the Sun and of the Earth, and on the existance or not of a steady state in their core. Then Indirect detection experiments on more assumptions than the direct ones. The Kamiokande limit on the flux of upward going muons limits their cross section on hydrogen to be less than about 1/10 for a Majorana neutrino. The discovery in the near future of WIMPs with spin dependent interactions by direct experiments would indicate that one of the following hypotheses is true [27].

* The particle is light, that are only inefficiently seen in Kamiokande. In addition, particles lighter than about 2 GeV would evaporate from the Sun.

* The particle-antiparticle asymmetry is large, though this is not possible for Majorana particles like neutralinos (see Table 1-6).

* WIMP is observed only with odd-N nuclei, which would lead not to be captured in the Sun.

4) collider searches

The constraint on the neutralino dark matter χ is obtained from accelerator searches at LEP, the Fermilab Tevatron. The primary sparticle signature studied up to now has been the classic missing-energy signature of LSP emission. No positive signatures imply within the context of the minimal supersymmetric extension of the Standard Model that $M_\chi \geq 21.4$ GeV [28]. It is also suggested that the collider sensitivity is increased up to $M_\chi \simeq 300$ GeV by the LHC, which is designed to have a center-of-mass energy of 14 TeV for pp collisions at a luminosity $L \simeq 10^{34}$ cm^{-2}s^{-1}.

5) rare decay physics and the WIMPs search

Here I would like to comment on the status of the WIMPs search in conjuction with the other rare decay physics.

Rare decays have played a key role in the development of the standard model. The decay $\pi^+ \rightarrow e^+\nu$, which is helicity suppressed to the level of 10^{-4}, provided a

13

confirmation of the V-A nature of the weak interaction. CP violation was observed by the decay mode $K^0_L \to \pi^+\pi^-$ at the level of 10^{-3}. Studies of these classic rare decays can now be categorized as "precision experimements"[29]. Recently an event consistent with the signature expected for the rare kaon decay $K^+ \to \pi^+\nu\bar{\nu}$ at the level of 10^{-10} [30].

On the other hand, a signature beyond the standard model is still in shadow. However, very recently one candidate was observed for the proton decay $p \to e^+\pi^0$ at the mean life of 10^{33} yr, if it due to, though it is only a quite preliminary status [31]. Both the neutrinoless (0ν) $\beta\beta$ decay and dark matter experiments are exclusion experiments since up to now no positive evidence has been observed in either class of experiment.

In particular the direct detection of WIMPs are quite challenging experiments compared with the $0\nu\beta\beta$. In WIMP search with direct detection, nuclear recoil of WIMPs produce a continuous distribution in the low energy region of ~10 keV. The recognition of this signature is quite hard compared with a sharp line in the energy region of a few MeV which could be produced by neutrinoless $\beta\beta$ decays. The following strategies are rather required under these present circumstances of not reaching a detection sensitivity for observing a faint signature in the near future.

 i) precise measurement
   The background for a certain energy region for which the exclusions are derived is given as "counts (/keV/DAY/kg)" or equivalent units. Corrections to this differential energy spectrum arise from the light output response (f-value), instrumental threshold, detection efficiency, and nuclear form factor. However, under the present exclusion experiment these corrections are apted not to considered so seriously and properly. Throughout our measurement we take the position that the ambiguity is as small as possible.

 ii) the highest sensitivity
   This is mandatory and our experimental system (ELEGANT VI) is developed to be the best in the world. In order to get a high signal-to-noise ratio(S/N ratio), the target nucleus are selected properly and especially care should be devoted to how we reduce the background in the low energy region.

 iii) checking the performance and the effects
   In order to check the feasibility of each part in the system, these measurements are must and this is why the measurements should be carried out in the overground laboratory under background (cosmic rays etc.) circumstances.

It is noted here that compared with the above rare decay experiments we cannot diminish backgrounds entirely for WIMPs search and then cannot judge the signal

or not by only one event at the present experimental status. The most worrisome background might be neutron scattering, which pass the discrimination cuts and mimic WIMP signals. Hence on the first step, the neutron contribution to backgrounds in the low energy region is important to measure. Then if it is dominated, somewhat "heroic" efforts could be entertained.

1.3 Theoretical aspects of WIMPs search

The event rate for elastic scattering in a laboratory detector is written for simplicity,

$$R = N \cdot \rho v \cdot \sigma = N \cdot \frac{\rho_{DM} \beta c}{M_\chi} \cdot \sigma \qquad (1.7)$$

where R is the event rate, N is the number of target nucleus, ρ is the particle density, M_χ is the mass of dark matter, v is the velocity of dark matter, σ is the cross section of dark matter and ρ_{DM} is the dark matter density. In the following let us see the several terms in equation (1.7).

1) **particle density and velocity distribution**

The dynamical considerations that lead us postulate dark matter also suggest that the dark matter distribution may resemble [32]

$$\rho = \rho_0 \frac{a^2}{a^2 + r^2}, \quad \frac{dn}{dv} \propto v^2 exp(-\frac{v^2}{\sigma_H^2}) \text{ for } v < v_e, \qquad (1.8)$$

where ρ_0, a are the halo core density and radius, σ_H is the halo velocity dispersion, v_e is the position dependent escape velocity from the Galaxy. Using a distance from the Sun to the center of the Galaxy $r_\odot = 8.5$ kpc and a circular velocity at large radii $v_\infty = 213$ km/s, we follow Flores [33] and deduce nominal values

$$\rho_0 = 1.0 \text{GeV/cm}^3, a = 5.6 \text{kpc}, v_e = 640 \text{km/s}, \sigma_H = 213 \text{km/s}. \qquad (1.9)$$

The rms halo velocity for this halo model, $< v^2 >^{1/2} = 261$ km/s. And the distributions of (1.8) are plotted in Fig. 1-6.

15
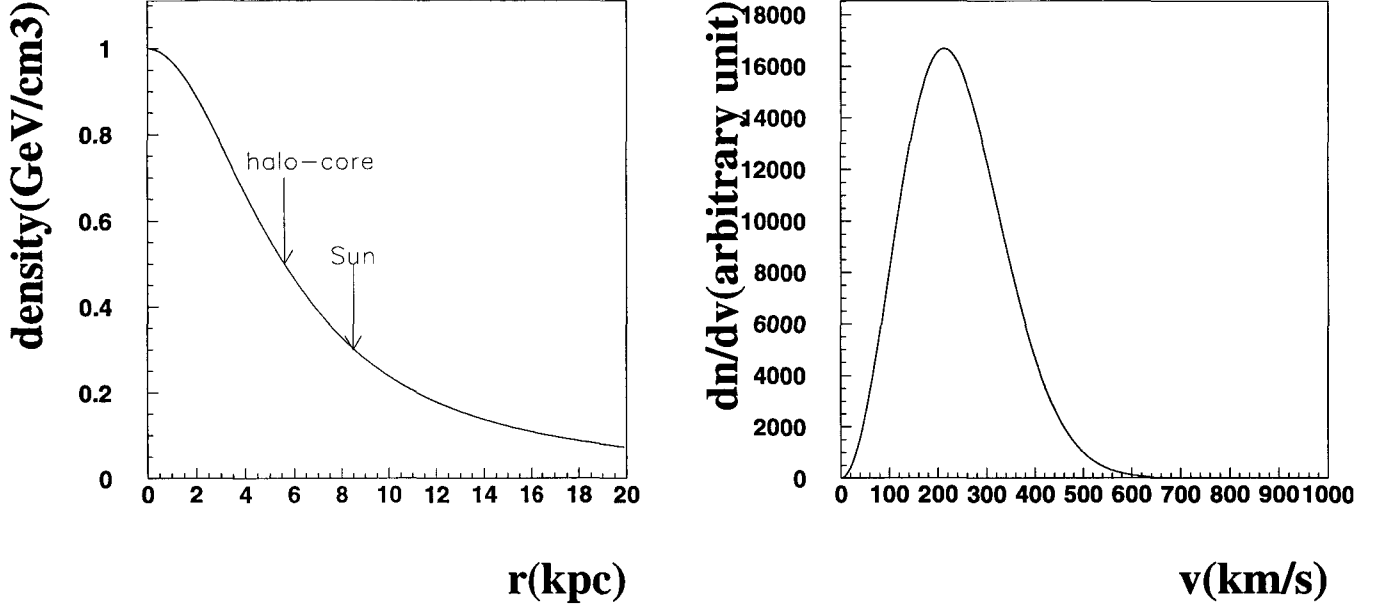
Fig. 1-6Left Radial distribution of dark matter in the Galaxy. **Right** A Maxwell-Boltzmann velocity distribution with $< v^2 >^{1/2} = 261$ km/s.

In experiments we need only the local dark matter density, $\rho_\odot$. Estimates for $\rho_\odot$ for spherical halo have been in the range 0.2 GeV/cm^3 $\leq \rho_\odot \leq 0.4$ GeV/cm^3, leading to the adoption of $\rho_\odot = 0.3$ GeV/cm^3 as the central value. However, it has always been recognized that some flattening of the halo is likely, which would increase $\rho_\odot$ in the vicinity of the Galactic plane. The most recent estimate is that of Gates et al. [34] who obtain 0.3 GeV/cm^3 $\leq \rho_\odot \leq 0.7$ GeV/cm^3 in the flattened halos, together with an estimated (1995) observational limit of 5-30% for dark matter in the non-luminous stars ('MACHOs'). This suggests a value of $\rho_\odot = 0.4$ GeV/cm^3 for non-baryonic component [35]. Hence $\rho_\odot$ have a large ambiguity depending on any further changes in the estimated MACHO fraction.

2) **cross section**

In general the cross section for a reaction: A+B→C+D in the-center-of system is given as,

$$\frac{d\sigma}{d\Omega}\Big|_{CM} = \frac{1}{64\pi^2}\frac{1}{s}\frac{p_f}{p_i}|m|^2 \tag{1.10}$$

where $d\Omega$ is the solid angle around $\mathbf{p_c}$, $s = (E_A + E_B)^2$, $|\mathbf{P_A}| = |\mathbf{P_B}| = p_i$, $|\mathbf{P_C}| =$

16

$|\mathbf{P_D}| = p_f$. The matrix element m is witten for the neutral current interaction in the case of $C = A'$ and $B = D = X$.

$$|m| = \frac{G}{\sqrt{2}}(\bar{u}_X \gamma^\mu (c_V - c_A \gamma_5) u_X)(\bar{u}_A^l \gamma_\mu (g_V - g_A \gamma_5) u_A) \tag{1.11}$$

In the non-relativistic approximation for a fermion of mass M and momemtum $\mathbf{p}$, the vector current operator; $(\bar{u}\gamma^\mu u) \sim (2M, 2\mathbf{p} + 2i\mathbf{p} \times \sigma)$ and axial vector current operator; $(\bar{u}\gamma^\mu \gamma_5 u) \sim (2\sigma \cdot \mathbf{p}, 2M\sigma); \sigma$ is a Pauli matrix, $s = (M_X + M_A)^2$ and

$$|m|^2 \simeq \frac{G^2}{2}(2M_X)^2 (2M_A)^2 (g_V^2 \cdot c_V^2 + <\sigma> g_A^2 \cdot c_A^2) \tag{1.12}$$

Hence, the cross section is given as

$$\frac{d\sigma}{d\Omega}|_{CM,point} = \frac{G_F^2}{8\pi^2} \frac{p_f}{p_i} \frac{M_X^2 M_A^2}{(M_X + M_A)^2}(g_V^2 \cdot c_V^2 + <\sigma> g_A^2 \cdot c_A^2) \tag{1.13}$$

where $c_V = T_f^3 - 2sin^2\theta_W Q_f$ and $c_A = T_f^3$ and G_F stands for the Fermi coulping constant. These values for fermions are listed in Table 1-5.

Table 1-5 The $Z \to f\bar{f}$ Vertex Factors [36]

f	Q_f	c_A	c_V
ν(Dirac)	0	1/2	1/2
ν(Majorana)	0	1	0
e,μ,τ	-1	-1/2	$\simeq$-0.03
u,c,t	2/3	1/2	$\simeq$0.19
d,s,b	-1/3	-1/2	-0.34

Using these values for c_V and c_A, the cross section for each WIMP candidate are summarized in Table 1-6 [32].

The vector (g_V) and the axial vector coupling (g_A) constants in Table 1-6 are written as (see Fig. 1-3)

$$g_V = N_n - (1 - 4sin^2\theta_W)N_p, \quad g_A = 2\lambda_N \sum_q T_q^3 \triangle q, \tag{1.14}$$

where N_n and N_p are numbers of the neutrons and protons in the target nucleus, respectively, θ_W is the Weinberg angle, $T_{u,d,s}^3 = 1/2, -1/2, -1/2$ is the third component of weak isospin, and $\triangle q$ is the fraction of the spin carried by the quark. And $\lambda_N = \frac{J(J+1)+S(S+1)-L(L+1)}{\sqrt{3J(J+1)}}$ for single particle shell model and

Table 1-6 The cross section for WIMP candidate. a;Setting $\Omega_\chi h^2=1/4$ and using EMC data($g_{A_p}=1.48$). b; $K_N = (\frac{M_\chi M_N}{M_\chi + M_N})^2$. c; $M_\chi=4$ GeV. d; $M_\chi=7$ GeV. e; $\lambda_N, \Delta q$ as in e; Q_q is charge of quark q, $e^2 = 4\pi\alpha$. This form assumes left and right squark masses are equal. f; $M_\chi=10$ GeV, $M_{\tilde q}=84$ GeV. g; $tan(\beta) = v_1/v_2$, the ratio of two higgs vevs. This form neglects Yukawa couplings to the quarks. h; $M_\chi=10$ GeV, $cos^2(2\beta)=1/2$. i; Generic "LSP" is linear combination of all neutral spin 1/2 particles: $\tilde\gamma, \tilde z, \tilde h_1, \tilde h_2$.

WIMP	Majorana fermion	t-channel	s-channel	Elastic cross sections $\sigma_{\chi N}$	Typical $\sigma_{\chi p}(\text{cm}^2)^a$
ν_D	no	Z	-	$\frac{G_F^2}{8\pi}K_N(g_V^2 + 3g_A^2)^b$	7.3×10^{-39c}
ν_M(Fig.1-7)	yes	Z	-	$\frac{3G_F^2}{2\pi}K_N g_A^2$	3.7×10^{-38d}
$\tilde\gamma$(Fig.1-7)	yes	-	$\tilde{q}\tilde{l}$	$\frac{3\lambda_N^2}{\pi}K_N[\Sigma_q(\frac{eQ_q}{m_{\tilde q}})^2\Delta q]^{2e}$	2.3×10^{-39f}
$\tilde h$	yes	Z	$\tilde{q}\tilde{l}$	$\frac{3G_F^2}{2\pi}K_N g_A^2 cos^2(2\beta)^g$	2.0×10^{-38h}
LSP^i	yes	Z	$\tilde{q}\tilde{l}$	ref.[37][14]	$\sim 10^{-38} \sim 10^{-40}$

J=nuclear spin, $S = 1/2$, $L = J \pm 1/2$, Σ_q is sum over quark flavors. And $\lambda = \frac{1}{2}(1 + \frac{S(S+1)-L(L+1)}{J(J+1)})$, the effective spin parameter of the nucleus, is given by Landé formula, then $\lambda_N^2 = 4/3\lambda^2 J(J+1)$ and $g_A = \frac{2}{\sqrt{3}}\lambda\sqrt{J(J+1)}\Sigma_q T_q^3\Delta q$. As for the nuclear spin matrix element $\lambda^2 J(J+1)$, a more realistic value is obtained by assuming all nucleons of the same type as the unpaired nucleon contribute, with the net spin of these 'odd-group' nucleons estimated from the nuclear magnetic moment [38]. The comparison between the single particle model and the odd-group model for various isotopes are listed in Table 1-7.

On the other hand hadronic matrix element; $C_{\chi N}^2 = \Sigma_q T_q^3\Delta q$ in the case of ν_M and $\tilde h$ depend on the values assumed for the quark spin fractions Δq , while the nonrelativistic quark model (NQM) yields no strange quark content ($\Delta s \equiv 0$), European Muon Collaboration (EMC) measurements indicate that strange quarks make a significant contribution to nucleon spin. Squared expectation values of hadronic matrix elements for WIMPs are tabulated in Table 1-8 [35].

From the experimnetal point of view, the important thing is the relative sensitivity of odd-N_n (Ge, Xe) and odd-N_p (Na, I, F) targets. The ratio of $C_{\chi p}^2/C_{\chi n}^2$ gave ~2 for EMC [40] whatever the neutralino, whereas the values of EMC[39] yield a ratio is close to unity for Higgsino(Majorana neutrino) but $>\sim 10$ otherwise.

As you see the above, the axial vector coulping (g_A) constants (λ and Δq) is strongly model dependent, however, in the case of Majorana neutrino (Higgsino) elastic scattering off proton of Fluorine target nucleus, the ambiguity is small (see

18

Table 1-7 Values of $\lambda^2 J(J+1)$ for various isotopes. The second column gives the experimentally determined total angular momentum J. The fourth column gives the shell model description of the nucleus. The last two columns give the single- particle and odd-group model predictions for $\lambda^2 J(J+1)$.

isotopes	abundance(%)	J	Shell model(nL_J)	$\lambda^2 J(J+1)$ single particle	odd group
^{7}Li	92.5	3/2	$1P_{3/2}$ proton	0.417	0.244
^{19}F	100	1/2	$2S_{1/2}$ proton	0.750	0.647
^{23}Na	100	3/2	$1D_{5/2}$ proton	0.350	0.041
^{127}I	100	5/2	$2D_{5/2}$ proton	0.250	0.007
^{133}Cs	100	7/2	$1G_{7/2}$ proton	0.194	0.052
^{73}Ge	7.8	9/2	$1G_{9/2}$ neutron	0.306	0.065
^{129}Xe	26.4	1/2	$3S_{1/2}$ neutron	0.750	0.124
^{131}Xe	21.2	3/2	$2D_{3/2}$ neutron	0.150	0.055

Table 1-7 and Table 1-8).
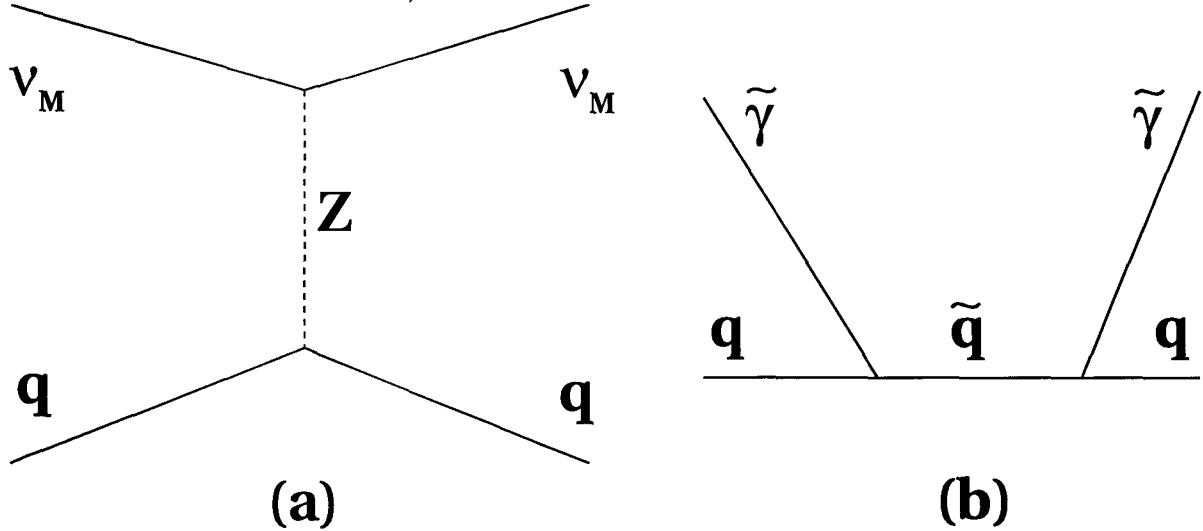
Fig. 1-7 (a) Scattering of Majorana neutrino off quarks of a nucleus. (b) Scattering of photino off quarks of a nucleus.

3) nuclear form factor

We must consider the finite-size effect of the nucleus in the dark matter nucleus

Table 1-8 Squared expectation values of hadronic matrix elements for photino and higgsino elastic scattering off protons (p) and neutrons (n) using EMC and NQM estimates of $\triangle q$. Values for a Majorana neutrino are the same as those for a Higgsino.

$C_{\chi N}^2 = \mid < Q_q^2 \triangle q > \mid$	NQM	EMC[39]	EMC[40]
$\tilde{\gamma}p$	0.14 ± 0.01	0.096 ± 0.009	0.06 ± 0.02
$\tilde{\gamma}n$	0.002 ± 0.001	0.012 ± 0.003	0.03 ± 0.01
$C_{\chi N}^2 = \mid < T_q^3 \triangle q > \mid$			
$\tilde{h}p$	0.40 ± 0.02	0.46 ± 0.04	0.55 ± 0.10
$\tilde{h}n$	0.40 ± 0.02	0.34 ± 0.03	0.26 ± 0.07

cross section. The finite-size effect of the cross section by means of the Born (plane wave) approximation is written in terms of a form factor $F(q)$ as

$$\frac{d\sigma}{d\Omega} = [\frac{d\sigma}{d\Omega}]_{point}|F(q)|^2, \quad F(\mathbf{q}) = \int \rho(\mathbf{r})exp(-i\mathbf{q}\cdot\mathbf{r})d^3\mathbf{r} \qquad (1.15)$$

where $(d\sigma/d\Omega)_{point}$ is the cross section of the dark matter nucleus elastic scattering in eq. (1.8), which are calculated assuming that the target nucleus is a point particle; $\mathbf{q}$ is the momentum transfer and $\rho(\mathbf{r})$ is the probability density of the distribution (the nucleon density in the nucleus) , normalized so that $\int \rho(\mathbf{r})d^3\mathbf{r}=1$. In the following let us discuss the form factor separately according to the interaction.

i) **spin-independent interaction**

The form factors are obtained by Fourier transform of (a) a solid sphere [35], approximating with the whole nucleus, (b) a Fermi distibution [41], more realistic model, and (c) a Gaussian scatterer [42], a commonly used approximation.

a) soild sphere

$$F(q) = 3j_1(q)/q = 3[sin(q) - qcos(q)]/q^3 \qquad (1.16)$$

which corresponds to $\rho(r) = \rho_0(r < r_N)$ and 0 for $r > r_N$.

b) Fermi distribution

$$\rho(r) = (1 + exp(r - R)/a)^{-1} \qquad (1.17)$$

c) Gaussian form factor

$$|F(q)|^2 = exp(-q^2/q_0^2), \quad q_0^2 \equiv 3/r_N^2 \qquad (1.18)$$

where $r_n = r_{rms} \simeq 0.89A^{1/3}+0.30$ fm.

The results of using each form factor are shown in Fig.1-8(Left) for ^{19}F and for the comparison, the case for ^{127}I (large mass number A) is also shown in Fig.1-9(Left).

ii) **spin-dependent interaction**

In the case of spin-dependent interactions there are two strategies to calculate the form factors like the calculation of the spin matrix element (λ), which corresponds to considering contributions from only the unpaired nucleon (the single particle model) or nucleons of the same type as the unpaired nucleon (the odd group model), and is likely to be substantially in error for large mass nuclei [38].

In the following calculation the radial wave function of the nucleus in the single particle model is used and then the spin dependent amplitude is written as

$$F_{spin}(\mathbf{q}) = \int |\psi_{nl}(\mathbf{r})|^2 \cdot exp(i\mathbf{qr})d^3\mathbf{r} \qquad (1.19)$$

In the case of ^{19}F the nucleus is described as 2S shell (see Table 1-7) in the single particle model. The result is shown in Fig.1-8(Right). And also for comparison ^{127}I case is shown in Fig.1-9(Right) by using the radial wave function of 2D shell of ^{127}I.

More precise calculation have been carried out for a small number of nuclei, when coupling to all odd group nucleons is taken into account [38]. In this case the early (zeros) of the spherical Bessel function are at least partially filled [35].

21
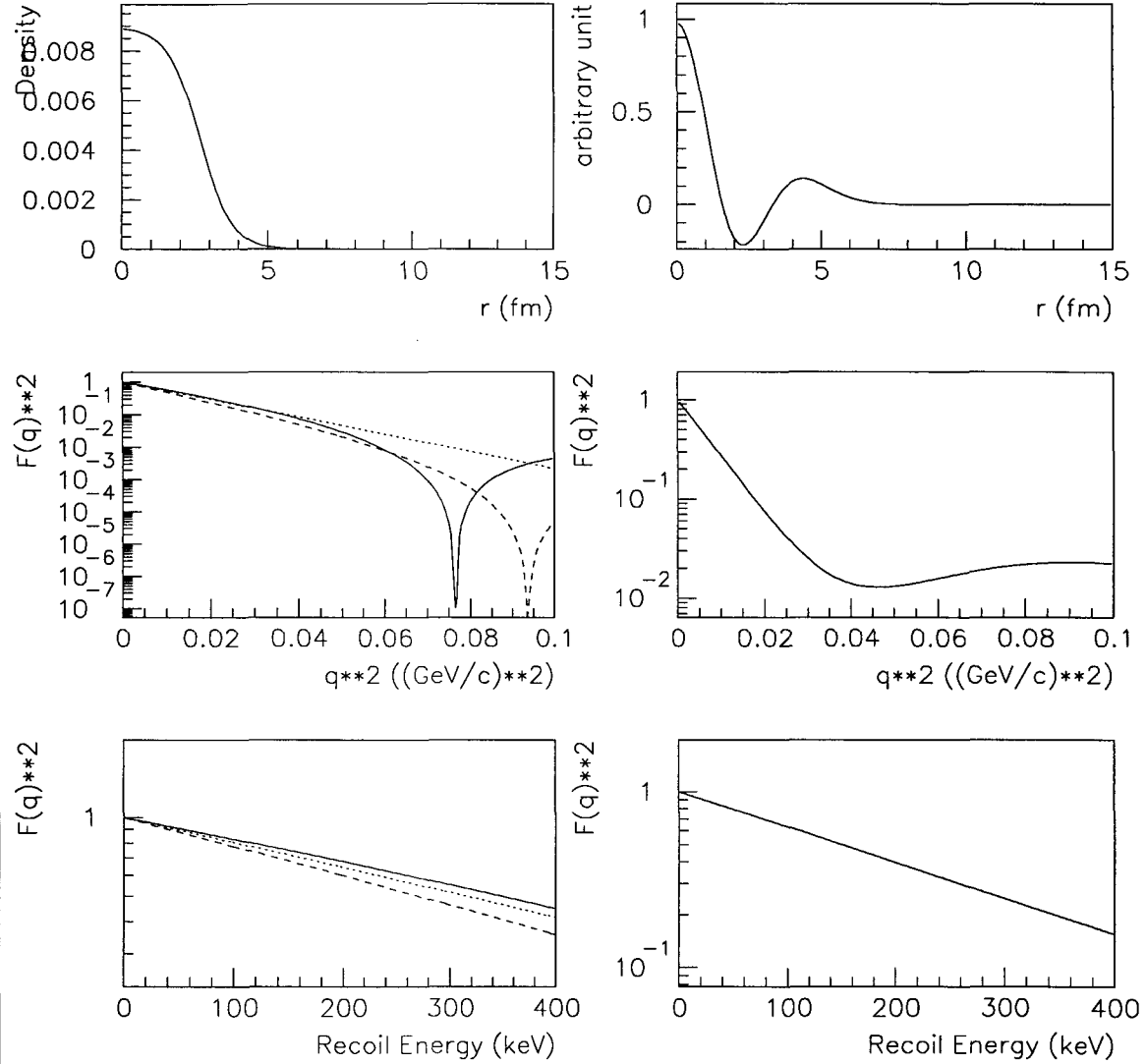
Fig. 1-8 Left; Spin independent form factor for ^{19}F. Top figure is the nucleon density as a function of a nulear radius. Center figure is the $|F(q)|^2$ as a function of q^2. Bottom figure is the $|F(q)|^2$ as a function of a recoil energy. Soild line is for the solid sphere(a). Dashed line is for the Fermi model(b). Dotted line is for the Gaussian form factor(c). **Right;** Spin dependent form factor for ^{19}F. Top figure is the radial wave function of 2S shell of ^{19}F. Center figure is the $|F(q)|^2$ as a function of q^2. Bottom figure is the $|F(q)|^2$ as a function of a recoil energy.
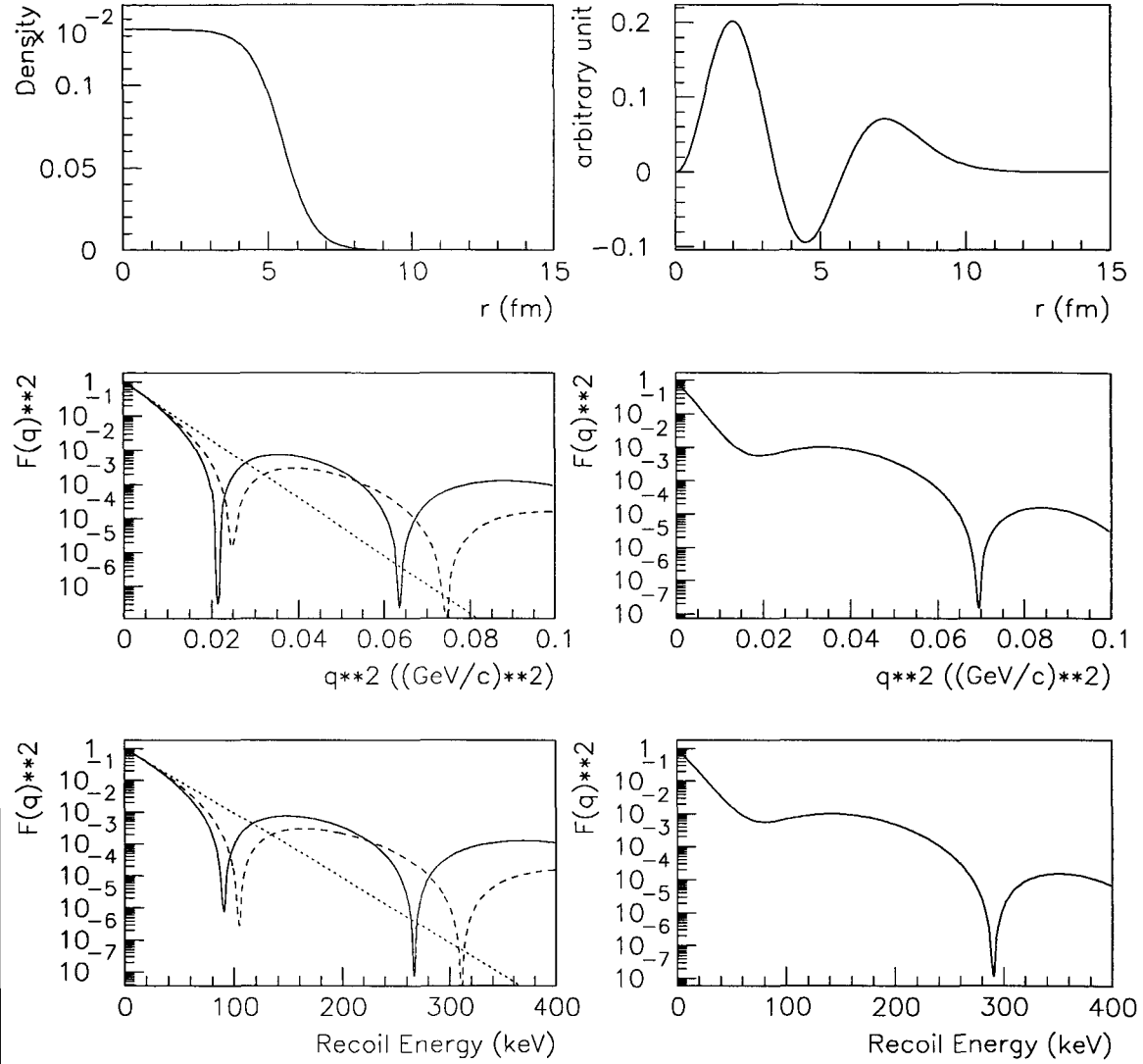
Fig. 1-9 Left; Spin independent interaction for ^{127}I. Top figure is the nucleon density as a function of a nulear radius. Center figure is the $|F(q)|^2$ as a function of q^2. Bottom figure is the $|F(q)|^2$ as a function of a recoil energy. Soild line is for the solid sphere(a). Dashed line is for the Fermi model(b). Dotted line is for the Gaussian form factor(c). **Right**; Spin dependent interaction for ^{127}I. Top figure is the radial wave function of 2D shell of ^{127}I. Center figure is the $|F(q)|^2$ as a function of q^2. Bottom figure is the $|F(q)|^2$ as a function of a recoil energy.

The coherency in the sum of the scattering amplitude over all nucleons may be broken in case of large momentum transfer ($q \cdot R > 1$) where R is the radius of the nuclei. The dimensionless quantity $q_{max}R$ are listed for several nuclear targets and for a representative neutralino mass of $M_\chi = 100$ GeV and $v = 300$ km/s.

Table 1-9 The dimensionless quantity $q_{max}R$ for several nuclear targets. The momentum tranfer is given by $q \leq 2\mu v$, where μ is the reduced neutralino nucleus mass. As for R, r_{rms} of the equation (1.18) are used.

Nucleus	q_{max}(MeV)	E_{max}(keV)	$q_{max}R$
^{19}F	30	26	0.4
^{29}Si	43	34	0.5
^{73}Ge	81	48	1.0
^{127}I	108	49	1.2

In the case of spin independent interaction, this reduction due to incoherency is about 20% and $\sim 10^{-2}$ at the recoil energy of 100 keV for ^{19}F and ^{127}I, respectively (see Fig.1-8 and 1-9). Then the loss of coherence for large nuclei is a potential disadvantage.

Convoluting the above form factor and the velocity distribution, the cross section of the equation (1.13) is expressed as,

$$\bar{\sigma} = \int \frac{dn}{dv} \frac{G_F^2}{8\pi^2} \frac{p_f(v)}{p_i(v)} \frac{M_X^2 M_A^2}{(M_X + M_A)^2} (g_V^2 \cdot c_V^2 + < \sigma > g_A^2 \cdot c_A^2)[(2\pi) \int_0^\pi sin\theta |F(\mathbf{q})|^2 d\theta] dv$$

(1.20)

In the next Chapter, we will discuss the design of our experiment based on this calculation of the WIMP-nucleus cross section.

Chapter 2

OSAKA CaF$_2$ DETECTOR (ELEGANT VI)

2.1 Aims

Osaka CaF$_2$ detector (ELEGANT VI) has following two major goals;

2.1.1 Dark matter search by elastic ^{19}F recoil

The strategy is the direct detection of spin-coupled dark matters by elastic nuclear recoils. Among spin-coupled dark matters, the lightest neutral super partner (neutralino) is one of the promising candidates. The elastic neutralino-nucleus cross section depends on the fraction of the composition such as gaugino-like or higgsino-like. The cross section for Majorana neutrino is unambiguous and comparable to the case that the neutralino is a pure higgsino state. The sensitivity is planned to reach this Majorana neutrino. Since we cannot turn off the source nor locate its direction, a several tests should be used to validate a signal. The most unambiguous evidence would be changes in the event rate and the the spectrum of energy deposition with the time of the year;(Annual modulation).

2.1.2 Double beta decays of ^{48}Ca

The detector is designed to be used also for the search of the $\beta\beta$ decay of ^{48}Ca. The large Q value of the decay (4.27MeV) makes the study ideal since little background is expected in such a high energy region. The total weight of ^{48}Ca is 7g. The present

sensitivities of our detector for 0ν and 2ν decay mode are $\mathrm{T}^{0\nu}_{1/2} \sim 7 \times 10^{20}\mathrm{years}(76\%\mathrm{C.L.})$ for one year measurement and $\mathrm{T}^{2\nu}_{1/2} \sim 1 \times 10^{20}\mathrm{years}$ for 5 month, respectively. In the case of replacement of the center $CaF_2(Eu)$ crystal with pure CaF_2 with a size of 45×45 × 200mm^3, the total weight of ^{48}Ca is 31g. However, the light output of pure CaF_2 is only about a quarter of the Eu doped one and the veto efficiency of the active light guide of pure CaF_2 would be reduced due to the coupling of the same pure CaF_2. Then, search for $0\nu\beta\beta$ in the region of $\mathrm{T}^{0\nu}_{1/2} \geq 10^{23}\mathrm{years}$ requires several studies and further developments.

2.2 Requirements

In practice, the measurements at the overground laboratory, the target nucleus with large N and the cross section with large σ are required (see the eq. (1.1) in Chapter 1.2). In general, the croser to the center of the galaxy the measurement can be done, the larger the dark matter density is, as shown in Fig.1-1. And if the ralative speed to dark matter would be increased, the event rate can be increased. The annual modulation is the use of this natural effect of the earth ralative velocity change during the year.

In considering the experimental requirements, another important factor is the energy deposition. This elastic scattering event deposits only several keV of kinetic energy in the nucleus. Assuming, as usual, that most of the dark matter halo surrounding our galaxy is made of elementary particle dark matter, so that the typical dark matter particle velocities are ≈300 km/s (see Fig.1-1). At these very small velocities the energy transfer involved is very small, $\triangle E < M_\chi v^2 = 10\mathrm{keV}(M_\chi/10\mathrm{GeV})$, which is much smaller than any elementary particle mass scale in the problem.

Above these considerations, the following experimental conditions are required.

1) **low background**

It is noted here that the need for new technology has promoted widespread work on cryogenic detectors recently. However, the starategy of background rejection is still in progress and count rate(background rate) itself is still too high [43]. At this point, the scintillator is more practical phase.

The origins of backgrounds are classified into the following two groups.

i) **internal backgrounds**

α, β and γ-rays from natural radioactive isotopes contained in materials used for the CaF_2 crystal itself.

A high radiopurification of CaF_2 crystals has been developed by a R&D project with Bicron company. To get the exact concentration of U and Th, the ICPMS(Inductively Coupled Plasma Mass Separation method) are used. The $CaF_2(Eu)$ crytal used here has been purified to the level about 0.05ppb

for U and 0.24ppb for Th. Our measured contamination are summarized in Table 2-1 compared with that of the other groups.

Table 2-1 U and Th contamination measurements by ICPMS.

manufacture	material	U(ppb)	Th(ppb)	Eu(%)
BICRON	CaF_2(Eu)	0.05	0.24	0.17(EL-VI)
BICRON	CaF_2(pure)	0.09	0.68	(EL-VI)
BICRON	CsI(Tl)	0.04	0.06	(EL-VI)
OKEN	CaF_2(Eu)	5.8	1.6	0.33~0.44
Merck	CaF_2(Eu)	1.4	6.6	(BPRS-Collab.)[44]
Quartz & Silice	CaF_2(Eu)	0.05	0.16	(BPRS-Collab.)[44]

ii) **external backgrounds**

a)β and γ-rays from natural radioactive isotopes outside the CaF_2 crystals. Some are room backgrounds and others may come from the materials used for ELEGANT VI system.

All materials used for ELEGANT VI have been checked by a low background Ge detector system(ELEGANT III) recently[45]. Samples are classified into the following four categories.

1) photomultiplier parts
2) materials used for scintillation counters(Tefron, Grease etc.)
3) materials used for passive shieldings and the airtight box (Pb, Cu, and LiH+paraffin etc.)
4) materials used for LED monitor system(LED, fiber etc.)

They are sufficiently small, but a few samples are not and can be improved (see Chapter 7-3(1)).

b)β and γ-rays from decay products of ^{222}Rn in the air around the scintillators. Detectors are kept airtight, and pure N_2 gas is circulated to purge ^{220}Rn and ^{222}Rn in the air around the detectors.

c)Charged cosmic rays such as muons and electrons.
A 3-inch×3-inch cylindrical NaI(Tl) detector was used to measure the intensity of cosmic ray component. The evaluated cosmic ray intensity at the Osaka University sea-level laboratory is about $\sim 10^2/m^2/s$ (see Table 7-9)[46].

d)Neutral cosmic rays such as neutrons induced by cosmic muons etc.
They give rise to γ-rays by (n,n'γ) and (n,γ) reactions on materials used around the detectors. A high pressure ^{3}He counter surrounded with a moderator was used for the measurement of the neutron flux at our overground

laboratory in Osaka University. This gave the neutron flux of 1.74×10^{-3} n/cm^2/s [46].

2) large cross section

As a target-nucleus, fluorine are suggested in particular by Ellis and Flores in Ref. [41] where the large cross section on ^{19}F for axially coupled dark matters has been emphasized. They showed ^{19}F(a finite spin;J=1/2) have relatively high rates and this estimation is fairly stable against a variety of calculating techniques of nuclear physics. The values of nuclear spin matrix elements, $\lambda^2 J(J+1)$, for various isotopes are summarized in Table 1-7.

As target-detectors, several fluoride scintillating compounds are available such as CaF$_2$, CsF and BaF$_2$. In this comparison, light output, mass fraction of ^{19}F and hygroscopicity are criteria. The characteristics of these scnitillators are summarized including new scintillators under R&D efforts in the Table 2-2.

From these criteria in Table 2-2, CaF$_2$(Eu) crystal are most favorable scintillator among fluoride scintillating compounds.

The other important criteria in the evaluation of various detectors are kinematics and natural abundance. These factors are combined into the so-called figure of merit[40] [1] as,

$$F_M = a_N K \frac{4}{3}\lambda^2 J(J+1) \leq 1 \tag{2.1}$$

where a_N is the mass fraction of a target nucleus in the detector and K is the kinematic factor ($K = \frac{4M_\chi M_N}{(M_\chi+M_N)^2}$). The figure of merit are listed in Table 2-3 for the isotopes in the detector at Table 1-7.

.

This table shows that a CaF$_2$(Eu) scintillator has great advantage for studying spin-coupled dark matters because of the large F_M and the small ambiguity between the models.

It should be noted that the other projects using fluoride detectors are proposed such as cryogenic LiF bolometer(Tokyo) [43] and PICASSO(Canada) & SIMPLE(Paris); superheated freon droplets [48][49] (see Table 1-3). As mentioned earlier on the low bakground subsection, it has become apparent that an important requirement of dark matter detectors is the need to reduce background electron events arising from radioactivity that cannot be eliminated by shielding or purification of detector

---

[1]In Ref.[40], the abundance is natural abundance, not a_N in this context.
[2]DAMA collaboration uses Kr-free xenon enriched at 99.5% in ^{129}Xe [47]

Table 2-2 Characteristics of fluoride scintillators. In order to comparison, NaI(Tl) and CsI(Tl) are also shown. The light output is given relative to NaI(Tl)=100. Index of refraction is at the wavelength of the peak emission.

Quantity	$CaF_2(Eu)$	CsF	BaF_2	CeF_3	CdF_3	$LaF_3(Nd)$	$LaF_3(Ce)$
R&D				yes	yes	yes	yes
density(g/cm^3)	3.19	4.64	4.89	6.16	6.38	5.95	5.95
radiation length X_0(cm)	1.68	2.0	2.03	1.66	1.73	2.0	2.0
decay constant(ns)	940	2.8	0.6/620	30	7	6	3/27/185
peak emission(nm)	435	390	220/310	375	520-580	175,350	290,340
light yield(relative)	50	6	5/16	4-5	0.25	5	0.5/5/0.2
index of refraction	1.44	1.48	1.56	1.68	1.55	1.7	1.7
hygroscopicity	no	very	little	no	no	no	no
mass fraction(%)	49	13	22	29	34	29	29

Quantity	NaI(Tl)	CsI(Tl)
R&D		
density(g/cm^3)	3.67	4.53
radiation length X_0(cm)	2.59	
decay constant(ns)	230	1050
peak emission(nm)	415	550
light yield(relative)	100	85
index of refraction	1.85	1.80
hygroscopicity	strong	slight
mass fraction(%)	-	-

material, although low energy thresholds appear possible in LiF thermal detector. In low temperature Ge detectors, nuclear recoil discrimination can be achieved by measuring ionization simultaneously with the thermalized phonon signal [50]. However, the mobility of electrons and holes is too low to allow sufficient charge collection for this technique to be used in LiF [51] and this is likely to be true for other fluorine- containing low temperature detectors. Then, alternative routes to fluorine-containing detectors have been sought which may allow improved prospects for background rejection. Fluorine-containing scintillators such as $CaF_2(Eu)$ is preferable candidate detector.

It is noted here that another advantage of fluorine is that for dark matter masses below 50GeV, the nucleus mass M_N is better matched to the mass M_χ of the incident particle. The average energy deposition at low energy is

Table 2-3 Figure of merits, F_M, for the various nuclei of Table 1-7. The kinematic factor is calculated for $M_\chi = 50\text{GeV}$, because the lower limit of the accelerator experiment in Chapter 1.2.

target nucleus	a_N	K	F_M(single)	F_M(odd)
^{7}Li in LiI(Eu)	0.049	0.43	0.012	0.0069
^{19}F in CaF$_2$(Eu)	0.49	0.80	0.39	0.34
^{23}Na in NaI(Tl)	0.15	0.86	0.060	0.0071
^{127}I in NaI(Tl)	0.85	0.81	0.23	0.0064
^{133}Cs in CsI(Tl)	0.51	0.79	0.10	0.028
^{73}Ge in Ge	0.078	0.97	0.031	0.0065
^{129}Xe in Liq. Xe	0.264^2	0.81	0.21	0.035
^{131}Xe in Liq. Xe	0.212	0.80	0.034	0.012

$$E_R = \frac{M_\chi^2 M_N}{(M_\chi + M_N)^2}\bar{v}^2, \qquad (2.2)$$

where $\bar{v}$ is the average velocity of the projectile. The energy is maximum when the target has the same mass as the incident particle. The typical shape of this relation, and their variation with target mass M_N and incident particle mass M_χ are illustrated in Fig. 2-1. The mean kinetic energy E_R would amounts to 4 keV for particles with 10GeV mass and $\beta \sim 10^{-3}$ impinging on fluoride nuclei, while 2keV for germanium nuclei.

Target Mass(Gev)   **DM Mass(Gev)**

30
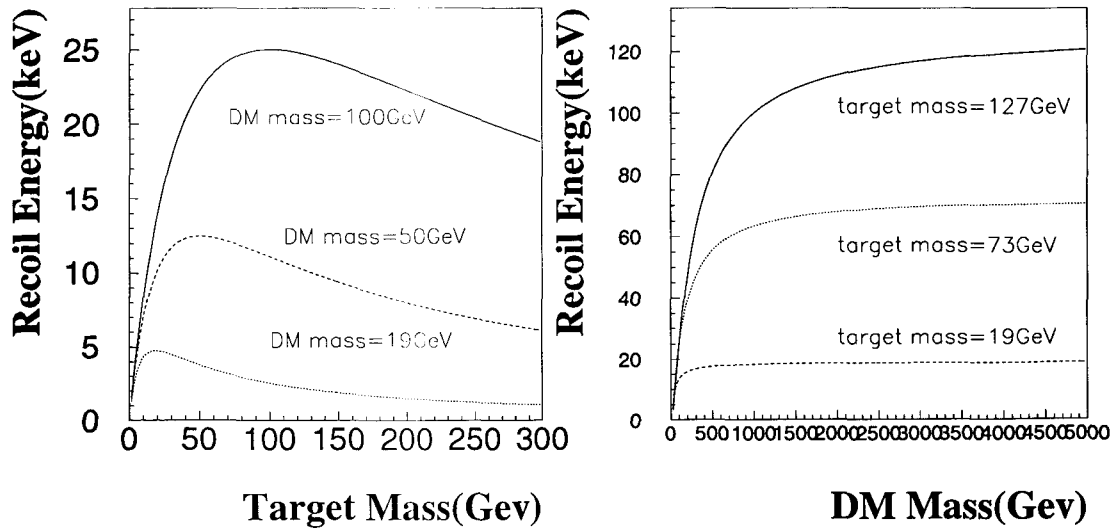
Fig. 2-1 Left: Typical shape of the average energy deposition at low energy. The recoil energy is maximum($E_d = M_\chi/4$) when $M_N = M_\chi$. Right: The recoil energy approaches to the target mass multiplied by $\beta^2 = (v/c)^2 = 10^{-6}$ when $M_\chi \to \infty$. It is noted that this is based on the condition of $\bar{v}$ is constant. The solid line is the case for ^{127}I. The dotted line is for ^{73}Ge. The dashed line is for ^{19}F.

3) large target volume

A third approach is to strive for large target masses, trading off redundancy for simplicity and large event rates which, for instance, may allow the use of the annual modulation signature. As for cryogenic detectors, there are number of groups developing detectors with large masses. However, the mass is still in $\sim O$(gram). On the other hands, use of scintillators would allow fabrication of multi-kg detectors. ELEGANT VI uses the large volume of about 3.5kg of 100%^{19}F.

4) low energy threshold

It is clear that ultralow background detectors with an energy threshold as low as possible are needed, and that any effort in improving the level of sensitivity of the detectors are rewarding. Thus, in order to disentangle the expected signal from the background at such low energies, one has to design procedures to remove not only the backgound originated in natural/induced redioactivity or cosmic-ray (environmental backgrounds) but also electronic noise and microphonics. Actually, this external disturbances due to microphonics and electronic noise are still dominating the background in the low energy region for low-level Ge detectors, which is a common problem of this type of detectors even for achieving the extremely low background ($\sim 10^{-1}$counts/keV/yr/kg at $\sim$MeV) by Heidelberg- Moscow $\beta\beta$ experiment [15]. You can see the threshold is somewhat higher for Ge detectors in the following Table 2-4. It is also quite important to obtain detailed information of the detection efficiency in the low energy region like a few photoelectron. High gain amplifiers with integration circuit and low noise discriminators are developed. By using a light emitting diode (LED) signal, the efficiency as well as the energy resolution for such low energy signals are determined.

5) recoil response calibration

It is well known that a slowly moving nucleus tranfers very little of its energy to the electrons in the material, and the resulting pulse height in a scintillation/ionization

detector of a slow nucleus is much smaller than that of an electron of the same kinetic energy. The ratio of pulse height between an electron and a nucleus is called f-value or quenching factor. We need to calibrate this f-value of our crystal, because it is suggested that the f-value depends on the scintillator, the activator concentration, the recoil energy, and the temperature. For instance, significant differences are generally present in literature on the f-values especially for Xe nuclei measured by different authors. The specific reason of interest is the high estimated f-values of liquid Xenon. It is suggested the recombination effect enhances the light response to highly ionizing particles (as the recoil nuclei) [52]. And in particular, for the case of CaF_2(Eu), UK group suggested that for dark matter purposes care should be taken to perform calibration experiments using a scintillator with the same doping as used in the dark matter detector itself [53]. Consequently, direct neutron scattering measurement of the response to nuclear recoils is required.

Table 2-4 Several important quantities for typical detectors to be considered in a choise. E_{th-ee} is the energy threshold in electron equivalent energy(keV). f-value is the scintillation efficiency (the so-called "quenching factor"). $E_{th} = E_{th-ee}/f$ is the recoil energy threshold. (n) means that in this case, the f-value has been measured by elastic scattering of monoenergetic neutrons with several scattering angles.

target nucleus	E_{th-ee} (keV)	f	E_{th} (keV)	project
^{19}F in CaF_2(Eu)	2	0.011-0.20(n)[54]	18-10	ELEGANT VI
^{19}F in CaF_2(Eu)	4	0.07-0.12(n)[44]	57-33	DAMA
^{23}Na in NaI(Tl)	5	0.4[16]	13	ELEGANT V
^{127}I in NaI(Tl)	5	0.05[16]	100	ELEGANT V
^{23}Na in NaI(Tl)	8	0.30[53]/0.35(n)[55] (300K)/(160K)	27/23 (300K)/(160K)	UKDMC
^{127}I in NaI(Tl)	8	0.08[53]/0.10(n)[55] (300K)/(160K)	100/80 (300K)/(160K)	UKDMC
^{23}Na in NaI(Tl)	2	0.30[53]	7	DAMA
^{127}I in NaI(Tl)	2	0.08[53]	25	DAMA
^{76}Ge in Ge	2	0.30[56]	7	Gotthard
^{76}Ge in Ge	12	0.25-0.30[15][3]	40-48	Heidelberg-Moscow
^{129}Xe in Liq. Xe	10	0.5-0.8[52][57]	17-13	DAMA
Xe in TPC	-	0.25(n)[4]	-	UK/UCLA

[3]Recently, its low energy behavior is investigated down to recoil energies of 3keV by neutron beam measurement. [58]

[4]Recently, the first neutron beam measurement for Xe recoil has been done by Wang et al. [59], but

It is noted here that the maximum recoil energy for ^{19}F is given as, $1/2M_N(2v_{mean})^2$ $\sim$160keV when we take the twice of mean velocity of maxwell distribution for the velocity of dark matter. Then it is enough to investigate for the fluorine recoil energy less than 200keV. Low energy properties for typical detectors are summarized in Table 2-4.

---

preliminary though.

2.3 Design principle of ELEGANT VI

We have been developing a new detector system; ELEGANT VI, which consists of 25 $CaF_2(Eu)$ crystals with dimension of 45mm cube. ^{19}F isotope in CaF_2 serves as a good scatterer with large nuclear matrix element for the spin coupled dark matter. ^{48}Ca isotope in CaF_2 serves as a source for double beta decays with the highest Q-value of 4.27MeV. The large mass fraction of ^{19}F in a CaF_2 is quite important propertity to search for spin coupled dark matters candidates, which is three times larger than that of ^{23}Na in NaI. $CaF_2(Eu)$ crystals are surrounded by active and passive shields. The whole detector system is shown in Fig. 2-2. It consists of 25 CaF_2 modules and 40 CsI(Tl) ones.

Fig. 2-2 Schematic view of ELEGANT VI. upper part; front view; lower part; side view, $CaF_2(Eu)$: $CaF_2(Eu)$ scintillator; CaF_2: CaF_2(pure) light guide; Pb: lead shield; Cu: OFHC shield; CsI(Tl): CsI(Tl) scintillator; AT: air tight box; CD: cable drain; PMT: photo multiplier tubes.
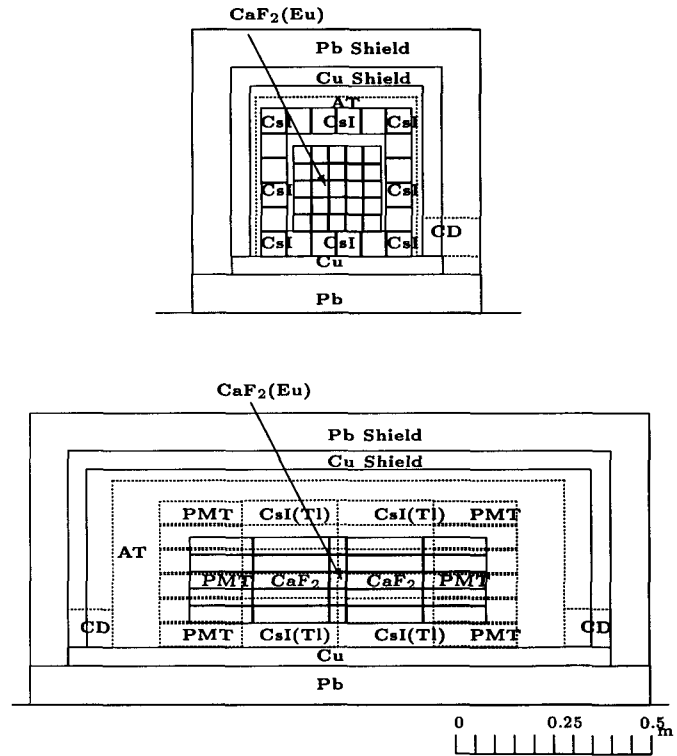
As a whole, four major newly-devices are introduced to this system especially for the background reduction as follows,

1) 4π active shield
   Active shield made of CsI(Tl) scintillators are set around the CaF_2 scintillator-complexes. As for the PMT-sides so far, a relatively long light guide are utilized as

only a passive shield to reduce background from the PMTs. In CaF_2 scintillator-complexes, pure CaF_2 are utilized as a active light guide to achieve 4π active shield. Taking advantage of the difference of the scintillation light between Eu doped CaF_2 and pure CaF_2, the difference of the pulse height between the both sides of PMTs are enhanced and the fired position in the scintillator-complexes are clearly identified. The ratio of this difference between these pulse heights can be defined as the so called roll-off ratio;$R = (V_L - V_R)/(V_L + V_R)$, where V_L and V_R are the pulse heights of the PMTs at the left and right ends of the scintillator-complexes. This background redution technique is quite effective especially in the low energy region and the properties are investigated more in detail in Chapter 3.

2) Non-hygroscopic

No containers of CaF_2 and CsI crystals are necessary because of non-hygroscopic features. Therefore bare crystals with thin light shield are used in this system. The containers have two meanings in the direct dark matter search. One is the energy loss in it, and another is the origin of backgrounds. NaI(Tl) detector, which is usually used as an active shield, needs container to prevent deliquescence. In the ELEGANT V, a low-background high-purity(99.999%) aluminium (Al) plate 0.8mm in thickness is utilized for containers, which makes the veto efficiency lower for low energy backgrounds such as X-rays. The attenuation of several materials are listed in Table 2-5 [60]. ELEGANT VI system enables one to make 4π active shield even for X-rays. Another advantage is the low background originated in the least materials. Both scintillators are chosen to make active shield as hermetic as possible and dead space minimun, since air or materials in the space may contain backgrounds.

Table 2-5 The photon attenuation in the several materials at the energy of 10 keV.

material	density(g/cm^3)	thickness(μm)	attenuation
Al	2.69	800	0.13
Teflon(fourfold)	2.1-2.2	320	0.81
Al mylar		20	
mylar	1.38-1.395	20	0.99
Cu	8.93	5 cm	0.023 at 80 keV
			0.74 at 1MeV
CaF_2	3.18	4.5 cm	0.40 at 100keV

3) Segmentation

CaF_2 detectors are divided into relatively small segments. True event is confined

in a small region in space, on the other hand background events are supposed to be spread in space. Therefore small segmentation is effective to reduce background. The $CaF_2(Eu)$ has a size of 45×45 × 45mm^3. The PM tube is 1.5" Hamamatsu H3178 although diameter of the socket assembly is reduced to 44.5mm(H3178MOD) from 47mm to install 25 CaF_2 without any space in between [61]. The lightoutput of CaF_2 is small (The light yield is about a half of NaI by the Table 2-2.), then the PMT is adjusted to cover maximum area to obtain maximum light collection efficiency.

4) **Large volume**

Large volume of about 3.5kg of 100% ^{19}F with $J = \frac{1}{2}$ is available for 25 $CaF_2(Eu)$ assemblies. The attenuation length of $CaF_2(Eu)$ is about 13cm. Then, the attenuation through the 45mm length is about $exp(-4.5/13) \sim 7\%$, so making the larger volume of $CaF_2(Eu)$ crystal is impractical.

2.3.1 Detectors

1) **CaF_2 scintillator-complexes**

One unit of the CaF_2 scintillator-complex consist of the combination of two kinds of CaF_2 crystals as shown in Fig. 2-3. The properties and characteristics are described in detail in Chapter 3. The whole crystal is covered with fourfold teflon sheets (BC-642 PTFE Reflector tape;BICRON, 80μm) and an aluminized myler (90313;Toyo-metalizing, 20μm) to make the light collection maximum [62].

In order to monitor the gain shift of PMTs, the light of LED(light emitting diode; NLPB520 Nichia Chemical) is sent to both sides of the crystals through optical fibers (BCF98 BICRON). This monitoring system is vital especially for the search of annual modulations of WIMPs, because the signal below 5 keV cannot be tested by a radioactive source and the low Z of CaF_2 material makes its photo peak hardly seen.
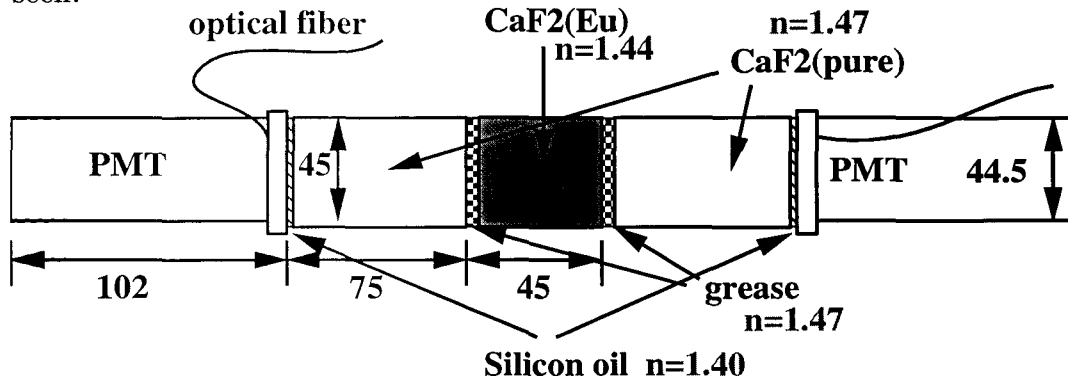
Fig. 2-3 Side view of CaF$_2$ scintillator complex. In order to support optical fibers and PMTs, acrylic plates with the thickness of 10mm are covered PMTs. n is the refractive index. The size is given in mm.

a) linearlity of the low energy region

The CaF$_2$(Eu) was checked for linearity of response to γ ray energies below 100 keV and the results are summarized in Fig. 2-4. The linearity appears to be quite acceptable for most practical purposes.
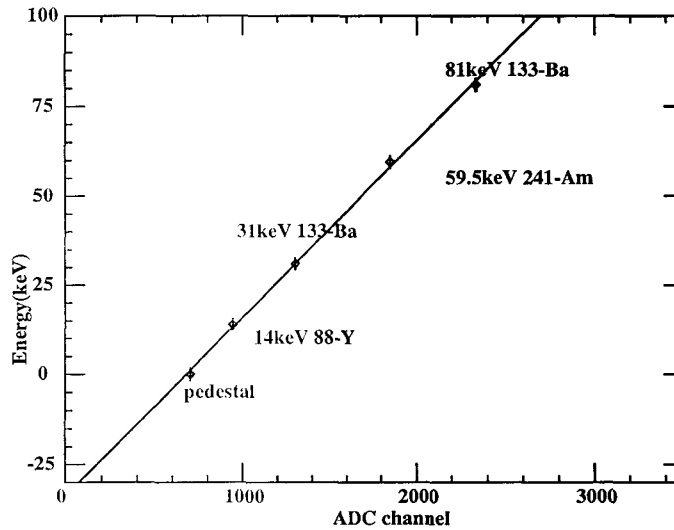
Fig. 2-4 Linearity of response of CaF$_2$(Eu) to X-rays and low energy gamma rays as a function of energy (keV).

b) energy resolution

Typical γ ray response of CaF$_2$(Eu) is illustrated in Fig. 2-5. The resolution performance of all 25 modules of CaF$_2$(Eu) are checked by the 662 keV γ ray from the ^{137}Cs source and summarized in Table 2-6. Resolution as a function of the reciprocal square root of energy is obtained [63].
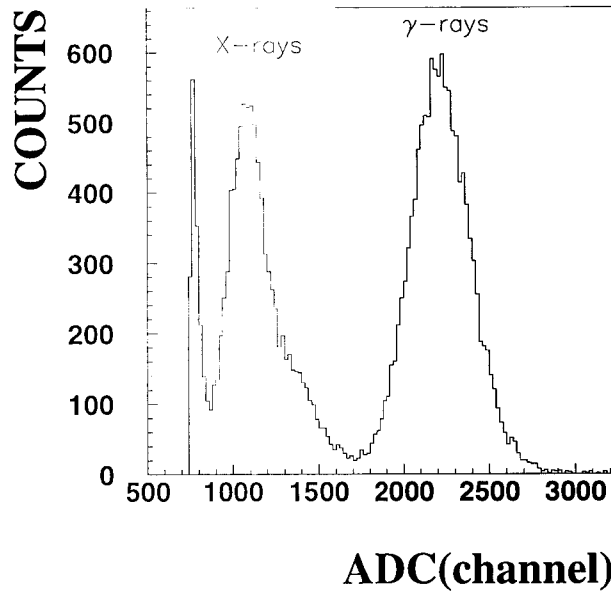
Fig. 2-5 Response of CaF$_2$(Eu) to the 59.5 and 17.5, 13.9 keV γ ray and X rays from the ^{241}Am source. This spectrum is obtained after the roll-off selection which is described in Chapter 3.

2) CsI(Tl)
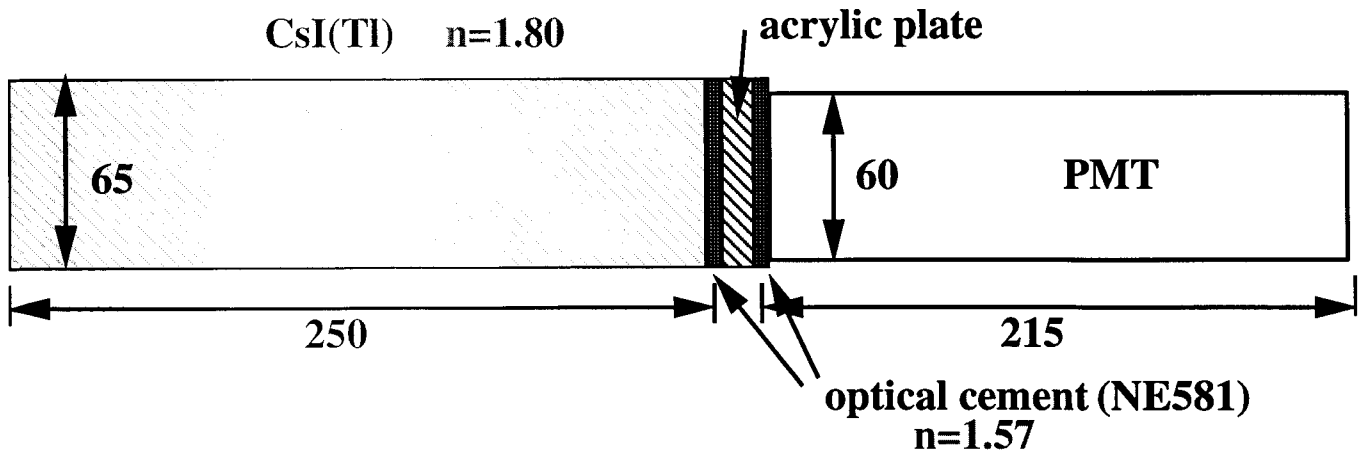
Fig. 2-6 Side view of CsI(Tl) scintillator. The size is given in mm. n is the refractive index.

Fourty modules of 6.5 × 6.5 × 25cm^3 CsI(Tl) scintillators, provied by BICRON,

Table 2-6
Energy resolution are checked by the 662keV γ ray from the ^{137}Cs source.
HV=$-$1100~1400V.

Module #	PMT #:L/R	FWHM(%)	data
1	ZF6877/7586	7.5	△
2	ZF7576/7425	6.2	○
3	ZF6842/6932	6.1	○
4	ZF6923/6895	7.1	△
5	ZF6911/6927	6.8	○
6	ZF7423/7415	7.2	△
7	ZF7434/7419	6.0	⊙
8	ZF7578/7431	6.1	○
9	ZF7418/7589	6.6	○
10	ZF6868/6903	8.7	×
11	ZF6893/6907	6.4	○
12	ZF6896/6873	6.8	○
13	ZF7438/7433	6.5	○
14	ZF6881/6912	6.4	○
15	ZF7297/6858	7.0	△
16	ZF6582/6856	6.2	○
17	ZF6898/7591	7.2	△
18	ZF6885/6892	6.5	○
19	ZF6839/6840	6.5	○
20	ZF6845/7426	6.5	○
21	ZF6921/7298	6.8	○
22	ZF6878/6871	6.2	○
23	ZF6886/6865	6.3	○
24	ZF6913/6883	6.6	○
25	ZF7582/7587	6.1	○

are mounted around the CaF_2 modules as shown in Fig. 2-2. The CsI(Tl) array, covering a large solid angle of 3.2π, is used to reject background events accompanied by γ and/or X rays. Each CsI(Tl) module is viewed at an end by a 2 inchϕ PMT H1161 (R329-02) provided by Hamamatsu Photonics. In order to detach the PMT from the crystal without causing damage to the crystal when the PMT went dead, an acrylic plate of the thickness of 5mm is inserted beween the PMT and the crystal through optical cement (NE581/BC-600, BICRON). One unit of the CsI(Tl) scintillator is shown in Fig. 2-6. The whole crystal is covered with fourfold teflon sheets (BC-642 PTFE Reflector tape;BICRON, 80μm) and an aluminized myler (90313;Toyo-metalizing, 20μm) to make the light collection maximum [62]. The stability of CsI(Tl) can be checked by the environmental backgrounds. The characteristics is described in detail in Chapter 7.2.2.

The ^{40}K contamination was measured inside the shields with 5cm thick OFHC copper and 5cm thick lead. Peak yields of 1462keV γ ray were fitted by a gaussian and a linear function. The density of ^{40}K radioactivity is calculated by the formula,

$$d(^{40}K) = \frac{Y_{peak}}{I_\gamma \epsilon M_{CsI}}(\text{Bq/kg}), \quad d'(^{40}K) = \frac{d(^{40}K)}{3.7 \times 10^{10}}(\text{Ci/kg}) \qquad (2.3)$$

The contamination of ^{40}K is calculated by the formula,

$$X = \frac{d'(^{40}K) \cdot A_{CsI}}{SpA \cdot A_{^{40}K}} \times 10^6 (\text{ppm}) \qquad (2.4)$$

where the parameters of these formula are listed in Table 2-7. The peak efficiency of 1462 keV γ ray was determined by a simulation with GEANT on the asumption of the internal background.

Table 2-7
The parameters used in the formulae (2.3) and (2.4).

M_{CsI}	4.76kg	mass of the detector
I_γ	0.1067	intensity of γ ray per disintegration
ϵ	0.25	peak efficiency of 1462keV γ ray
S_pA	5.65×10^{-6}Ci/g	specific activity of ^{40}K
A_{CsI}	260	total mass number of CsI
$A_{^{40}K}$	40	mass number of ^{40}K

The results are summarized in Table 2-8.

Table. 2-8 ^{40}K contamination of all 40 CsI(Tl) are listed compared with a new CsI(Tl) with the size of 2 inch cube [64], which was originally utilized for KEK B-factory.

CsI-Module #	peak yield	$I(^{40}K)$Bq/kg	$I(^{40}K)$pCi/kg	ppm
1	1377±236	2.16±0.370	58.3±10.1	67.0±11.5
2	219±102	1.47±0.741	43.0±19.9	49.4±23.0
3	156±92	1.13±0.667	30.5±18.0	35.0±20.6
4	127±59	0.919±0.427	25.0±11.5	28.6±13.2
5	222±70	1.61±0.507	43.4±0.315	49.9±15.8
6	194±86	1.41±0.626	37.9±16.8	43.7±19.4
7	120±67	0.869±0.485	23.5±13.2	27.1±15.1
8	127±54	0.919±0.391	25.0±10.6	28.6±12.3
9	1688±240	2.64±0.374	71.3±10.1	82.1±11.8
10	1776±317	1.84±0.327	49.7±8.88	57.1±1.81
11	2888±330	2.99±0.341	80.9±9.1	92.9±10.6
12	2431±374	2.52±0.387	67.9±10.6	78.2±12.0
13	3170±417	3.28±0.432	88.8±11.8	102.±13.4
14	178±65	1.29±0.471	34.8±12.7	40.1±14.6
15	364±155	2.64±1.12	71.3±30.2	82.1±34.8
16	2373±363	2.46±0.377	66.5±10.1	76.3±11.8
17	2628±337	2.72±0.348	73.4±9.35	84.7±10.8
18	3099±395	3.21±0.408	86.6±11.0	99.8±12.7
19	1295±366	1.34±0.379	36.2±10.3	41.8±11.8
20	1289±221	9.34±1.60	252.5±43.2	290.4±49.7
21	354±144	2.57±1.05	69.4±28.1	79.7±32.4
22	2485±320	2.57±0.129	69.6±8.9	79.9±10.3
23	< 54.8	< 0.0566	< 1.53	< 1.76
24	3721±351	3.85±0.362	104.2±9.45	119.8±11.3
25	3364±490	3.48±0.506	94.1±13.7	108.2±15.8
26	151±82	1.09±0.593	29.5±16.1	34.1±18.5
27	280±104	2.03±0.754	54.7±20.4	63.1±23.5
28	1165±323	1.21±0.334	32.6±9.11	37.4±10.3
29	2318±345	2.40±0.358	64.8±9.60	74.6±11.0
30	3215±429	3.33±0.444	90.0±12.0	103.±13.9
31	2460±323	2.55±0.334	68.9±9.12	79.2±10.3
32	262±92	1.90±0.668	51.4±18.0	59.0±20.6
33	328±90	2.38±0.654	64.3±17.5	73.9±20.2
34	105±61	0.761±0.442	20.5±11.9	23.7±13.8
35	1498±214	2.34±0.335	63.4±9.13	73.0±10.3
36	1756±246	2.75±0.384	74.2±10.3	85.4±12.0
37	1285±213	2.01±0.333	54.2±9.11	62.4±10.3
38	1605±224	2.51±0.350	67.9±9.36	78.0±10.8
39	1555±261	2.43±0.407	65.8±11.0	75.6±12.7
40	1299±209	2.03±0.326	55.0±8.89	63.1±10.1
KEK-B	4190	2.50	67.0	77.6

The resolution performance of all 40 modules of CsI(Tl) are checked by the 662 keV γ ray from the ^{137}Cs source and summarized in Table 2-9. In Table. 2-9, the best resolution (FWHM) is 8.7% at 662 keV , which corresponds to 1.1 photoelectrons/keV ($\sim$0.91 keV/photoelectrons) if we consider only statistics. On the other hands, the relative light yield of CsI(Tl) is 85% of NaI(Tl) ($\sim$40 photoelectrons/keV) from Table. 2-2. If we take the quauntum efficiency of PMT for 25%, then the light yield of CsI(Tl) is about 8.5 photoelectrons/keV. Then the light detection efficiency of our CsI(Tl) detector is about 13%.

We have installed two independent passive shielding systems. In the following two sections let us discuss these shieldings separately.

2.3.2 Shields and Radon rejection

The first is a conventional shield consisting of an outer 10 cm layer of low activity lead and an inner 5 cm layer of OFHC copper.
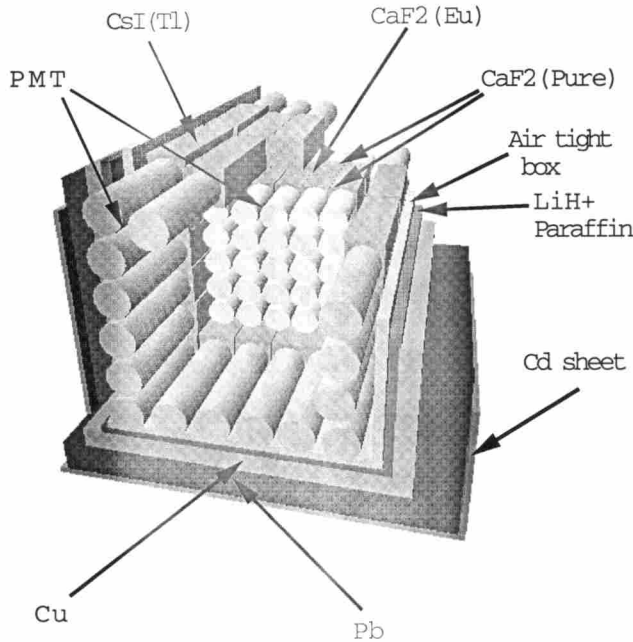
Fig. 2-7 Schematic view of ELEGANT VI.
front view, CaF$_2$(Eu): CaF$_2$(Eu) scintillator; CaF$_2$: CaF$_2$(pure) light guide; Pb: lead shield; Cu: OFHC shield; CsI(Tl): CsI(Tl) scintillator; PMT: photo multiplier tubes.

The lead shield was reformed into the unification type, which was shown in Fig. 2-

Table 2-9

Energy resolution are checked by the 662keV γ ray from the ^{137}Cs source
HV$=-1300\sim1600$V.

Module #	PMT #	FWHM(%)	data
1	CE7890(15)	9.8	◯
2	CE8865(6)	8.7	◯
3	CE7400(34)	9.7	◯
4	CE4549(44)	9.8	◯
5	RC6614	12.1	△
6	CE7970(22)	9.7	◯
7	CE5678(1)	10.0	◯
8	CE4460(11)	9.9	◯
9	CF0522	9.7	◯
10	CE8600(17)	9.8	◯
11	CE7780(42)	10.2	◯
12	CE9582(35)	9.4	◯
13	CF5038	9.6	◯
14	CE7815(5)	10.5	◯
15	CE8237(39)	10.6	◯
16	RC6597	9.4	◯
17	CE2100(29)	9.2	◯
18	CF1569(19)	9.9	◯
19	CE5021(36)	10.3	◯
20	CE9147(32)	8.9	◯
21	CE6879(9)	9.3	◯
22	CE1839(8)	10.0	◯
23	CF6498	10.7	◯
24	RC6585	9.3	◯
25	CE6589(12)	11.3	◯
26	CE9663(28)	9.4	◯
27	CE2011(14)	9.4	◯
28	CE8667(38)	9.9	◯
29	CE2081(45)	9.8	◯
30	CF6921	10.0	◯
31	CF0273(10)	9.3	◯
32	CE8727(20)	12.5	△
33	CE8758(25)	9.4	◯
34	CE5601(4)	10.3	◯
35	CF0326(16)	9.9	◯
36	CE5825(7)	9.9	◯
37	CE4582[43]	10.5	◯
38	CE6114(21)	9.2	◯
39	CE1416(43)	9.3	◯
40	CE5442(23)	10.6	◯
41	CE3547(2)	9.2	◯

8. In mounting small pieces of lead, some spaces in between are inevitable. And even if the solid angle of the aperture is only a few msr, environmental backgrounds and the radiative capture γ rays($\sim$8MeV) of ^{113}Cd go through it. Then, this reduction is mandatory. (This problem is called "streaming".)

The whole detector system is based on a stainless support rack. The total weight of the system is listed in Table 2-10.

Table   2-10   The   weight   of   the   system   (ELEGANT   VI).

component	weight(kg)
Pb (unification type)	2550
(Bottom and both sides)	2631
Pb (total)	5181
Cu (OFHC)	1578
crystal (CaF$_2$ and CsI)	222
PMT	263
detector (total)	485
H$_2$O tank	1188
Total	8432
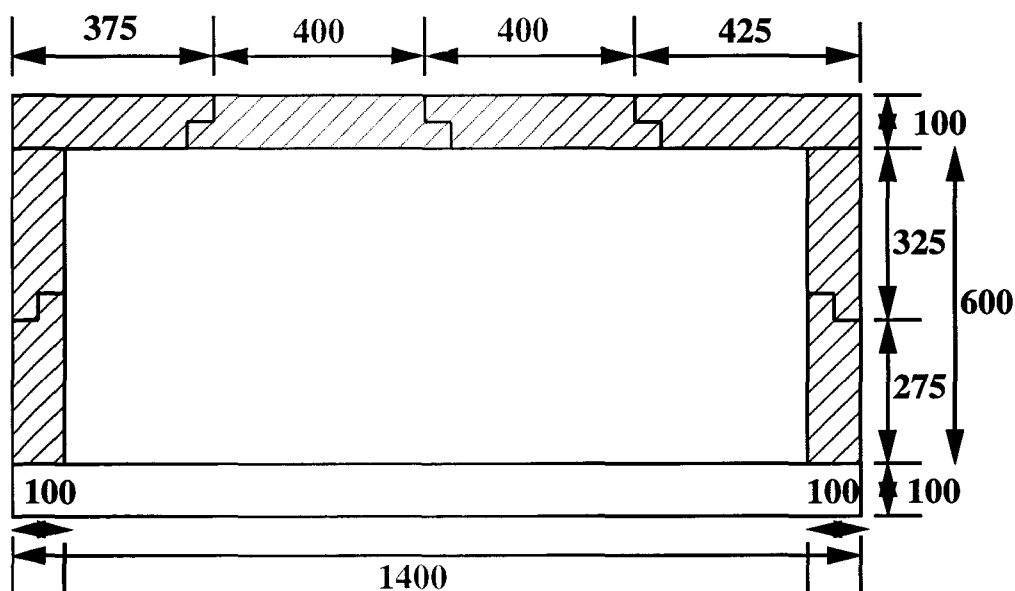
Fig. 2-8 Side view of unification type (parallel crosses type) lead shield. The unit is in mm. The lead of bottom and both sides are the conventional one.

The detector system is put in an airtight container to keep the system free from

44

radioactive Rn gas in the air. N_2 gas, which is purified to a level of four nines is introduced into the airtight container in order to purge out Rn gas from the detector region. The input and output of gas flow are checked by a flow meter and a bubbler, respectively. In the case of 400cc/min. of input flow, there is ~60 bubble/min. in the bubbler. The total volume of the airtight box is about 190 l, then it takes about 10 hour/1 circulation in the case of 300cc/min..

2.3.3   Neutron Shield

The second is a 0.6 mm layer of Cd sheet and a 15 mm layer of LiH- loaded paraffin so as to shielding against the neutrons.The whole system is shielded by a 30cm thick boron-loaded water tank moderator. In the following, let us look at each component.

It is noted here that as for one event there are no techniques to distinguish between neutron induced nuclear recoil and true dark matter event. Although we can discriminate between electron and nuclear recoil event by simultaneously measuring the ionization and phonon signals [50] or PSD methods, fast neutrons that are energetic enough to produce recoil signals above threshold, have the same signature as the particles we are looking for. Therefore, it is critical that the energetic neutron flux at the experimental site be minimized.

Neutrons are frequently classified according to their energy. Thermal neutron are in thermal equilibrium and has an average velocity of ~2200 m/s at normal temperature in a Maxwell distribution, which corresponds to the average energy $1/2 \cdot mv^2 \sim 0.025$ eV (250 K). Epithermal neutrons have energy from 0.3 eV to 500 eV, and Fast neutrons from 0.5 to 20 MeV.

1) Cd sheet

Cadomium has a quite high absorption cross section for thermal neutron. Then even if the thickness is only 0.6 mm, the reduction of the order of 10^{-3} for thermal neutrons can be expected by the following estimation. The intensity is expressed

$$I = I_0 exp(-\sigma n x) \tag{2.5}$$

where I_0 is the initial intensity, σ is the cross section, and the number of n of atoms per cm^3 is

$$n = N_0 \frac{\rho}{A} \tag{2.6}$$

where N_0 is Avogadro's number, ρ is the mass density of the material in g/cm^3 and A is the atomic number. The product σn is called the macroscopic cross section, measured in cm^{-1}, is designated by $\Sigma = n\sigma = N_0 \sigma \rho / A$. Its reciprocal value, $1/\Sigma$, is equal to the mean interaction length (cm) of the neutrons, i.e., their ,mean free path.

45

While the absorption cross section is high, this is an (n,γ) process (radiative capture). When a nucleus captures a thermal neutrons it will have an excess energy of about 8MeV, released by the binding energy of neutron. Due to this γ ray, the Cd sheet was put outside the lead shield.

2) LiH-loaded paraffin

In contrast to the ^{113}Cd(n,γ) process, Lithium is an ^{6}Li(n,α) process, which goes to the ground state of residual nucleus immediately without accompanying γ rays [5]. Lithium hydride (LiH) and Lithium carbonate (Li$_2$CO$_3$) are available for the conventional material containing a lithium. Since the mass fraction of Li for LiH is larger than that for Li$_2$CO$_3$, the amount of Li is about 9 times even if the same weight. Due to above reason, LiH is chosen, however, the LiH is toxic and has a chemical reaction as LiH + H$_2$O $\rightarrow$ LiOH + H$_2$ $\uparrow$. Then we should pay attention to handle it especially in humidity. In the ELEGANT VI system, N$_2$ gas is continously circulated and this is not a problem.

A neutrom loses all its energy in a head on collision with a hydrogen nucleus, but only a part of its energy it in head on collision with other nuclei. And it is evident that it takes a large number of collisions to degrade the energy of fast neutrons by orders of magnitude in their thermalization. If c is the average number of collisions needed to thermalize a neutron with an initial energy of E_0(eV), i.e., to reduce its energy to 0.025 eV, then

$$E_0 exp(-2c/(A + 2/3)) = 0.025 eV \tag{2.7}$$

and the number of collisions is

$$c = \frac{A + 2/3}{2} ln \frac{E_0}{0.025} \tag{2.8}$$

For the initial energy of 1 MeV, the thermalization will take 1800 collisions in lead and 15 collisions in hydrogen.

As for the moderator of Lithium, water can not be used for the above chemical reaction, then paraffin (CH$_2$) is used [6]. And the amounts of paraffin is determined so as to maximize the amounts of LiH in a paraffin. As a result the maxium weight fraction of LiH is 40% of paraffin; paraffin with the weight of 32.5kg loaded with LiH with the weight of 13kg was made.

Since this absorption reaction does not accompany any γ rays, which was mentioned above, this shield can be put inside the lead and copper shield. The contamination of natural radioactivities have been also checked. This shield is expected to be effective especially for the neutrons being produced primarily by cosmic ray muon

interactions within the lead, which shielding effect is described in detail in Chapter 6.2.3.

3) H_3BO_3-loaded water

Since the effective energy region of reduction is limited especially for thermal neutrons, which is shown in Fig. 2-10, a moderator is needed to thermalize. The whole system is surrounded by water tanks with the thicknesses of 20cm (side), 30cm (top) and 70cm (bottom) outside the Cd sheet. It is desirable for a thicker moderator of a few meter, because the mean free path is about $\sim$10 cm for fast neutrons, however, at this stage this is the loading limit for the support rack, which is already listed in Table 2-10.

Boron has a high absorption cross section for thermal neutrons. This is an $^{10}B(n,\alpha)$ process. In 93 % of the reactions the ^7Li nucleus is left in an excietd state and a 478 keV γ ray is emitted. For a further absorption, boron is incorporated in the water tank. Boron oxide (B_2O_3) and boron acid (H_3BO_3) are available for the conventional material containg a boron. Although the mass fraction of B for B_2O_3 is larger than that for H_3BO_3, the degree of solution of H_3BO_3 in water is much larger than that of B_2O_3 through the chemical reaction; $B(OH)_3+H_2O \rightarrow B(OH)_4^-+H^+$. Since the degree of solution depends on the temperature, the test of various amounts of boric acid in water was performed. As a result the maxium weight fraction of H_3BO_3 is 4% of water at room temperature; 25°C (water temperature $= 23°C$); water with the weight of 1.3 ton loaded with H_3BO_3 with the weight of 50 kg was made. The purity of H_3BO_3 is 99.5%.

These characteristics are summarized in Table 2-11.

Table 2-11 Neutron shield and moderator for ELEGANT VI.

conponent	element	natural% abundance:a	cross;σ section(barn)	a×σ (barn)	mean free path Σ(cm)
Cd sheet	^{113}Cd	12.2	20000	2440	9.0×10^{-3}
LiH+paraffin	^6Li	7.5	940	71	0.18
$H_3BO_3+H_2O$	^{10}B	19.8	3840	760	1.5×10^{-2}

The cross section and the reduction factor:I/I_0 are summarized in Fig. 2-9, 2-10.

[5]The residual nucleus is ^3H and its life time of β decay to ^3He is 12.3 year and Q_β is 18.6 keV. Then this low energy β ray can be vetoed efficiently by the anti-counters; CsI(Tl) and CaF$_2$(pure), while if Lithium is a detector itself such as LiF bolometer[43] this β decay is a serious problem.

[6]It is noted here that hydrogen has a radiative capture cross section of σ=0.332 accompanying 2.2 MeV γ ray.
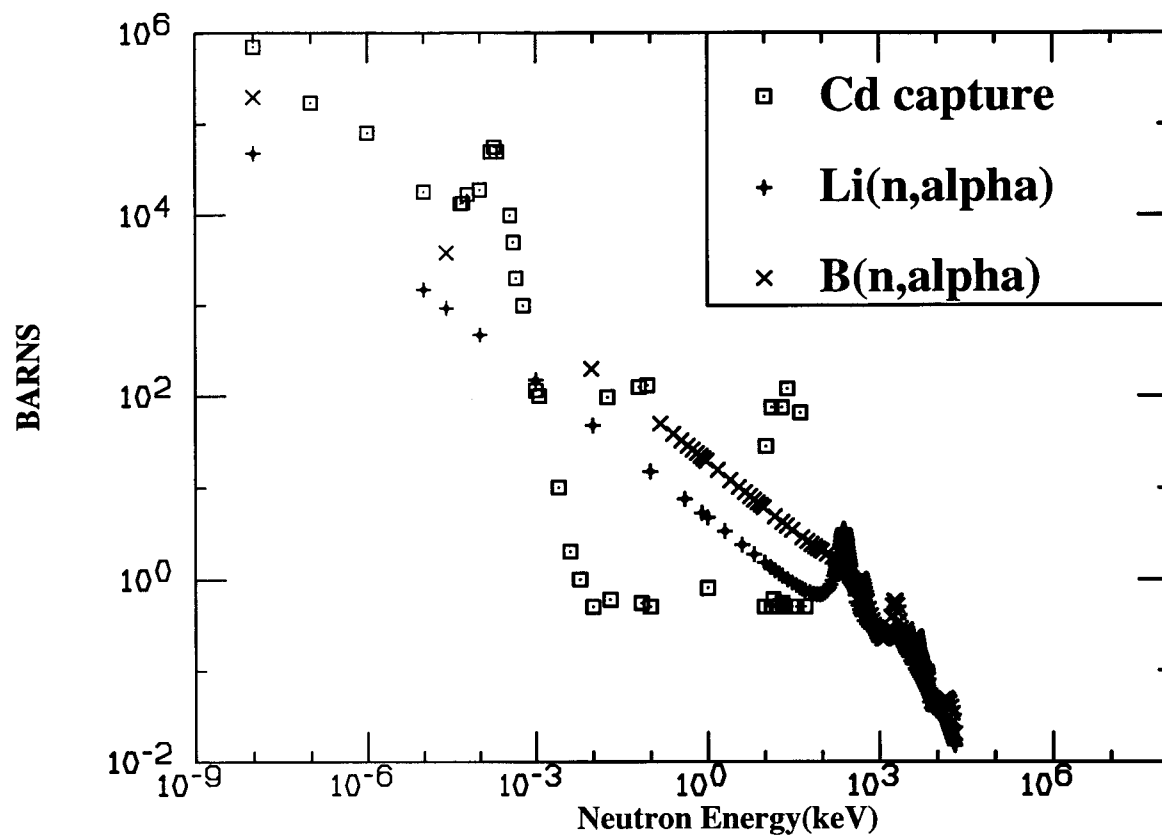
Fig. 2-9 Cross section versus neutron energy for ^{113}Cd, ^{6}Li and ^{10}B in neutron absorption. The cross section is inversely proportional to the speed of the neutron; the $1/v$ law.

48
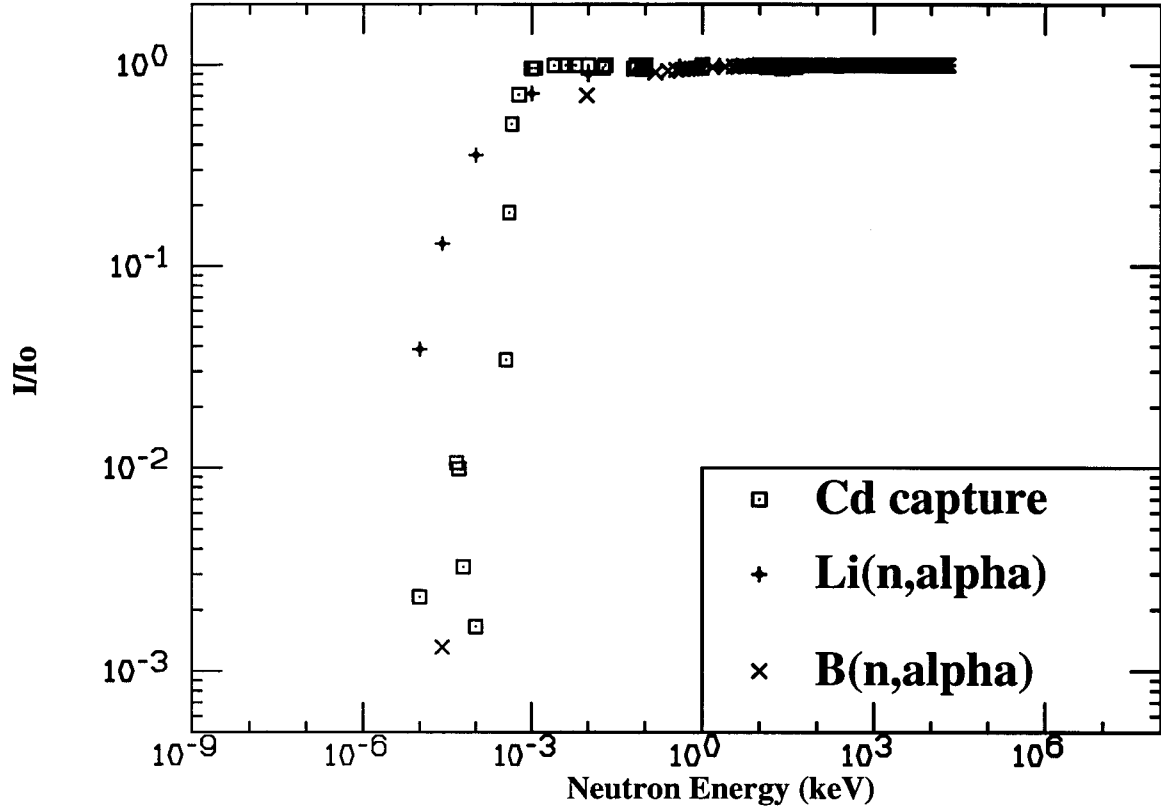
Fig. 2-10 The reduction(absorption) factor;I/I_0 $\propto 1/e$ versus neutron energy was calculated for ^{113}Cd, ^{6}Li and ^{10}B in the actual thicknesses.

2.3.4 Electronics and Data acquisition

ELEGANT VI system is designed to perform not only the dark matter search (DM) but also the study of double beta decays of ^{48}Ca $(\beta\beta)$ simultaneously. Then the raw signal of CaF$_2$ was devided into two signals of a high gain (ADC full scale = $\sim$300keV) for the dark matter search and a low gain (ADC full scale = $\sim$10MeV) for the study of $\beta\beta$ decays of ^{48}Ca, which is shown in Fig. 2-11.

There are 50 energy and timing signals from the 50 PM tubes of the 25 CaF2 modules, and 40 energy signals from each PM tubes of the 40 CsI modules. As for the energy signals of CaF$_2$, the signals are divided, which was mentioned above, and finally 102 energy signals including a gain monitoring CaF$_2$ module outside the shieldings are present. They are taken by CAEN C205 32 ch charge integrating ADCs. This ADC module is high density as a single span module, in which each input signal is converted to two words; a 12-bit word (1X-gain) and a 122bit word (7.5X-gain), corresponding to 15 bits of dynamic range. Then this ADC has 64 ch as a single span for each signal, however the

conversion time is quite long; 1.6 ms, which is 10 times of a conventional ADC(Lecroy 2249W). The data structure is listed in Table 2-12.

Then one event of recording is 180 words, however, each event has 2 words (64ch) and LAM is cleared at the 65th reading. Consequently if you consider the dead time, one event of reading is 64ch $\times$ 7(ADC) +13 header = 461 words. Including the conversion time of ADC, the dead time is about 15 ms if you take the single action of CAMAC to be 30 μs, which corresponds to 70 cps.

All digitized data are acquired by SUN workstation(IPX) through a CAMAC crate controller(K3922) and VME with K2917 and SFVME, and are stored into a 10 GB hard disk. Stored data are dumped from the hard disk into magnetic tapes three times a week. These data are analyzed by Digital UNIX (DEC) with Migration system having 7 TB tape library at RCNP.
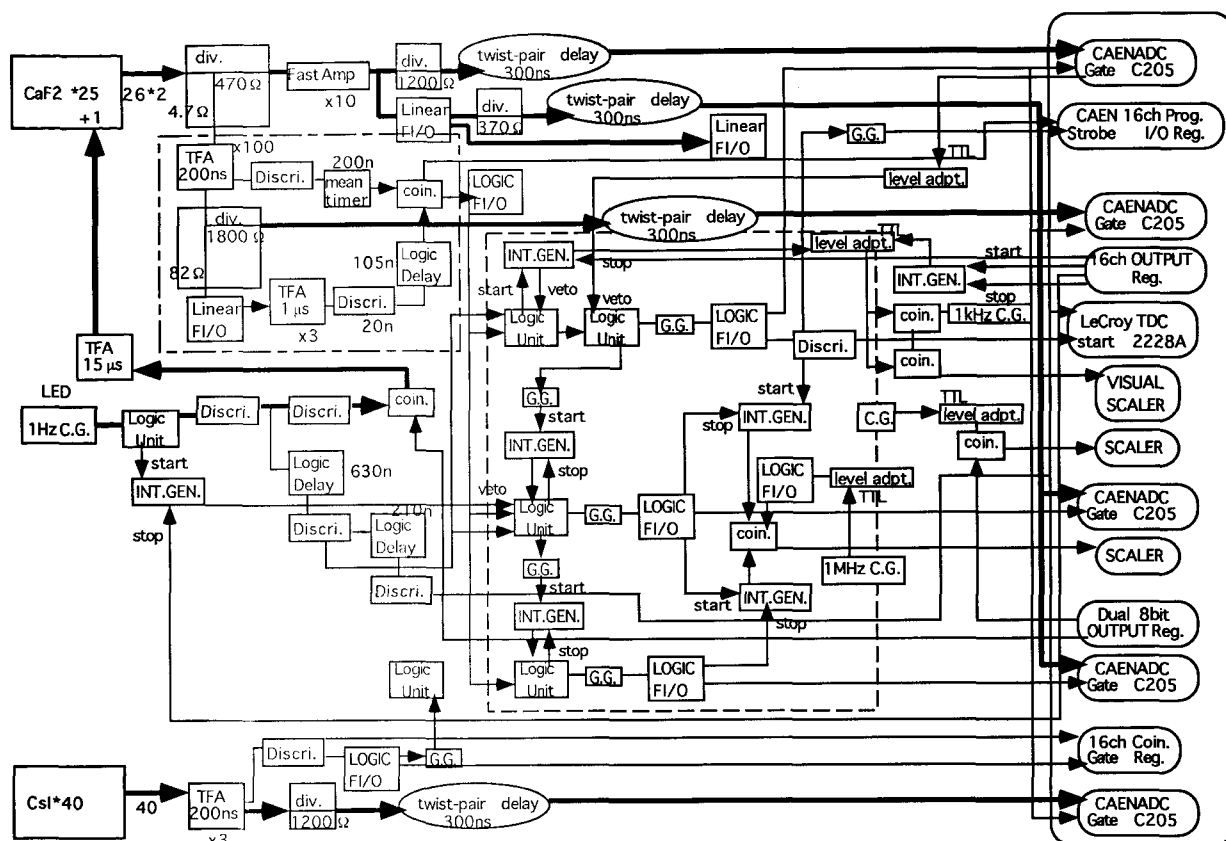
Fig. 2-11 The electronics to acquire the signal of ELEGANT VI.

51

Table 2-12 Data structure of ELEGANT VI system.

Index	Contents	
0	ID, type, size	
1	Hitpattern of LED (4-bit)	header
2	time between each event(wait) 16-bit; clock=10K	header
3	time between each event(daq) 16-bit; clock=1M	header
4	time between 1st and 2nd trigger(rate) 16-bit; clock=10M	header
5	conversion time 16-bit; clock=1M	header
6	DM($\beta\beta$) and LED trigger discrimination TDC 2228A	header
7 9	Hitpattern of CsI (16-bit data)	header
10 11	Hitpattern of CaF$_2$ (16-bit data)	header
12	live time (16-bit; clock=1K)	header
13	time between 1st and 2nd trigger 16-bit; clock=1M	header
14 63	Energy data of high gain CaF$_2$ DM (50 signals)	
64 115	Energy data of low gain CaF$_2$ $\beta\beta$ (52 signals)	
116 155	Energy data of CsI (40 signals)	
156 180	Energy data of sum of L and R CaF$_2$ 2nd trigger (25 signals)	

Chapter 3

BACKGROUND REJECTION BY ROLL-OFF RATIO

3.1 Central CaF$_2$ scintillator-complex

In order to find the low energy and rare signal of nuclear recoil by WIMPs, background reduction is essential. The background is reduced by the design of 4π active shield [65]. The whole system is described in the previous Chapter 2. The central part of the ELEGANT VI consist of 25 modules of CaF$_2$ scintillator-complexes. One unit of the CaF$_2$ scintillator-complex consist of the combination of two kinds of CaF$_2$ crystals as shown in Fig.2-3. One is central crystal made of Europium doped CaF$_2$(Eu) scintillator and the others are side crystals made of pure CaF$_2$ crystals. The CaF$_2$(Eu) crystal has light guides of pure CaF$_2$ crystal with a size of $45 \times 45 \times 75$mm^3, which are also sensitive to gamma rays. It is noticed that the side crystals made of pure CaF$_2$ act as not only light guide but also active shield against the background from outside materials. So far, we could not reject the background from photomultiplier(PM) absolutely, because we have to see the scintillation light from it. Using the long light guide, we can reduce the background from PM by some extent, but not entirely.

The scintillation is viewed by two PM through light guides(CaF$_2$(pure)) of both side of the crystal. The point is this light guide(pure CaF$_2$) scintillate unlike the usual light guide. Scintillation light from pure CaF$_2$ is dominatly in ultra violet(UV) region. On the other hand, scintillation light from central crystal CaF$_2$(Eu) is mainly normal visible light. The transmittance of CaF$_2$(Eu) is limited only for normal visible light [66], while pure CaF$_2$ transmit UV region in addtion to normal visible light. Thus center CaF$_2$(Eu)

acts as the filter from the scintillation light from pure CaF_2. Photomultiplier tube(PMT) is Hamamatsu H3178 assembly made the quartz window modification (160nm $\sim<$), which is essential to observe UV region of the scintillation light. Optical grease of KF96H (Shin'etsu silicon Co. Ltd.), which is transparent to UV light, was used for the connection between the PMT and the scintillation crystal. The refractive index is 1.44, 1.47, and 1.40 for CaF_2(Eu), CaF_2(pure) and the silicon oil, respectively, then we do not need to care reflection at the boundary. The transmittance of optical glues has been studied by M. Kobayashi et. al. in the wavelength region of 200 $\sim$ 600 nm [67] (Table 3-1).

Gamma-ray source of ^{60}Co, [133]Ba, [241]Am and [57]Co were used for the examination of the performance of the CaF_2 scintillator-complex. The decay schemes of these radioactive source are shown in Fig. 3-1. Checking the rejection efficiency at low energy, we used outer trigger from NaI(Tl) in coincidence with CaF_2 using some particular γ-ray source, which has two succesive γ-rays. The experimental setup is shown in Fig. 3-2 and the schematic of the electronics is shown in Fig. 3-3.

Table 3-1 List of optical glues examined in the test. M/H gives the
main-component/hardner weight ratio. The quantity d in the notes gives the density in
g/cm^3, and n the index of refraction for the Na-D line (589.3nm); they are taken from
the catalogue of the manufacturing companies. The cutoff wavelength is requiring a
transmittance larger than 50% and radiation resistant up to 10^6 rad.

Glues	Transmittance(nm)	M/H	Notes
EPOTEK 305	200	100/28	Epoxy Technology Inc., USA d=1.15, n=1.511
EPOTEK 328	200	100/10	ibid. d=1.45, n=1.407
Cemedine 1565	290	100/15	Cemedine Co., Japan d=1.15, n=1.57
Cemedine CS23 10-5	290	100/20	ibid. d=1.15
STYCAST 1266	290	100/28	Grace Japan Co. d=1.18, n=1.56
NE581(BC-600)	290	100/25	BICRON n=1.57
HYSOL RE2038	290	100/28	Dexter Co., USA d=1.1
Acrybond BC-415B	300	100/1.8	Mitsubishi Rayon Co. metaacrylic resin
KE103 RTV(hard)	200	100/5	Shin-etsu Chem. Co.
KE103R TV(soft)	200	100/1.5	ibid.
TSF451-50M(0.5Mcs)	200		Toshiba Silicon Co. d=0.975, n=1.404
KF96H(1 Mcs)	200		Shin-etsu Chem. Co.
OKEN 6262A	275		Oyo Koken Co. d=1.12, n=1.453
BC630			BICRON d=1.06, n=1.465
V-788			Visilox systems(not available now)
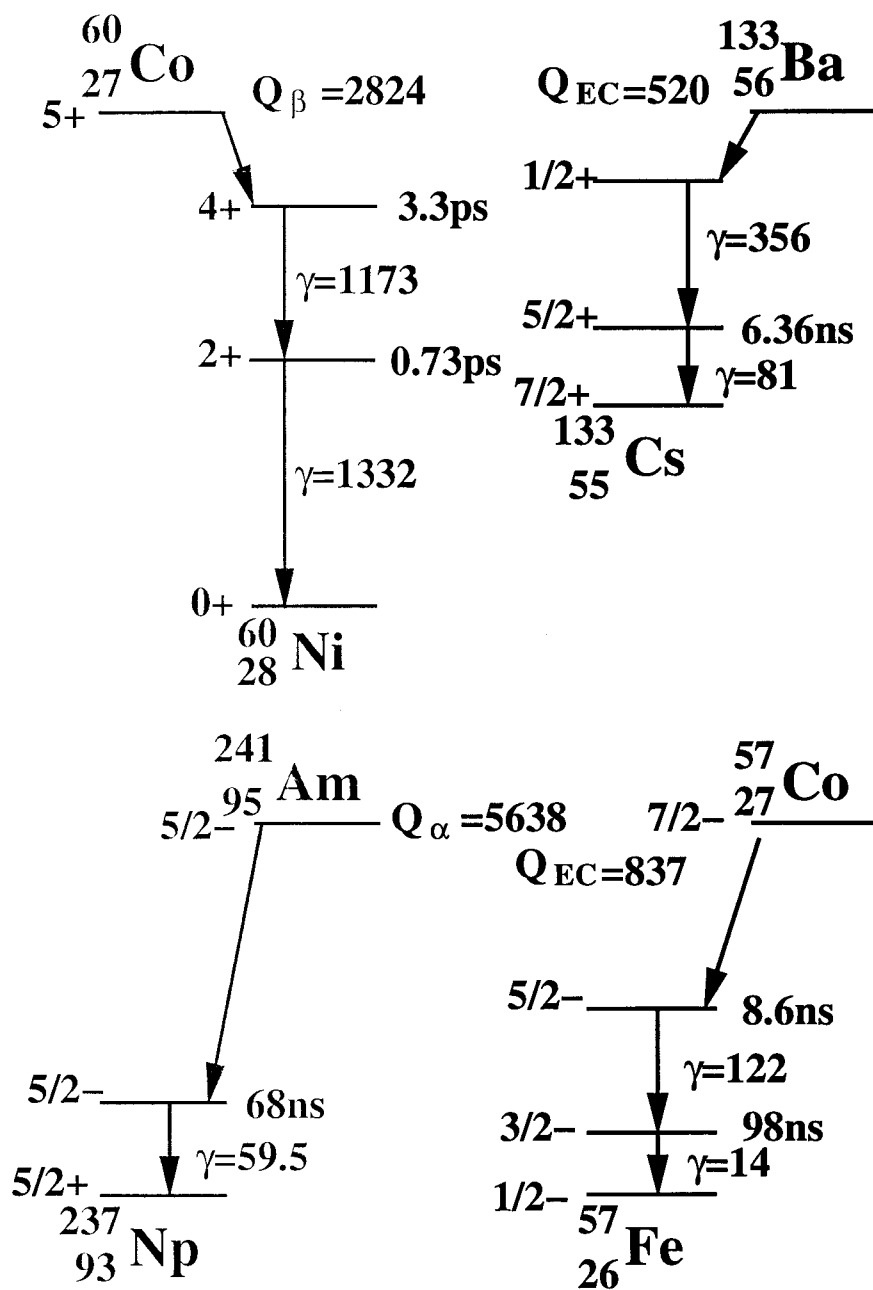
Fig. 3-1 Decay scheme of ^{60}Co, ^{133}Ba, ^{241}Am, and ^{57}Co. Energies are given in units of keV.
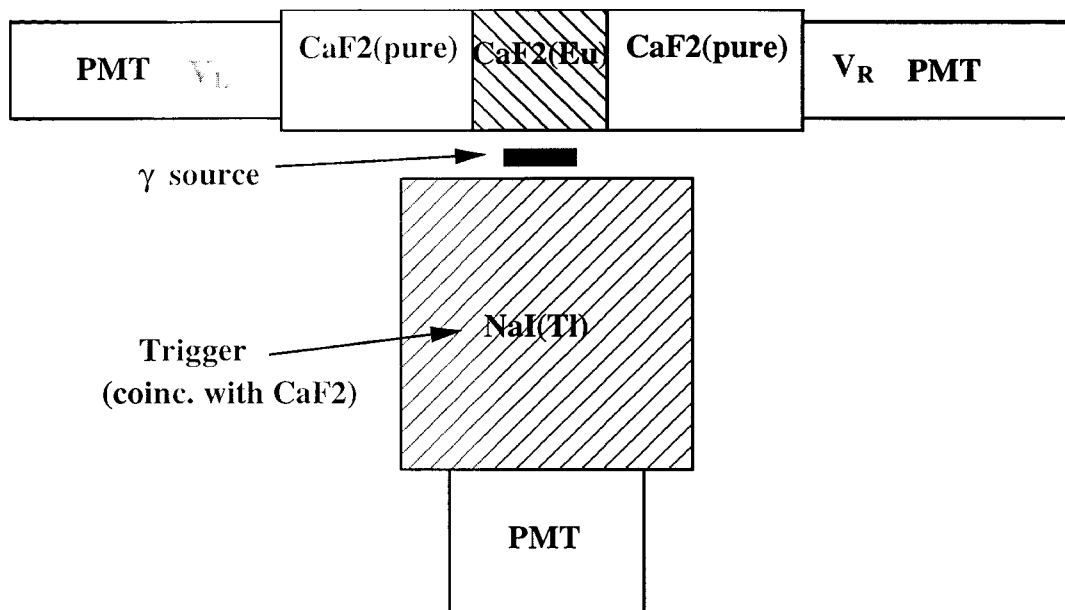
Fig. 3-2 The experimental setup.
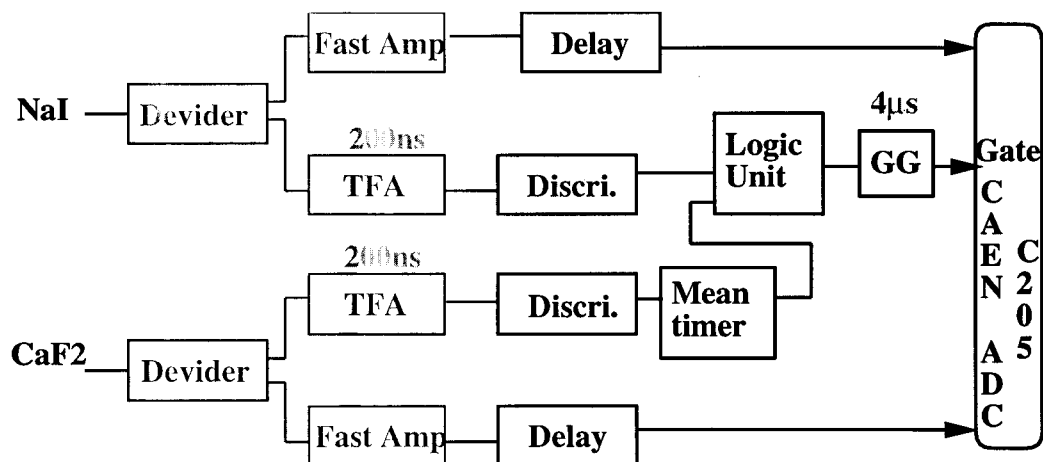
Fig. 3-3 The electronics to acquire the two succesive γ-rays by NaI and CaF$_2$.

A typical two dimensional plot of both light outputs from the both sides of PMT is shown in Fig. 3-4. It shows clearly three loci due to three crystals inside the scintillator-complex. The pulse height of the PM at one end of the CaF$_2$ crystal depends on the position of scintillation with respect to the edge of the crytal. One may define the roll-off ratio to identify the fired position of the scintillator-complex as $R = (V_L - V_R)/(V_L + V_R)$, where V_L and V_R are the pulse heights of the PMTs at the left and right ends of the

57

scintillator-complex, respectively. A typical spectrum of the roll-off ratio(R) of CaF_2(Eu) is also shown in Fig. 3-4 Three peaks correspond to directly three loci due to the central crystal and the two sides pure CaF_2 crystals. Then the events in central crystal of CaF_2(Eu) are clearly selected by setting a proper window on the roll-off ratio spectrum. The enhancement of this roll-off ratio can be done, because of the mechanism mentioned above. Since the light output of CaF_2(pure) is much less than CaF_2(Eu), the lower region of the spectrum is mainly from the pure one. Even at the 14keV, the spectrum of the roll-off ratio is quite good [68]. The leakage from side CaF_2(pure) is only several percent.

LEFT(channel)   ROLL-OFF RATIO
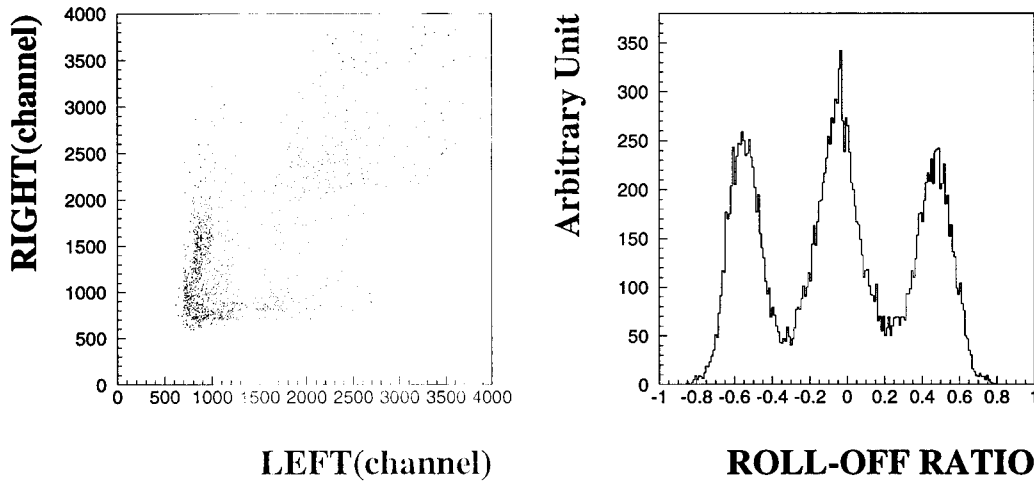
Fig. 3-4 Left A typical two dimensional plot of both light outputs from the both sides of the CaF_2 scintillator-complex.Gamma-ray source of ^{60}Co was used. **Right** A spectrum of the roll-off ratio(R). The roll-off ratio is quite useful to select signals from the central crystal of CaF_2(Eu).

3.2 4π active shield

The side crystals combines with the surrounding anothor active modules are used as the 4π active shield. Combining the differnt types of scintillators, the enhancement of roll-off ratio was achieved and we succeeded to have the system of 4π active shield. This technique is practically useful for the rejection of environmental background and available not only for double beta decay experiment in the region of several MeV but also for the search for dark matter in the region of several keV, or rather, it is more effective in the low energy region. Because in the low energy region external backgrounds deposit its almost all energy in the surrounding detectors or even the events which reached to the central

crystal surely deposit some energy by compton scatterings in the surrounding detectors. In Chapter 6.2.3. these effects is described in detail in the actural circumstances.

Up to now 'phoswich detector' has been developed as this type of detector combining different scintillators. The phoswich detector is a counter with a double scintillator layer of materials with different decay times. In the 'phoswich' case the event is separated by decay times (pulse shape:fast/slow), while in this $CaF_2(Eu)$ & $CaF_2(pure)$ case the event is separated by optical properties such as emission/transmittance of scintillation light. Then this is a new type of detector using different mechanism. The phoswich detectors are listed in Table. 3-2.

Table. 3-2 The phoswich detectors combining different(A and B) scintillators.

scintillator (A)	scintillator (B)	use
NaI(Tl)	CsI(Tl)	X-ray γ-ray Astronomy, Pu detection
$CaF_2(Eu)$	NaI(Tl)	low energy β detection
acryl plate	NaI(Tl)	
BGO	CsI(Tl)	
PL	PL	

Chapter 4

DETECTION OF LOW ENERGY SIGNAL

4.1 Properties of the CaF$_2$ detector at low energy

The dark matter gives quite low energy deposit to the detector. It is thus essential to reduce the threshold energy for the dark matter search. The decaytime of the CaF$_2$ detector is quite long ($\sim$ 3μsec) and the signal doesn't have usual leading and trading slopes but looks like a bundle of many one photon signals in a low energy signal like a few keV. It is very important to treat properly the detector signals. A signal of one photoelectron is generated by an LED mounted on the crystal. It is found that one photoelectron energy of the CaF$_2$ scintillator-complex corresponds to 0.35 keV [62].

Now let us discuss in the case of a signal of 3 keV of the CaF$_2$ detector. The signal of 3 keV means that $\sim$8 photoelectrons are distributed over 3μs. Then the both sides of PMT have 4 photoelectrons each in 3μs. At low energy, time jitter causes the reduction of efficiency and the non-linearlity of pulse height. A timig filter amplifier (TFA) solves this problem. At first, the signals of left and right PMTs are integrated with the shaping time of 200 ns. And then, after summing the signals of left and right PMT, the signal is integrated again with the shaping time of 1μs. At the same time, requiring the coincidence of left and right signal, an accidental background such as dark current of PMT is reduced to $\sim$1/12 with holding the detection efficincy of one photoelectron is larger than 95%. As a result, the signals from the two photomultipliers were separately discriminated at the level of one photoelectrons and then put in coincidence for triggering purposes. Then only pulses above a threshold of 2 photoelectons occuring in coincidence

with the coincidenced left and right event are accepted. The electronics to acquire the signal of ELEGANT VI is shown in Fig.2-11.

4.2 8ch timing filter amplifier

We developed low noise circuit and system, which allowed us to reduce the threshold energy far below 5 keV. High gain amplifiers with integration circuit and low noize discriminators has been developed [69]. The timing filter amplifier gives good timing signal even for such low energy signals. This is essential to have good energy resolution as well as efficiency. Noise of TFA depends on its gain. The S/N ratio of TFA could be improved by increasing amplifier gain up to the gain of one hundred times, which is listed in Table 4-1.

Table 4-1 The S/N ratio of TFA with the shaping time of 200 ns is measured by several amplifier gain.

Gain (×times)	noise level (mV)	the pulse height of 60keV (PMT$_{HV}$=-1400V)	S/N ratio
3	0.2	15	75
15	0.6	75	125
100	2.0	500	250
200	4.0	1000	250

The circuit noise could be achieved less than 0.1 keV, which is below the one photo-electron energy, so the electric noise is sufficiently low. A schematic circuit diagram of the timing filter amplifer is shown in Fig. 4-1.
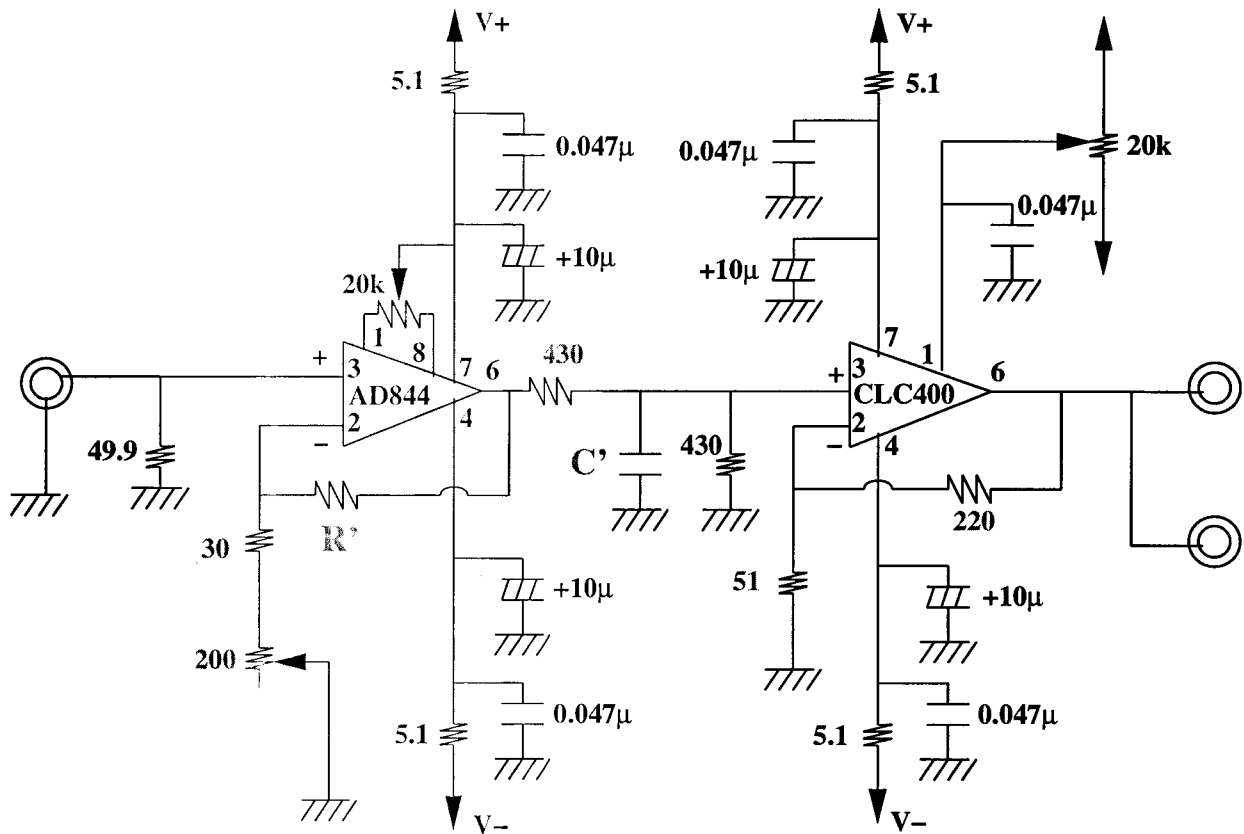
Fig. 4-1 A schematic circuit diagram of the timing filter amplifer. Differential Input Voltage; V±=6V. In the case of shaping time; τ is 200ns, a condenser; C'is 470pF and a feedback resistor; R' is 1.5kΩ, while as for τ=1μs C' is 2200pF and R' is 100Ω. In the first part for τ=200ns, the gain range;G is (30+1.5K)/30 ∼(230+1.5k)/230; 51∼7.5, while as for the second part, G is (51+220)/51∼5.3. In the first part for τ=1μs, G is (30+100)/30∼ (230+100)/230; 4.3∼1.4, while the second part is the same as the case of τ=200ns.

This TFA has the following features.

1) high density

ELEGANT VI system contains 50 energy and timing signals from the 50 PM tubes of the 25 CaF_2 modules and 40 energy signals from each PM tubes of the 40 CsI modules. As a result TFA for 92 channel (including monitor's CaF_2) is needed for ELEGANT VI. It is not practical to obtain such a high density of TFA for a single-span NIM module and hard to meet the present demand. Then 8 channel TFA for a single-span NIM module was developed 12 modules in total by ourselves.

62

2) simple archtecture

The archtecture is quite simple and devided into two parts. In the first part the almost gain is determined so as to maximize the S/N ratio, which is listed in Table 4-1. And by sending the signal through a conventional RC integrator, the pulse shaping is performed. After that, an appropriate operational amplifier (op amp) is used so as to match the shaping time. This is not a complicated integrator by using op amp, which output current and voltage is contant and linear change respectively, but by using a simple RC integrator, which output current and voltage are non-linear.

3) low noise and high gain

On the previous simple basis, an appropriate IC (op amp) is selected. These op amp topology uses 'current feedback' instead of the usual voltage feedback. This desigh has several advantages over conventional designs such as settling time is relatively independent of gain. And since this feedback is 'negative' feedback, an imaginary short (voltage difference is zero at the input 2 and 3 of op amp: see Fig.4-1) is applied. And both of op amps are 'non-inverting' gain configuration.

The main characteristics of selected op amps are listed in Table 4-2. In the first part low noise, high gain and high slew rate are required. On the other hand, in the second part wide band width is needed for the short shaping time.

Table. 4-2 The main characteristics of the selected op amps (IC) for the 1st and 2nd part.

op amp	company	band width	slew rate	gain range	comment
1st part AD844AN	Analog [7] Devices	60MHz	2000V/μs		fast response, high linearity, clean pulse
2nd part EL400CN	Elantec [8]	200MHz	700V/μs	$\pm 1 \sim 8$V	direct replacement for CLC400 [9]
CLC400	Comlinear Corporation	200MHz	700V/μs	$\pm 1 \sim 8$V	low cost, low power wideband, low gain

As a result the characteristics of the TFA is summarized in Table 4-3.

---

[7]http://www.analog.com/

[8]http://www.elantec.com/

[9]Recently, some products of Comlinear are not avaiable, because Comlinear Corporation was merged into National Semiconductor.; http://www.national.com/

63

Table. 4-3 The characteristics of the TFA; (OULNS 8ch TFA 7921).

rise time	shaping time	gain	power requirement	linearity
50ns	200ns	100(40~270)	±6V	±2V
	1μs	3(7~23)		

It is noted here that another feature of combining the two TFAs with a different shaping time of 200ns and 1μs is important. By double shaping, the characterictic frequency, in this case high frequency noise are cut due to TFA's low pass filter.

4.3 Detection efficiency of low energy signal

It is quite important to know the detection efficiency in the low energy region. We have determined the efficiency for the low energy signal by using the signal from a light emitting diode (LED). The signal below 5 keV cannot be tested by a radioactive source thus we generated the pulse shape of the low energy signal by the LED. However, the generated signal by the LED must have the same shaping as the real γ-ray signal. In order to achieve this requirement, an input signal is not a conventional rectangular pulse but a shaping pulse, which can be made by a timing filter amplifier. And the second part of TFA (OULNS 8ch TFA 7921) can be applied for this purpose. In this case a shaping time of 1.5μs are chosen and a schematic circuit diagram of this TFA is shown in Fig. 4-2. It is verified that the signal has the similar shape as the real gamma ray signal.
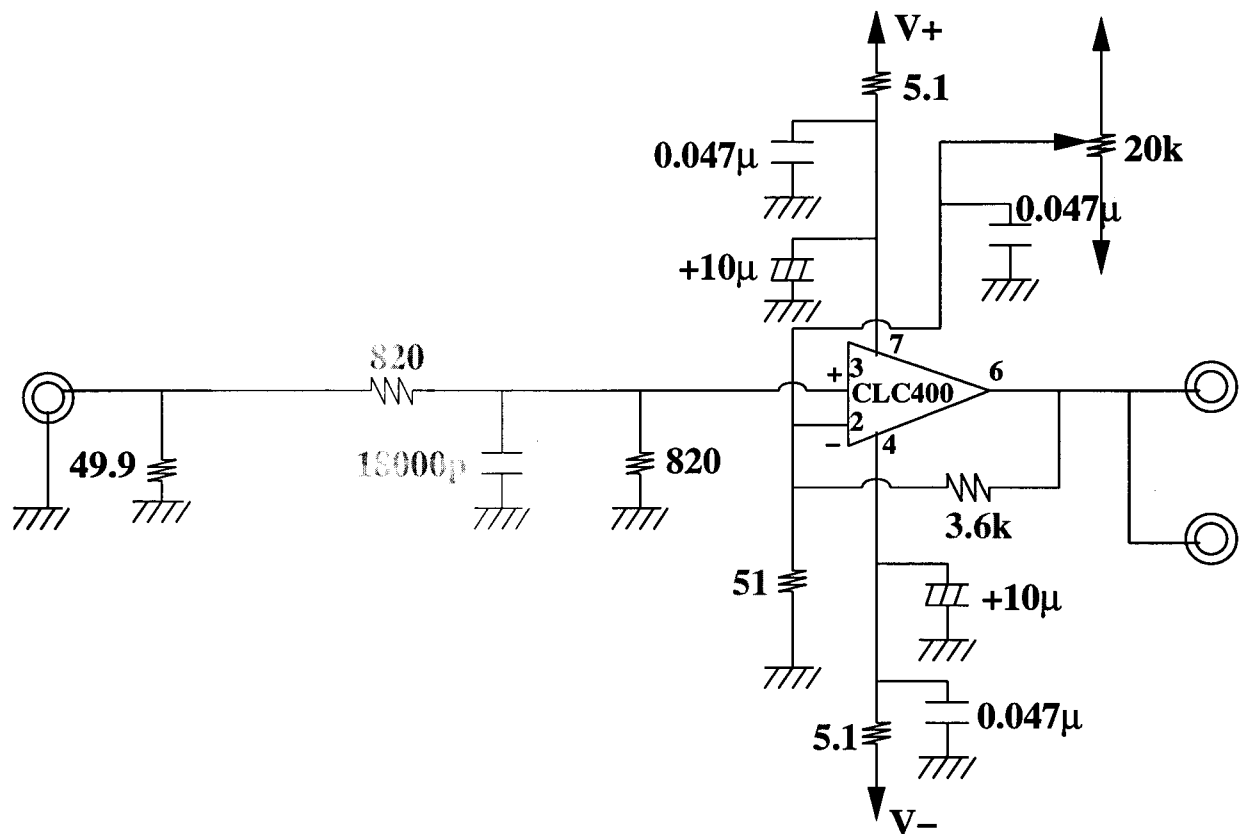
Fig. 4-2 A schematic circuit diagram of the timing filter amplifer. Differential Input Voltage; V±=6V. The shaping time is 1.5μs. In this case a feedback resistor is 3.6kΩ and then the gain;G is (51+3.6K)/51∼72.

By using the LED signal we were able to determine the efficiency as well as the energy resolution for such low energy signals. It is found that the detector system is sensitive to 2 keV signal with about 40 % efficiency [62]. And the result is shown in Fig 4-3.
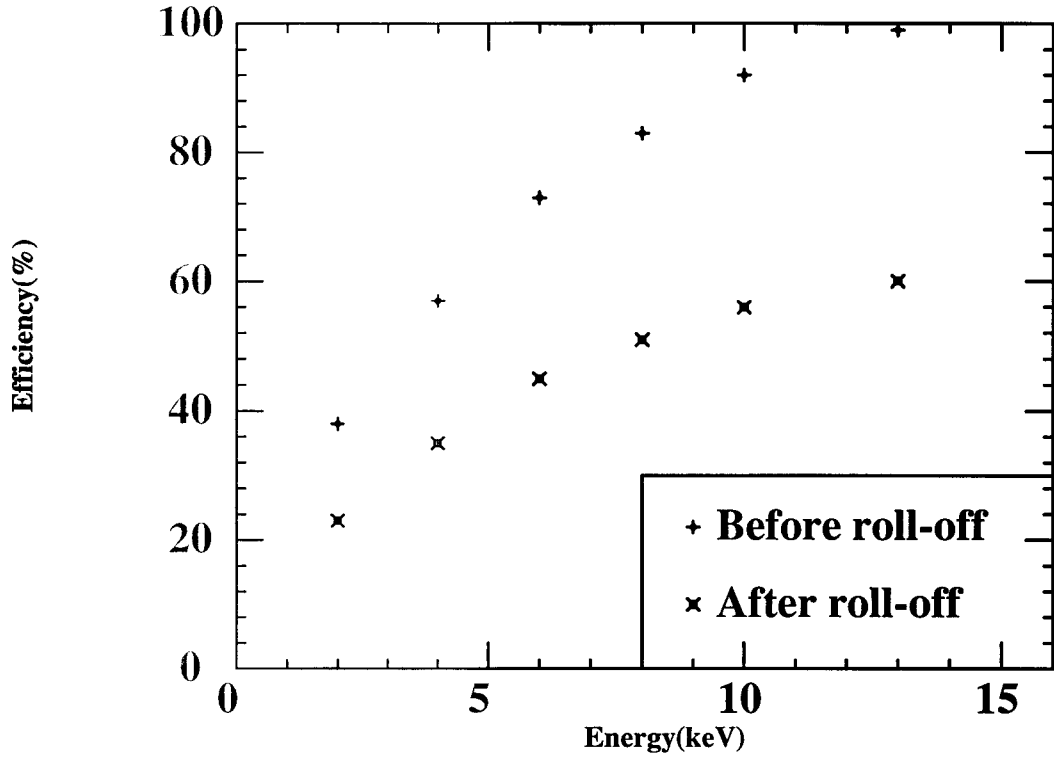
Fig. 4-3 The detection efficiency of ELEGANT VI in the low energy region.

However, a correction of the roll-off cut is needed for this result. By the roll-off cut the efficiency is reduced further. The roll-off ratio of the signal of 4 keV, which is generated by the LED is shown in Fig. 4-4. The roll-off selection is applied in the window of $R \leq \pm 0.3$. As for the signal 4 keV, the reduction of this cut is 39%. The result including this correction is also shown in Fig. 4-3.
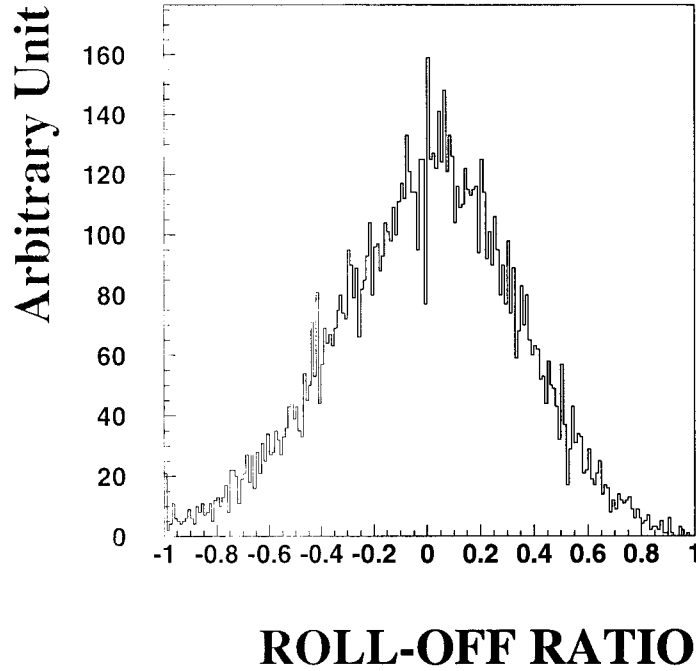
ROLL-OFF RATIO

Fig. 4-4 The roll-off ratio of the signal of 4 keV, which is generated by the LED.

It is noted here that in the low energy the timing of a signal behaves in a different way. Although a sum signal passes a long way to the coincidence circuit in Fig. 2-11, which takes about 30 ns normally in the case of no logic- delay, the event that a sum signal is more faster than a left and right signal occurs in the low energy region. In order to delay a sum signal and make an appropriate coincidence of a sum and a left/right signal, a logic delay of 105 ns was inserted between the discriminator(sum) and the coincidence circuit. This diagram of electronics is shown in the left dashed box of Fig. 2-11. Then the efficiency is improved in the low energy region like Fig. 4-3.

The relation of the pluse height and the energy of a real γ-ray and one photoelectron at the input to the discriminator is listed in Table 4-3. Then 1 keV corresponds to 8 mV and 17 mV for left(right) and sum signals, respectively. In the RUN, which was described in detail in Chapter 6, the energy thresholds are basically set at 8 mV and 10 mV for left(right) and sum signals, respectively. This is enough low to detect one photoelectron with the efficiency > 95%.

It is noted here that light detection efficiency can be improved even though a light output is naturally small. The interest in NaI(Tl) arises largely because it has high light output ($\sim$40 photons/keV) [70], while the photon light output of $CaF_2(Eu)$ ($\sim$20 pho-

67

Table 4-4 The relation of the pluse height and the energy of a real γ-ray and one photoelectron at the input to the discriminator.

signal	input height	pulse to discri.:left,right gate width	energy	input height	pulse to discri.: gate width	sum energy
^{241}Am	480mV	4μs	60keV	1000mV	4μs	60keV
1 photon	25mV	300ns	0.6keV	15mV	600ns	0.35keV

tons/keV) is lower than NaI(Tl). These light output with 25% photomultiplier efficiency are 10 photons/keV and 5 photons/keV for NaI(Tl) and CaF$_2$(Eu), respectively. On the other hand, the actual light output of NaI(Tl) of ELEGANT V and CaF$_2$(Eu) of ELEGANT VI are 1.3 photon/keV(0.77 keV/photon) and 3 photon/keV(0.35 keV/photon), respectively. As a result the light detection efficiency of NaI(Tl) of ELEGANT V and CaF$_2$(Eu) of ELEGANT VI are 1.3/10~13% and 3/5~60%, respectively. Althogh this light collection of NaI(Tl) of ELEGANT V is small, this is due to the large volume (10.2×10.2×101.6 cm^3) and 13% is good for this type of very long NaI detector. In the case of UKDM collaboration's NaI(Tl)[71] the light output is almost the same as 1.6 photon/keV, however, in the case of France(Saclay) group's NaI(Tl)(1"by 1"crystal) the light output is 10 photon/keV and ideal [72].

Chapter 5

LIGHT OUTPUT RESPONSE OF NUCLEAR RECOIL

The energy dependence of the scintillation efficiency produced in $CaF_2(Eu)$ by recoiling calcium and fluorine recoils was measured in the 25-91 keV and 53-192 keV recoil energy intervals, respectively. The scintillation efficiency was found to be $11\sim 20\%$, and $9\sim 23\%$ for F and Ca respectively. The scintillation efficiencies in $CaF_2(Eu)$ crystal increase with decreasing recoil energy, which is firstly suggested by the measurement of Davies *et al.*. It is also suggested that the Eu doping appears to affect the efficiency for nuclear recoils.

69

5.1 Introduction

Dark Matter particles, if they exist, interact elastically with the nucleus, and the energy is deposited in the crystal by the recoiling nucleus [21]. This elastic scattering event deposits several keV of kinetic energy in the nucleus.

In a scintillation detector, the nuclear recoil energy is converted into scintillation photons. The light output for Ca and F recoils is expected to be lower, at a given energy, due to several factors. One reason is that only a fraction of the nuclear recoil energy is transferred to electron excitation. The observed energy (pulse height) E_0 is, for simplicity, given as

$$E_0 = fE_R, \tag{5.1}$$

where E_R is the recoil energy and f is the conversion (reduction) factor of the pulse height for the recoiling nucleus with respect to the electron. We need to calibrate this f-value of our scintillation crystal, because this scintillation efficiency (f-value) depends on the scintillator, the activator concentration, and the recoil energy. Such an experiment was done recently by UK Collaboration [53] and the Beijing/Paris/Rome/Saclay Collaboration [44] for calcium and fluorine through neutron-nucleus scattering. Between these measurements there is a contradiction in the energy dependence of the scintillation efficiency. We have performed an experiment which extend the previous results [53][44] down to recoil energies of 25keV and 53keV for calcium and fluorine respectively. This is also important to reach the meaningful region for dark matter search.

5.2 Experimental setup

5.2.1 Pulsed-monoenergetic neutrons

The response of the detector to the nuclear recoil was measured by the ^{19}F(n,n') and the ^{40}Ca(n,n') reaction. Fig. 5-1 shows the neutron scattering apparatus used in the experiments described here. A pulsed neutron beam was produced by bombarding a deuterated titanium target with a pulsed 0.75MeV deuteron beam from a 3.2MV Pelletron Accelerator at Tokyo Institute of Technology by the d(d,n)^{3}He reaction. We used pulsed neutrons to determine the neutron energy by a time-of-flight- (TOF) method and to discriminate true events from those due to thermal neutrons. The average beam current was 2μA at a repetition rate of 2MHz. Details of the experimental apparatus of the beam line are described elsewhere [73]. The ~3.7 MeV neutron gives similar energy to a ^{19}F nucleus as the scattering by the dark matters. Time-of-flight measurements made with a liquid scintillator placed in the forward direction indicated a spread in neutron energy of around 0.26MeV (1σ). The main contribution to this spread comes from the deuteron energy loss in the primary target of Tid$_2$ with the thickness of 0.5?mg/cm^2,

70

which was made by d_2 gas electrolyzed on a titanium support (which also served as a deuteron beam stop). The neutron flux achievable is about $2 \times 10^7 /s/sr/\mu A$. Neutrons emitted at $0°$ were selected by placing a paraffin collimator, a 60cm long, cylinder with a tapered hole along the beam axis, 1cm in diameter near the neutron source and 3cm in diameter near $CaF_2(Eu)$ detector.
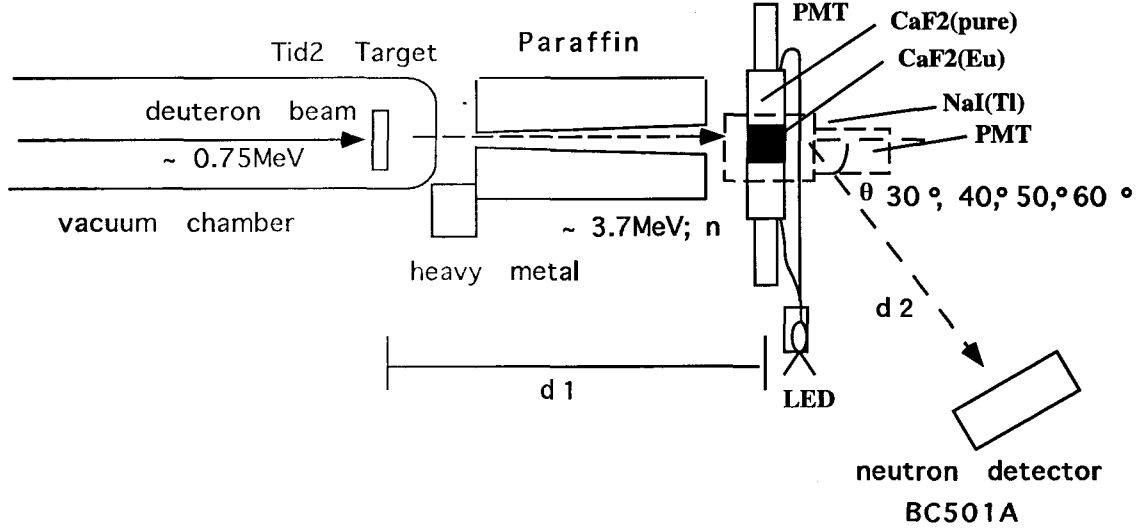
Fig. 5-1 Schematic of neutron scattering apparatus. Working conditions correspond to $d_1 = 80cm$, $d_2 = 200cm$, θ from $30°$ to $60°$.

5.2.2 The CaF_2 detector

The target $CaF_2(Eu)$ detector used for the experiment is the $CaF_2(Eu)$ crystal with the dimension of 45mm cube and europium doping content of 0.17%, having light guide of pure CaF_2 crystals coupled to photomultipliers. The tube is 1.5 inch Hamamatsu H3178 (quartz window). The light output of CaF_2 is small ($\sim$20photons/keV) so we want to cover maximum area to obtain maximum light collection efficiency. Then we obtained the light collection efficiency of 60% (0.35keV/photon). The $CaF_2(Eu)$ detector used here is the same doping as used in the dark matter detector itself, and the $CaF_2(Eu)$ crystals were obtained from BICRON and has been purified to the level about 0.05ppb for U and 0.24ppb for Th. The linearity of the ionization response of the $CaF_2(Eu)$ was checked with an energy calibration system by light emitting diode(LED)[63]. This LED (NLPB520 Nichia Chemical) is the world's first bright blue LED and almost the same as the maximum fluorescense emission wavelength of the $CaF_2(Eu)$. This light is sent to both sides of the crystals through optical fibers (BCF98 BICRON). The signal below

71

5keV cannot be tested by a radioactive source thus we generated the pulse shape of the low energy signal by the LED. It is verified that the signal has the similar shape as the real gamma ray signal. Periodic checks on the stability of the system were also done by lightening the LED with rate of 1Hz during the experiment. By using the LED signal we observed the pedestal energy shift of 1.6keV between beam-on time and beam-off time. Typical energy resolution as measured with the ^{241}Am 59.5keV γ ray is about $\Delta E/E = 25\%$(FWHM). The time resolution of CaF2 was measured to be 8 ns in FWHM at $\sim$1 MeV γ ray.

5.2.3 The neutron detector and NaI detector

The low energy signal from the detector was measured in coincidence with scattered neutrons detected by a BICRON BC501A liquid scintillator, 20cm$\phi\times$ 5cm, viewed by Hamamatsu R4144 photomultiplier. This was positioned 2m from the CaF$_2$(Eu) target with scattering angles of 30°, 40°, 50°, and 60°. Kinematics then difines the recoil energy in the target. Recoil energies of 53, 90, 135, and 192 keV, 25, 43, 65, and 91 keV for F and Ca were selected respectively. The heavy metal with the thickness of 10cm was positioned between the primary Tid$_2$ target and the neutron detector so as not to be exposed to neutrons and γ ray coming directly from the Tid$_2$ target. Then this shielding cut down the singles rate in the neutron detector to limit random coincidences.

The liquid scintillator is sensitive to both γ rays and neutrons; these events were separated by using a standard pulse shape discrimination (PSD) method. The typical distribution of the pulse height which depends on scintillation decay time, versus the pulse height proportional to the rise time, recorded by ADC is shown in Fig. 5-5(Left). Only events which produced a recoil proton pulse height in the BC501A with a value > 1.2 MeV were included so as to reduce background coincidences, which comes from detection of wall scattered neutrons. The BC501A detector was calibrated with the ^{88}Y 898 and 1836 keV γ ray, while NaI(Tl) detector was calibrated with ^{22}Na 511 and 1275 keV γ ray. The neutron pulse height response of the BC501A was found to be in agreement with the calculation of V. V. Verbinski et al. [74]. The time resolution of BC501A was measured to be 2.2ns in FWHM at $\sim$1 MeV γ ray (corrsponding to $\sim$3 MeV n). Then, it is sufficient to resolve γ ray ($\sim$7ns at 2m) and n ($\sim$60ns at 2m, which was calculated by $\beta = v/c = 9\%$ of 3.6$\sim$3.8MeV neutron).

Two NaI(Tl) scintillators, each with the dimensions of 85 × 95 × 95 mm^3 are placed just above and below the CaF$_2$ scintillator to detect escape γ ray events. Use of the paraffin collimator prevented also the NaI(Tl) detector from seeing the neutron source directly.

5.2.4 Electronics and procedure

The decay time of the CaF_2 detector is quite long ($\sim 3\mu$sec) and the transit time of a pulse through the PMT was about 0.04 nsec. The output pulses from the PMTs were fed into the developed high-gain Timing Filter Amplifier (TFA) with an RC circuit of time constant 200ns. In a few photoelectron level the time jitter of each pulse becomes enlarge, then each pulses were fed again into the TFA with a time constant $1\mu s$ after summing the left and right pulses. The signals from the two photomultipliers were separately discriminated at the level of one photoelectrons, which energy corresponds to 0.35keV and circuit noise can be kept below 0.30keV and then put in coincidence for triggering purposes. Then only pulses above a threshold of 2 photoelectons occuring in coincidence with neutron events in the BC501A neutron counter were accepted. We developed low noise circuit and system, which allowed us to extend our measurements down to the recoil energy of 25 and 53 keV for Ca and F, respectively.

The pulse heights from the CaF_2(Eu), BC501A, and NaI(Tl) detectors and the relative timing among the BC501A, CaF_2, and the deuteron beam pulses as determined by an inductive pickup coil were digitised and recorded through CAMAC-SFVME-SUN(Spark Station) on magnetic disc for each event, which was used as the main data acquisition system. A schematic of the electronics is shown in Fig. 5-2(A)(B). In this measurements there are three trigger mode such as dark matter mode (DM), double beta mode ($\beta\beta$) and LED mode (LED). The detector is designed to be used also for the search of the $\beta\beta$ decay of ^{48}Ca. The ^{40}Ca(n,n') reaction was used to excite the first 0^+ state (3.35MeV) in ^{40}Ca. The 0^+ state decays exclusively by the emission of e^+e^- pair thus energy calibration was carried out up to 3.3MeV [63]. This reaction was recorded simultaneously in separate analog-to-digital converters (ADC's) and the above three trigger modes was distinguished by using the different logic size of the trigger. Typical trigger distribution of the scattering angle of 50° degree is shown in Fig. 5-3. About 90% of total trigger rate is the $\beta\beta$ mode, and that of DM and LED modes are $\sim 3\%$ and $\sim 6\%$, respectively. The energy threshold of $\beta\beta$ mode is about 1.6MeV.

The required time of measurements depends on the cross section of each scattering angle, but the average time is about 3 hours. For each event, the following selections were required in the off-line analysis to select the true Ca/F recoil events.

i) The dark matter (DM) trigger including the rejection of the overflow in the left and right ADC. (The full range of the DM-ADC is about 150keV.)

ii) The events in central crystal of CaF_2(Eu) are selected by setting a proper window on the roll-off ratio spectrum [65].

iii) CaF_2(Eu) spectra were obtained by single events requiring only a neutron time-of-flight signature or a PSD signature. The high energy γ and low energy n cuts in

the neutron detector which suppresses the $\gamma\gamma$ and nn peak and reduces the random events background.

These background reductions are shown in Fig. 5-4. The raw total trigger rate at the scattering angle of 60° degree is about 100 cps and the coincidenced singles rate is a few cps.

experimental room
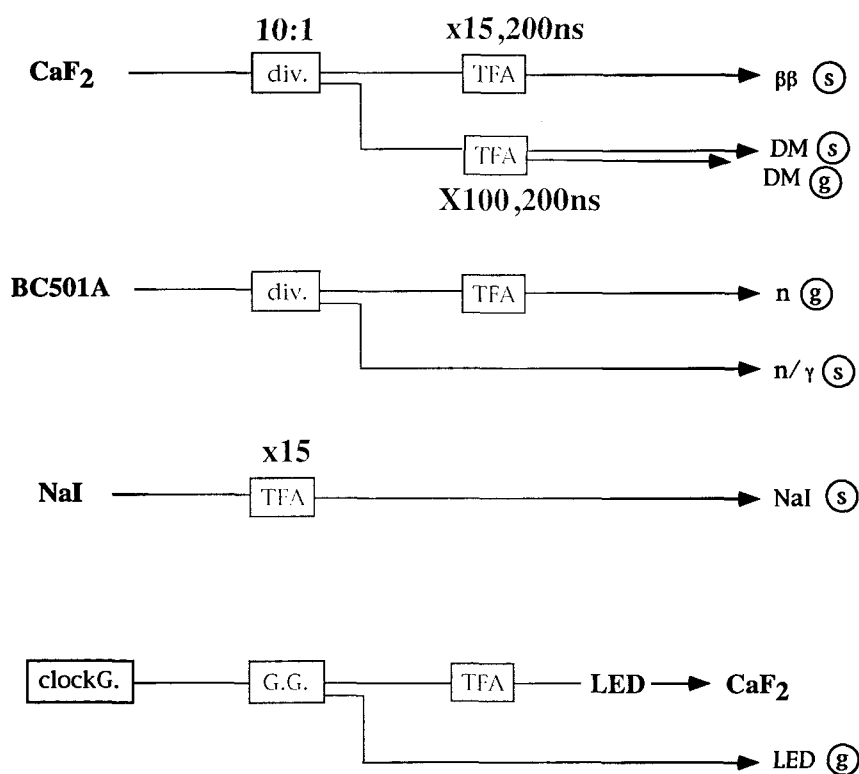
Fig. 5-2(A) Schematic of the electronics chain at experimental room.

counting room
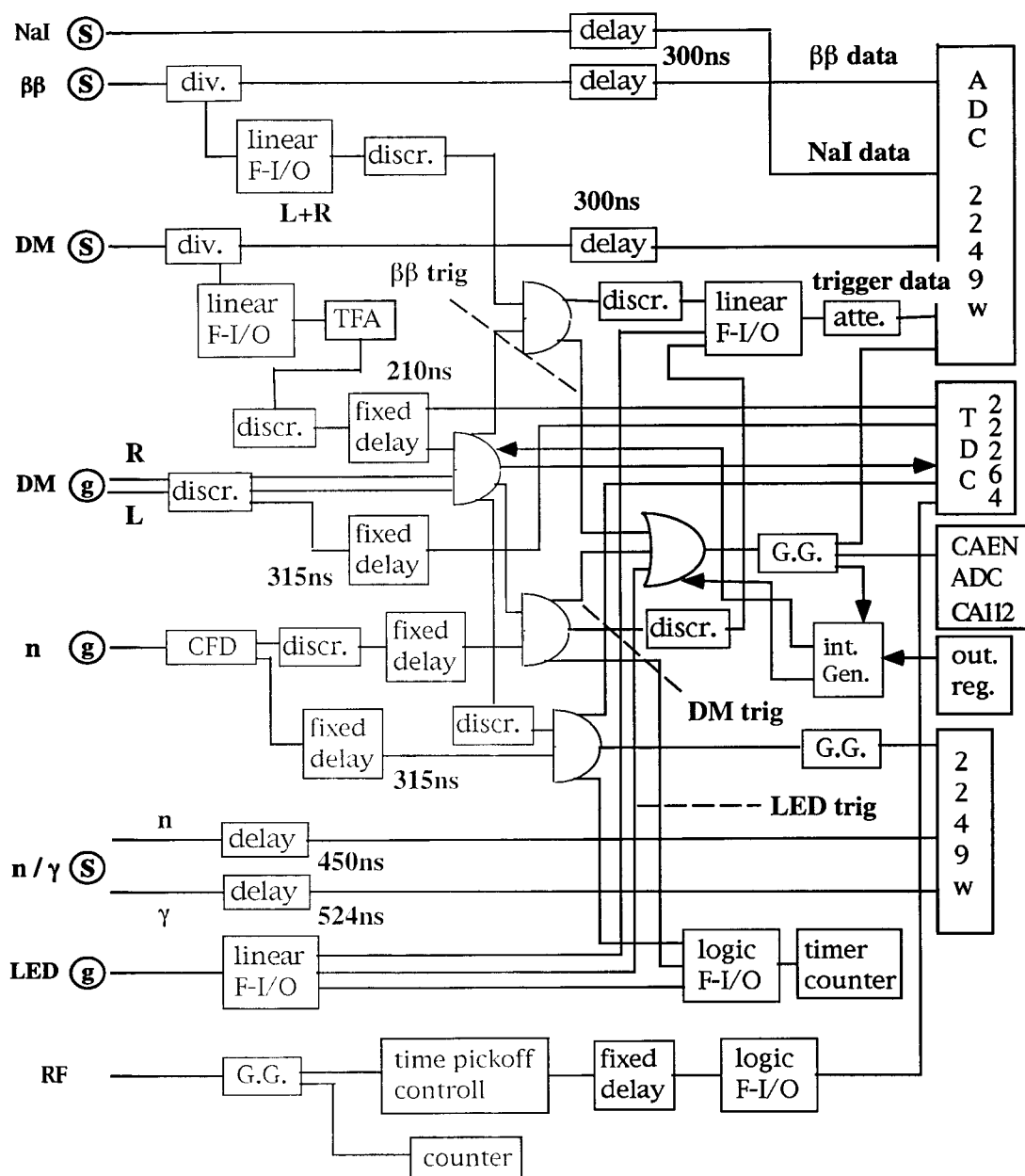
Fig. 5-2(B) Schematic of the electronics chain at counting room.
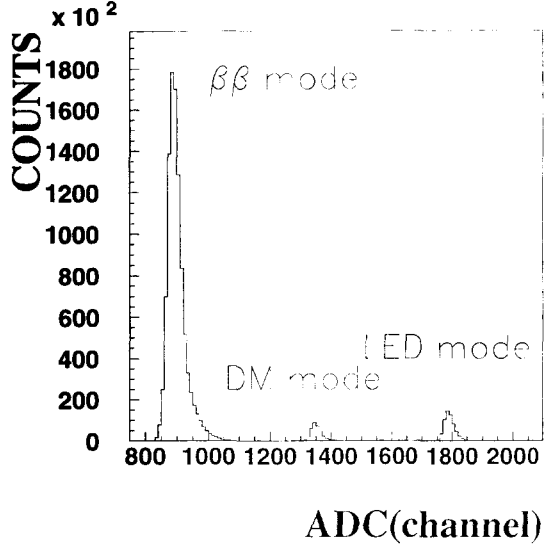
Fig. 5-3 Typical trigger distribution of three modes with the scattering angle of 50° degree. Three trigger modes are dark matter (DM) mode, double beta ($\beta\beta$) mode and LED (LED) mode.

5.3 Results

A tail can be seen on the fluorine peak in Fig. 5-5. The tail occurs due to detection of decay photons that Compton scatter in the target scintillator depositing energy in addition to the recoil energy. In case of inelastic scattering on ^{19}F two excited levels are found at low energy (109.9 and 197.2 keV). The energy level diagram of ^{19}F is shown in Fig. 1-4. And the inelastic cross sections of these two excited states are also shown in Fig. 5-6. The cross sections of inelastic scattering depend on the spin and parity of the excited state.

This was confirmed by using the upper and lower NaI(Tl) counters. Only the events of F recoils are selected by gating the energy region of upper and lower NaI corresponding to the Compton scattering events. And the convolution of the γ events to n events in the PSD selection is less than 1%. A simulation with GEANT shows that 21% of photons originating in decay from excited states, interact within the crystal through Compton scattering. Among these events we can reject the events that escaped γ ray interact the upper and lower NaI(Tl) veto counter and the both side pure-CaF$_2$ light guide. As a results the effect of the inelastic events on the scatter peaks were calculated to be at a level of $\sim$ 6% and this was allowed for estimating the peak positions at each angle.
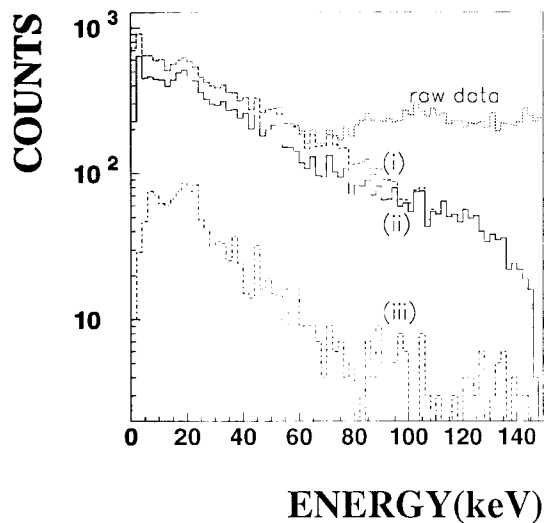
Fig. 5-4 Raw data: On-line energy spectrum of re-coiling F/Ca in CaF_2. (i), (ii) and (iii): Replayed energy spectrum after the selection (i), (ii) and (iii), respectively.
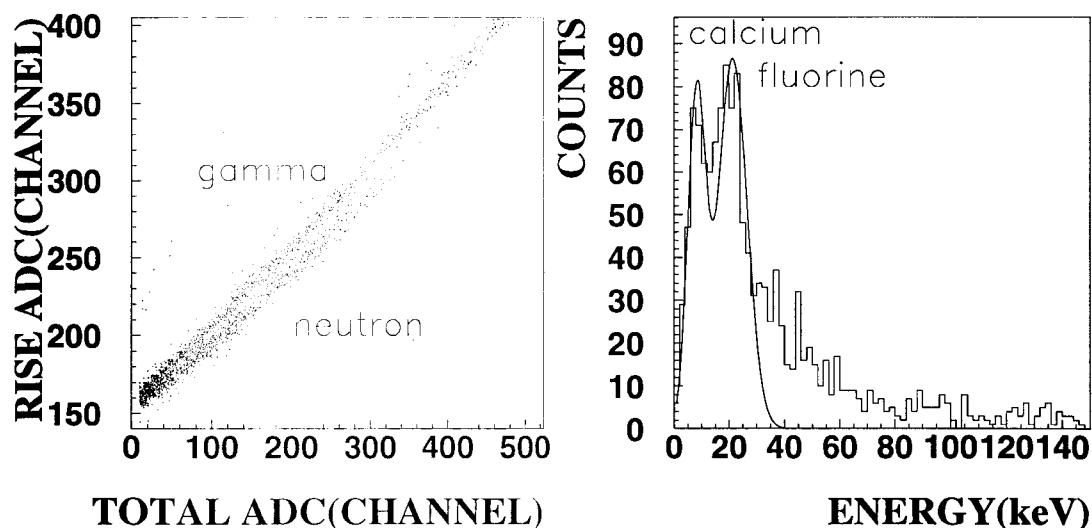
Fig. 5-5 Left: Typical distribution of the pulse height which depends on scintillation decay time, versus the pulse height proportional to the rise time, recorded by ADC of BC501A. Right: An example coincidence scatter spectrum for $CaF_2(0.17\%Eu)$ taken with a scattering angle of $60°$ using neutrons of energy of 3.7MeV. Two peaks are visible corresponding here to Ca and F recoils with energy of 91keV and 192keV respectively.

After background subtraction, the signal peaks were fitted with a Gaussian to determine the mean and the width of the observed energy distribution. In the fitting analyses the measured energy resolutions of the detector, the spread in neutron energy in the beam, and the mean scattering angles are used for the widths of the Gaussian peaks. Fig. 5-5. shows an example scatter spectrum for CaF_2(0.17% Eu) taken with a scattering angle of 60°. Two peaks are visible, corresponding here to the Ca and F recoils with energy of 91keV and of 192keV respectively. This was confirmed to be correct by comparing the relative count rates in the two peaks versus angle with calculations based on the known elastic scattering cross sections, which are shown in Fig. 5-7. Similar scatter spectra were observed at each angle.

Fig. 5-8 shows the scintillation response in keV for Ca and F recoils in CaF_2(0.17% Eu) obtained from the scatter spectra calibrated relative to electrons (photons) at each energy, versus the corresponding calculated recoil energy. For the purposes of calibrating dark matter detectors a plot of ratio of recoil efficiency to photon efficiency, versus recoil energy, may be more useful and this is also given in Fig. 5-8 for Ca and F respectively.

The only significant contributions to the vertical error bars in Fig. 5-8 are statistical and arise from peak finding with poor statistics and from the CaF_2(Eu) detector resolution. The uncertainty in the calculated recoil energy is due to the experimental geometry and beam energy.
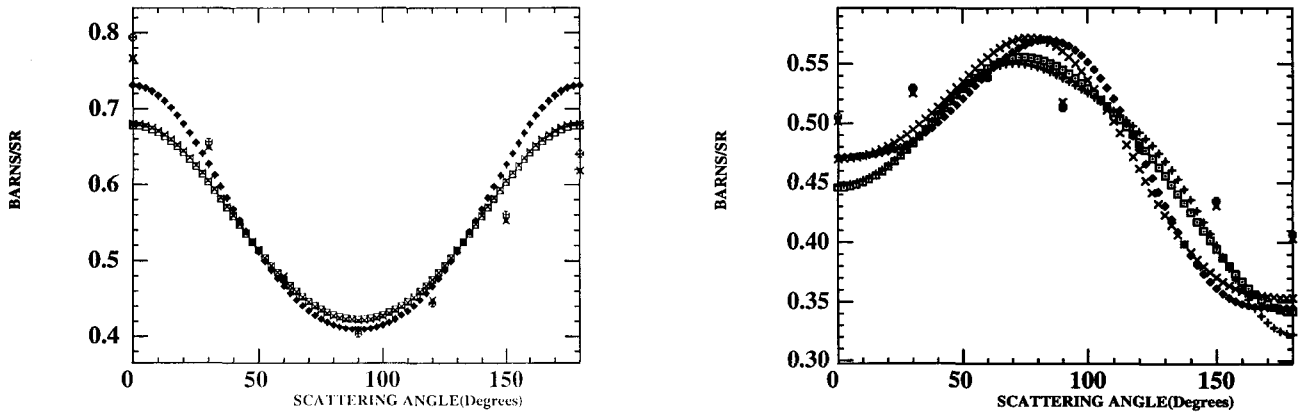
Fig. 5-6 Left: The differential cross section for inelastic scattering from the first excited state (0.110MeV) in ^{19}F. The energy of neutron projectile is 3~4 MeV. Right: The differential cross section for inelastic scattering from the second excited state (0.197MeV) in ^{19}F. These are obtained by the Database of BNL:NNDC (National Nuclear Data Center)[10].

Fig. 5-7 Left: The differential cross section for the elastic scattering of 3~4MeV

[10]IP address; bnlndz.dnc.bnl.gov(130.199.112.132)

78
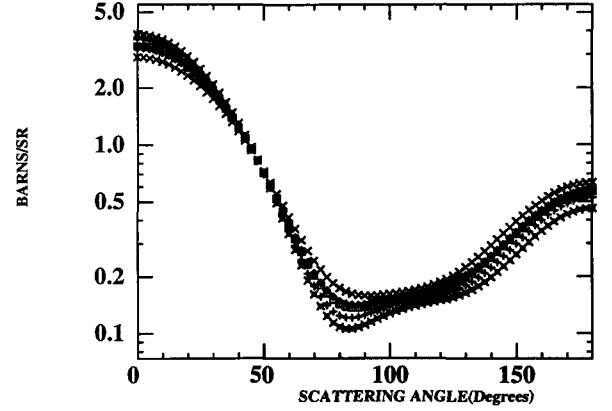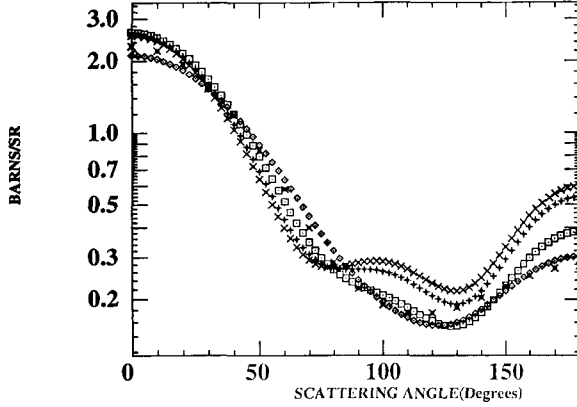
neutrons to the ground state of ^{19}F. This is also obtained by the Database of BNL:NNDC (National Nuclear Data Center). Right: The differential cross section for the elastic scattering of 3~4MeV neutrons to the ground state of ^{40}Ca.

So far the scintillation response of CaF_2(Eu) was measured by the BPRS(Beijing-Paris-Rome-Saclay) Collaboration [44] and the UK(United Kingdom) Collaboration [53]. The experimental conditions were summarized in Table 5-1.

The former group suggests the f-value does not depend on the energy. In contrast to the result of the BPRS group there is evidence from the data of the UK group that the f-value increase with decreasing recoil energy. We obtained the data which extend the UK's result down to recoil energies of 25keV and 53keV for Ca and F respectively and which are consistent with the UK's result.

It is also suggested that the Eu doping appears to affect the efficiency for nuclear recoils. R. B. Murray and A. Meyer calculated scintillation efficiency as a function of both dE/dx and activator concentration [76]. This indicates that for dark matter purposes we should perform calibration experiments using a scintillator with the same doping as used in the dark matter itself, because the activator concentration of the crystals used in the various experiments is surely not the same.

---

[11]The mol fraction of d_2/Ti is about 0.7~ 0.9%.

Table 5-1 The experiments of ^{40}Ca(n,n') and ^{19}F(n,n') are summarized. Wiconsin group measured the half-life of the first excited state of ^{40}Ca with ^{40}Ca(n.n')^{40}Ca reaction [75].

item/experiment	Wisconsin		
reaction for neutron production	^{2}H(d, n)^{3}He		
primary beam energy(n);MeV	3.52		
primary beam intensity			
target thickness (backing material)	deuterated polyethylene(200keV/5MeV)		
scattering angle of neutron(degree)	80		
solid angle of CaF$_2$ detector(msr)	20		
running time			
Yields			
cross section(mb);^{40}Ca(n,n')^{40}Ca(3.35)	22		
scintillation efficiency %(^{19}F/Ca)	-		
item/experiment	UK	BPRS	Osaka
reaction for neutron production	^{2}H(d,n)^{3}He	^{7}Li(p, n)^{7}Be	^{2}H(d,n)^{3}He
primary beam energy(n);MeV	3.2-5.5	1.9	3.83
primary beam intensity	10^9/s(isotropic)		10^{13}/s(isotr)
target thickness (backing material)	Tid$_2$		Tid$_2$^{11}
scattering angle of neutron(degree)	0	115	0
solid angle of CaF$_2$ detector(msr)		1.2	2
running time			~3hour at each angle
Yields			
cross section(mb);^{40}Ca(n,n')^{40}Ca(3.35)	-	-	
scintillation efficiency %(^{19}F/Ca)	12/8	6.9/4.9	11/9

5.4   Conclusion

In summary, we have observed recoils of calcium and fluorine nuclei of recoil energies in the range 25-91 keV and 53-192 keV in a $CaF_2(Eu)$ detector, respectively. The scintillation efficiency was found to be $11\sim 20\%$, and $9\sim 23\%$ for F and Ca respectively. These data serve to calibrate a $CaF_2(Eu)$ dark matter detector whose results are discussed in Ref. 12, 13, 14, 15.

It is emphasized here that we should pay attention to use a scintillator with the same doping as used in the calibration experiments itself for dark matter searches and take the energy dependence into account for a specific scintillator.
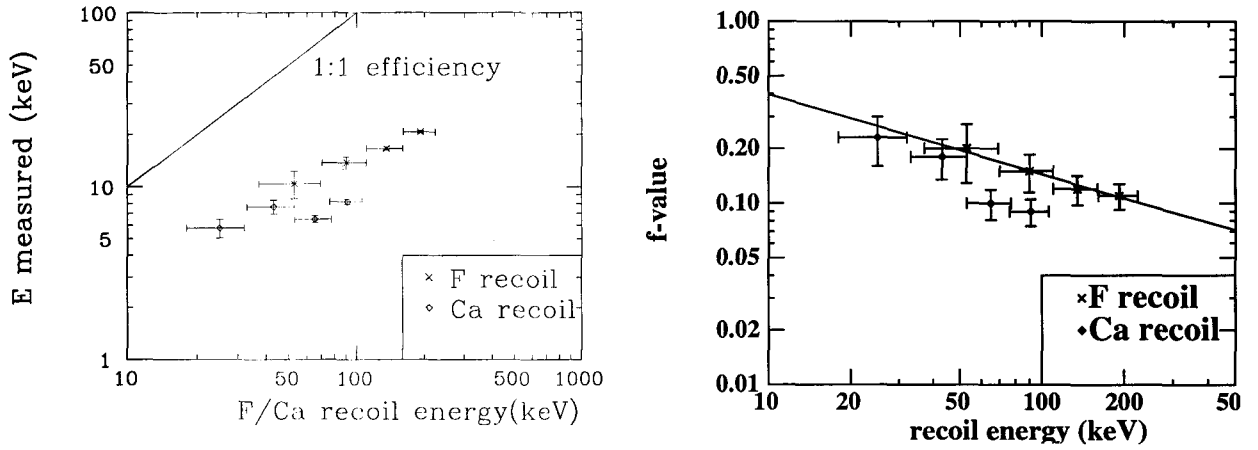
Fig. 5-8 Left: The scintillation response of $CaF_2(0.17\%Eu)$, calibrated relative to photons, versus calculated recoil energy for Ca and F recoils. Right: The ratio of recoil efficiency to photon response versus recoil energy in $CaF_2(0.17\%Eu)$ for Ca and F recoils.

81

Chapter 6

PERFORMANCE OF ELEGANT VI

6.1 Test run at Osaka University

The engineering run was carried out by using only 9 elements of CaF_2 detectors. Here outer detectors were used as veto counters for the central detector. This measurements was made at Osaka, the sea-level laboratory, for about 3.5 day (0.29×3.5 kg d) [65][77] [78][79]. 20 modules of CsI(Tl) detector was put around the CaF_2 detectors, however, in this measurements, these are not operated. There were 5 cm lead and copper shields. Radon gas, which is the radioactive gas contained in the air was not purged out. Trigger of the data acquisition was made only central CaF_2 module fires. The energy threshold was set at 2 photoelectrons ($\sim$ 0.7 keV). The noise level (the FWHM of the pedestal) is about 0.17 keV, and far below the trigger threshold. The trigger rate was about 3.5 counts per second.

The observed spectrum at the low energy region using the subset of ELEGANT VI is shown in Fig. 6-1. This spectrum is obtained after the following off-line analysis. Energy spectrum of all 9 CaF_2 modules are digitized by the gate of central CaF_2 trigger. Then if any one of outer 8 modules fires, i.e. if any one of outer 8 modules is larger than 3σ of its pedestal, the event of central CaF_2 is not selected. This off line veto is quite effective especially for the low energy region, because we can veto from zero energy without the threshold of any hardware such as discriminators and so on.

ENERGY(keV)
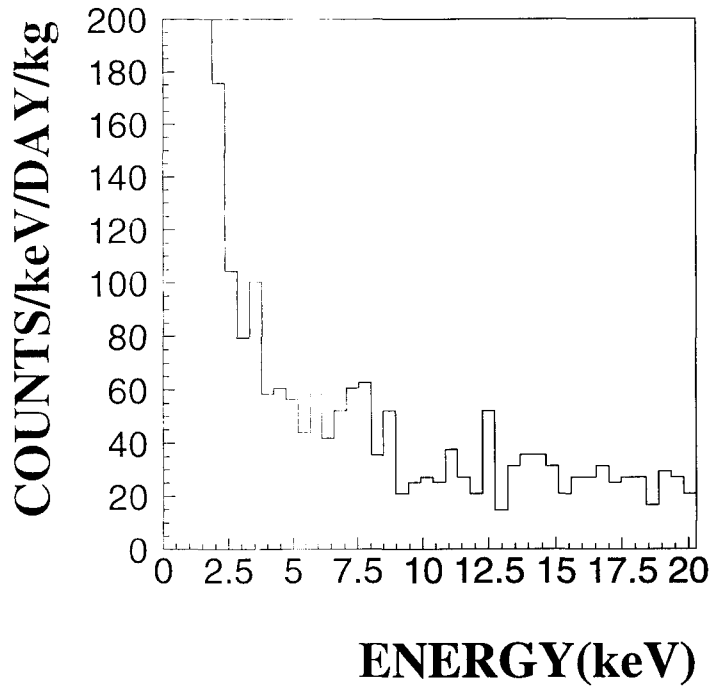
Fig. 6-1 A spectrum of the CaF_2 detector using surrounding 8 elements of CaF_2 as veto taken at the laboratory of Osaka Univ.(sea level). The vertical axis is given by counts/keV/kg/day.

The experimental condition is far below the final set up. However, the background level is already has similar precision as BPRS Collaboration [44].

6.2 Full operation at Osaka University

6.2.1 Experimental set up

1) **all 25-CaF_2 RUN**

At the first stage, a measurement was made to test the performance and the operation of ELEGANT VI. This measurements was carried out at Osaka, for about 16 hours (the live time of 7.0 hours); RUN001-006. There was only a conventional shield of an outer 10 cm layer of low activity lead and an inner 5 cm layer of OFHC copper. N_2 gas is circulated in the airtight container. Trigger of the data acquisition was made whenever at least one CaF_2 fires among all 25(24) modules (in reality one CaF_2 module: module #22 and two CsI modules(module #15 and 30) can not be used because of the PMTs were dead in the meantime unfortunately.)

In the following, the module number (#) is tagged on all CaF_2 and CsI modules for convenience, which is shown in Fig. 6-2. The trigger rate of 25(24) CaF2 and 40(38) CsI was about 150 cps and 9100 cps, respectively.

In this measurement it was found that the background level of each module is totally different. Histograms in Fig. 6-3. show the energy spectra of all(24) CaF_2(Eu)s in case that only central(Eu doped) CaF2 fires. It is the energy spectrum after the off-line cut of no-CsI fire, no other CaF_2 fire and roll-off selection, which effects are described in detail in Chapter 6.2.3. Roll off spectra of all(24) CaF_2 are also shown in Fig. 6-4. The central CaF_2(Eu) event rates of the module number of #7, 17, and 19 are especially high and these contributions owe to an internal background (U/Th). This fact is confirmed by an high energy spectrum, which is described in detail in Chapter 7.2.1. This central CaF_2(Eu) event rates are summarized in Table 7-1.

29/30	31/32	33/34	35/36	37/38	39/40
25/26	21	22	23	24	25	27/28
	16	17	18	19	20	
21/22	11	12	13	14	15	23/24
17/18	6	7	8	9	10	19/20
13/14	1	2	3	4	5	15/16
1/2	3/4	5/6	7/8	9/10	11/12

Fig. 6-2 Module numbers # are tagged on all CaF2 and CsI modules. This figure

84
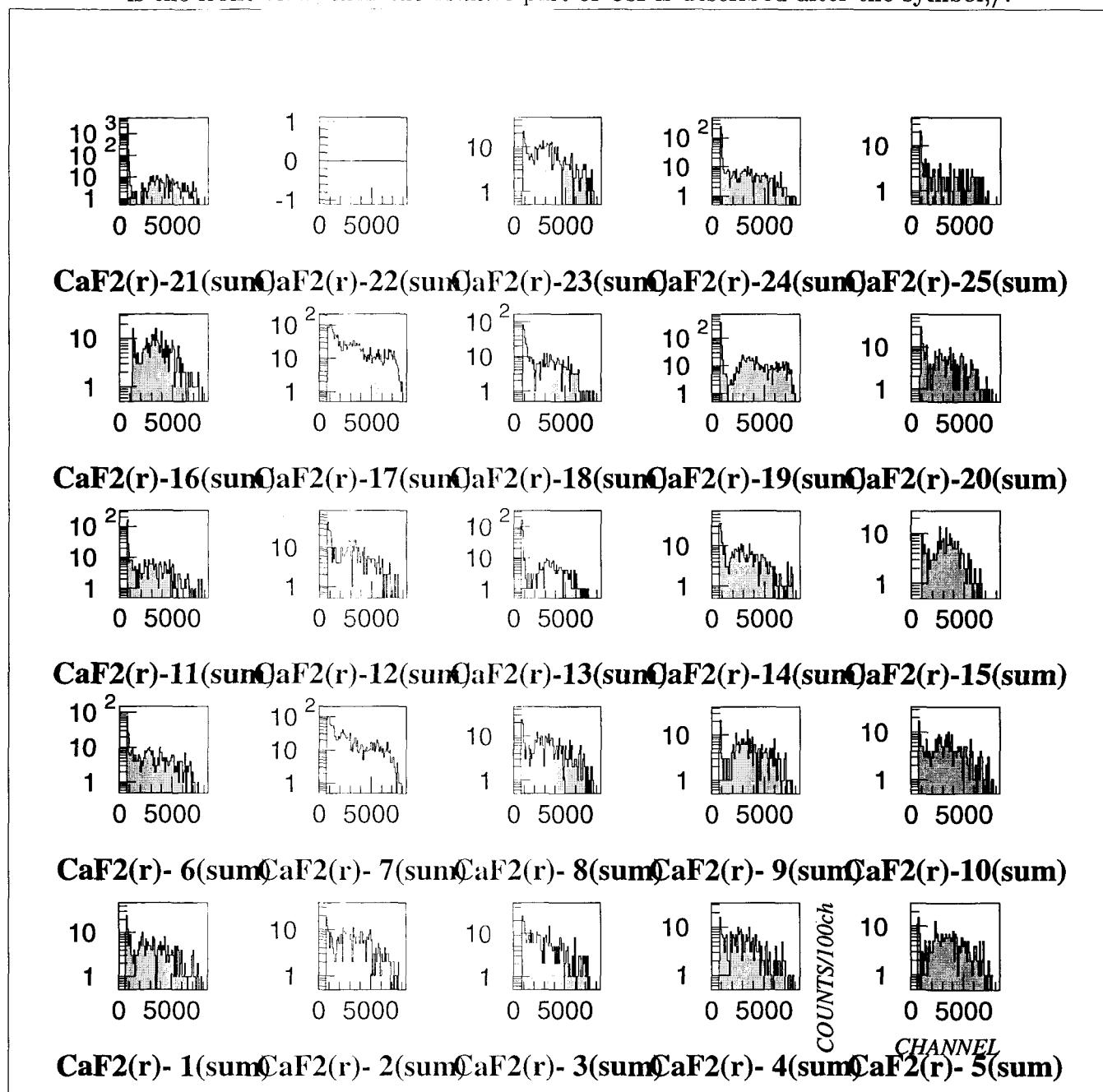
Fig. 6-3 Single spectra of all(24) $CaF_2(Eu)$s using surrounding other 24(23) elements of CaF_2 and 40(38) CsI detectors as veto and roll-off cut. The horizontal axis is given by CHANNEL and the full scale (8000ch) is about $\sim$350keV.

CaF2(v)-21(ratio)CaF2(v)-22(ratio)CaF2(v)-23(ratio)CaF2(v)-24(ratio)CaF2(v)-25(ratio)

CaF2(v)-16(ratio)CaF2(v)-17(ratio)CaF2(v)-18(ratio)CaF2(v)-19(ratio)CaF2(v)-20(ratio)

CaF2(v)-11(ratio)CaF2(v)-12(ratio)CaF2(v)-13(ratio)CaF2(v)-14(ratio)CaF2(v)-15(ratio)

CaF2(v)- 6(ratio)CaF2(v)- 7(ratio)CaF2(v)- 8(ratio)CaF2(v)- 9(ratio)CaF2(v)-10(ratio)

CaF2(v)- 1(ratio)CaF2(v)- 2(ratio)CaF2(v)- 3(ratio)CaF2(v)- 4(ratio)CaF2(v)- 5(ratio)
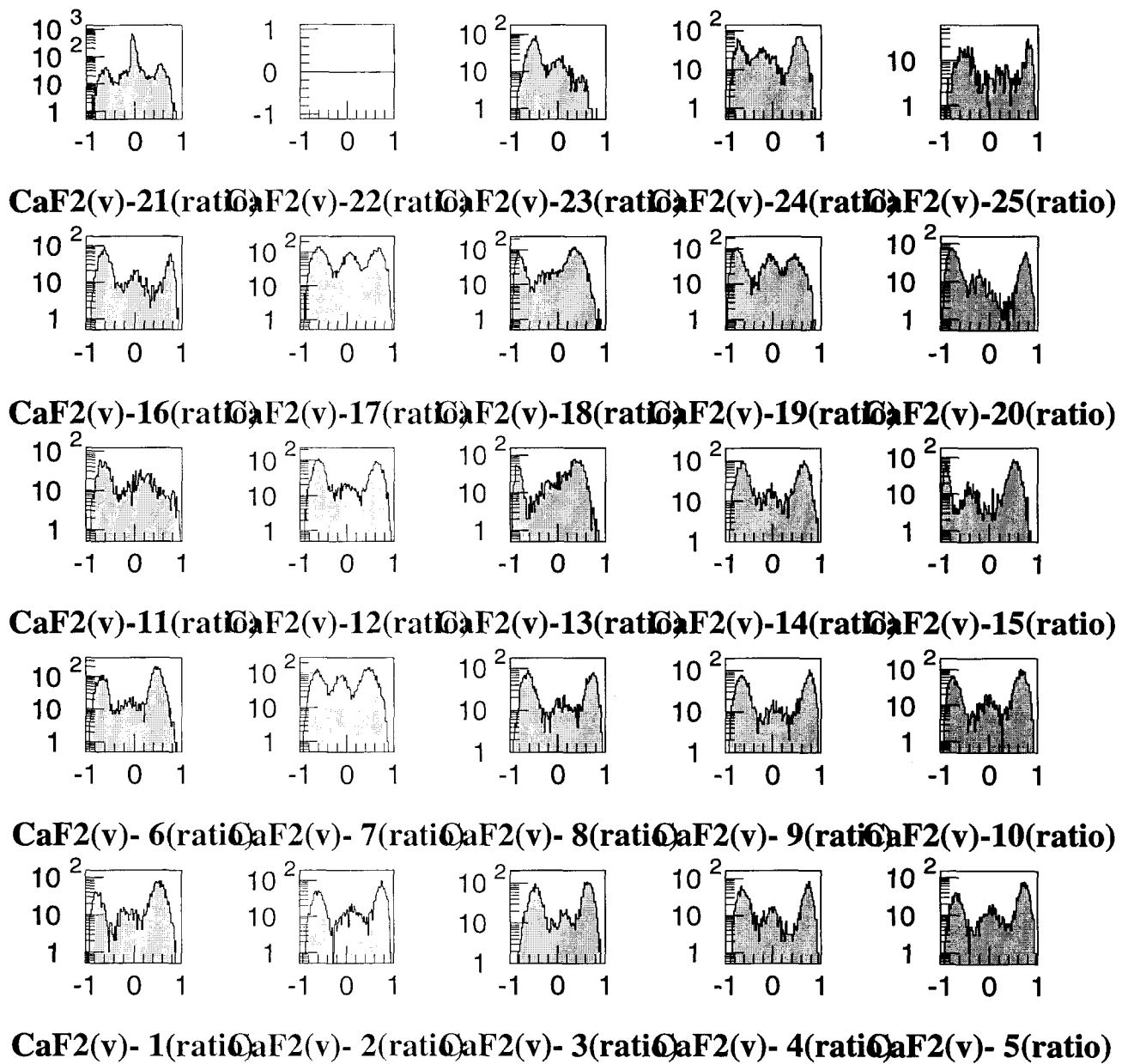
Fig. 6-4 Roll off spectra of all(24) CaF_2.

Table 6-1 The central $CaF_2(Eu)$ event rates of all(24) CaF_2 modules. This rate is integrated of all energy region of dark matter range ($\sim$ 350 keV).

module number #	event rate (conuts/hour) before roll-off	after roll-off	BG
1	273.	40.3	
2	280.	50.6	
3	402.	51.9	
4	247.	38.3	
5	232.	41.1	
6	559.	55.1	
7	769.	204.	high
8	351.	51.9	
9	351.	41.7	
10	314.	40.9	
11	221.	60.3	
12	456.	63.6	
13	314.	63.7	
14	414.	54.6	
15	246.	34.1	
16	261.	45.7	
17	850.	242.	high
18	466.	75.6	
19	488.	151.	high
20	247.	39.4	
21	612.	454.	(high)
22	-	-	
23	214.	60.1	
24	327.	96.7	
25	101.	20.0	

It is noted here that in this RUN the noise level of module number; #13, 19, 21 and 24 of CaF2 was high and the threshold level of these modules was raised to 50, 80, 50 and 30 mV, respectively. In this RUN the gain of each module was not matched precisely and the noise level of each module was also different. As a result the energy threshold levels are different. Then please do not take these numbers seriously.

2) selected 9-CaF$_2$ RUN

Based on the all 25-CaF$_2$ RUN, the configuration of CaF$_2$ module has been changed to Fig. 6-5. The modules of low event rate were selected and positioned in central 9 modules and #7, 17, 19 modules are disposed to the edges or outer layer of all CaF$_2$ modules.

29/30	31/32	33/34	35/36	37/38	39/40
25/26	21 (7)	22 (18)	23 (21)	24 (17)	25 (4)	27/28
21/22	16 (23)	17 (14)	18 (25)	19 (15)	20 (24)	23/24
17/18	11 (6)	12 (2)	13 (9)	14 (5)	15 (8)	19/20
13/14	6 (16)	7 (10)	8 (20)	9 (12)	10 (22)	15/16
1/2	1 (13)	2 (1)	3 (3)	4 (11)	5 (19)	11/12
	3/4	5/6	7/8	9/10	

Fig. 6-5 The configuration of all CaF2 modules has been changed. The module number# in parenthesis is the module numbers at the previous all 25-CaF$_2$ RUN.

6.2.2 Measurements

Measurements were carried out from 5 Jun. 1997 to 22 Sep. 1997. In order to examine the backgrounds and check the effects of passive shields, which are described in Chapter 2.3.2, measurements are carried out on each process constructing the complete shieldings of ELEGANT VI. These runs can be devided into following three types.

88

a) RUN-011, 012, 013 series

This series is mainly for examining the backgrounds and checking the effects of passive shields. Some improvements or changes were made in this series by taking into account the result of the previous RUNs.

b) RUN-014 series

The final setup of the shieldings of ELEGANT VI was completed in this series. The measurements after the completion were carried out from 6 Aug. 1997 to 2 Sep. 1997 for about one month. The total measuring time and the total live time is 13.4 and 8.14 days, respectively. The rest of the time of one month was dedicated to 'calibration RUNs' which were the calibration of a monitor's CaF_2 by radioactive sorces and the LED signal and 'backgrounds search RUNs' which were triggered by 40 CsI(Tl) modules. The 'calibration RUNs' were routinely carried out every second week and which were described in detail in Chapter 7.1.

c) RUN-015 series

This series was focused on the survey of backgrounds events which was not conducted by the previous (a) and (b) series.

Trigger of the data acquisition was made whenever at least one CaF_2 fires, however, in this selected 9-CaF_2 RUN, the energy threshold of central 9 modules and outer layer of 16 modules are set separately as follows (see Table 4-4 for the corresponding energy),

module		discriminator	threshold (-mV)
outer layer of 16 modules	$\Longrightarrow$	L/R	200
	$\Longrightarrow$	sum	400
central 9 modules	$\Longrightarrow$	L/R	5~9
	$\Longrightarrow$	sum	9~15

It is noted here that all the 25 modules of CaF_2 can be used for the study of $\beta\beta$ decays of ^{48}Ca.

6.2.3   Background reduction

In the followings, the backgrounds reduction and the effects of active veto and passive shieldings are described separately.

1) Active shields

The following selections were applied in the off-line analysis to select possible candidates for the true dark matter recoil events of the present interest.

89

i) CsI anti-veto

There are no signals from 40 CsI(Tl) detectors. The CsI detectors are triggered by only at least of one CaF$_2$ detectors fires.

ii) CaF$_2$ anti-veto

There are no signals from other CaF$_2$ detectors than itself. In the off-line data analysis of these (i) and (ii) requirements, no signals means that its ADC-value is lower than 3σ of its pedestal. The accidental cut of its own is estimated by this 3σ cuts to be $0.27\% \times 24 \sim 6\%$.

iii) roll off selecton

Rejection of events with $|R| \geq 0.3$, where R is the roll-off ratio. Hence only events in the central CaF$_2$(Eu) are selected.

The energy spectra of the residual events after each cut and the reduction ratio at each position of central 9 CaF$_2$ are shown in Fig. 6-6.

90
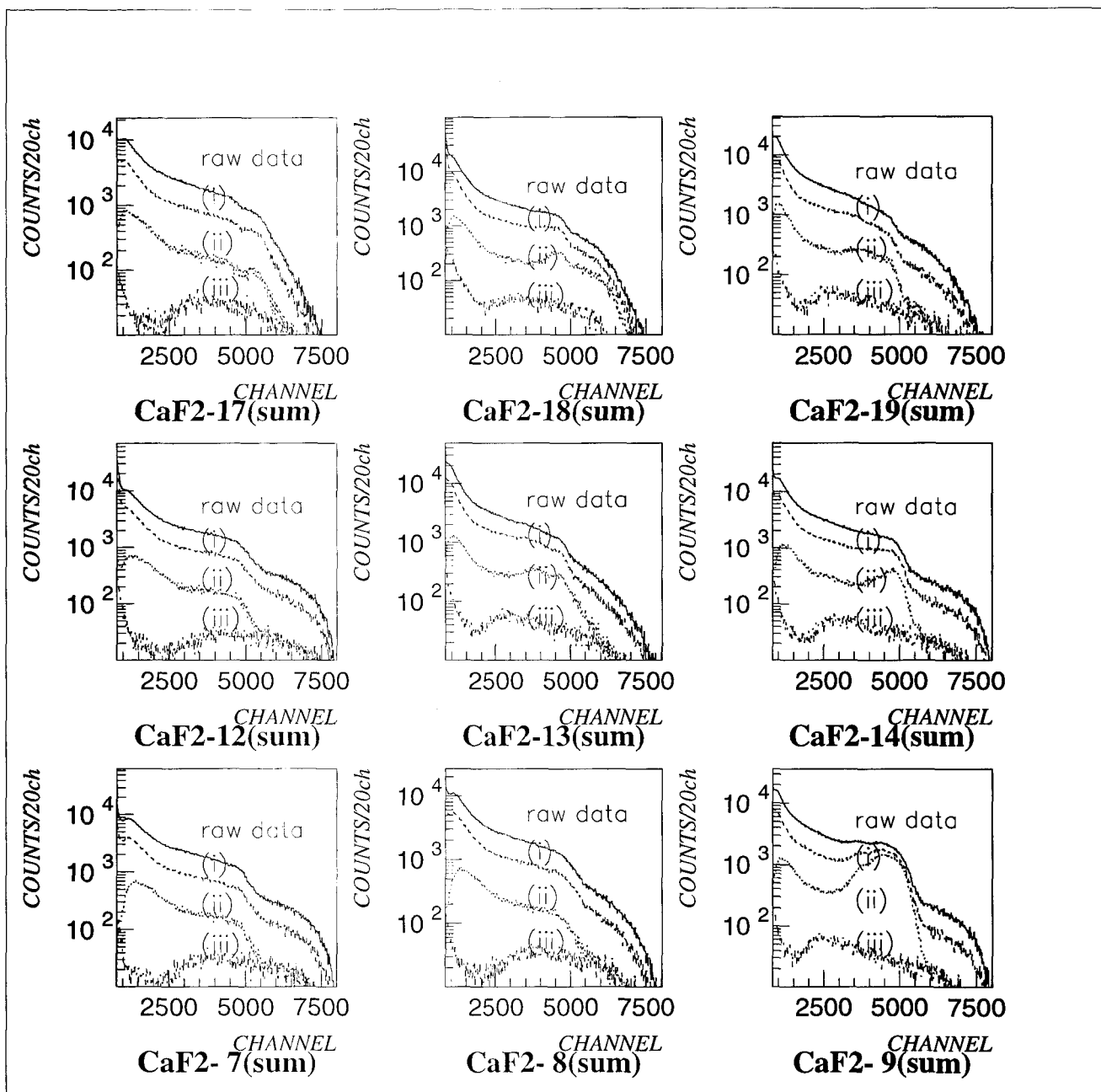
Fig. 6-6 Energy spectra of the central 9 CaF_2 detectors obtained at sea-level, Osaka. (raw data) in the full shieldings and N_2 gas circulation, measured for 8.1 days(RUN-014 series); the raw energy spectrum, (i) in anti-coincidence with 40 CsI(Tl) detectors, (ii) in anticoincidence with the 40 CsI and 24 CaF_2 detectors, (iii) in anticoincidence with the 40 CsI, 24 CaF_2 detectors, and the light guides of pure CaF_2 scintillators(roll-off cut).

91

It is emphasized here again that these anti-veto is not so effective especially for the low energy region until the off-line veto are applied. An event is not vetoed from zero energy as long as using the hard-veto of any hardware such as discriminators and so on. And the selection of (iii);roll-off cut is quite effective of the low energy region until about 6000 ch($\sim$ 200 keV).

A histgram of module #9 has a bump around 5000 ch until the selection of (iii) are applied. This is expected to be a backgrounds from the side crystals of pure CaF_2, which was confirmed from the roll-off ratio spectrum as shown in Fig. 6-7. The left crystal of pure light-guide CaF_2 is the origin of this bump.

These effects of active shields are compared with the energy spectrum of the high energy region in Fig. 6-8, which was measured for the study of double beta decays of [48]Ca simultaneously. There are two bumps in Fig. 6-8. The bump around 5 MeV is due to the through-going cosmic ray muons in the light guides of pure CaF_2. The energy losses of muon in the CaF_2 crystal is estimated by the minimum ionization as follows,

crystal	density(g/cm^3)	thickness(cm)	light yield		energy loss(MeV)
CaF_2(Eu)	3.18	4.5	1	$\Longrightarrow$	21$\sim$29
CaF_2(pure)	3.18	4.5(7.5)	1/4	$\Longrightarrow$	5(9)$\sim$8(12)

And the bump around 8 MeV is the overflow of both light outputs from the both sides of PMT in ADC.

roll-off ratio:R
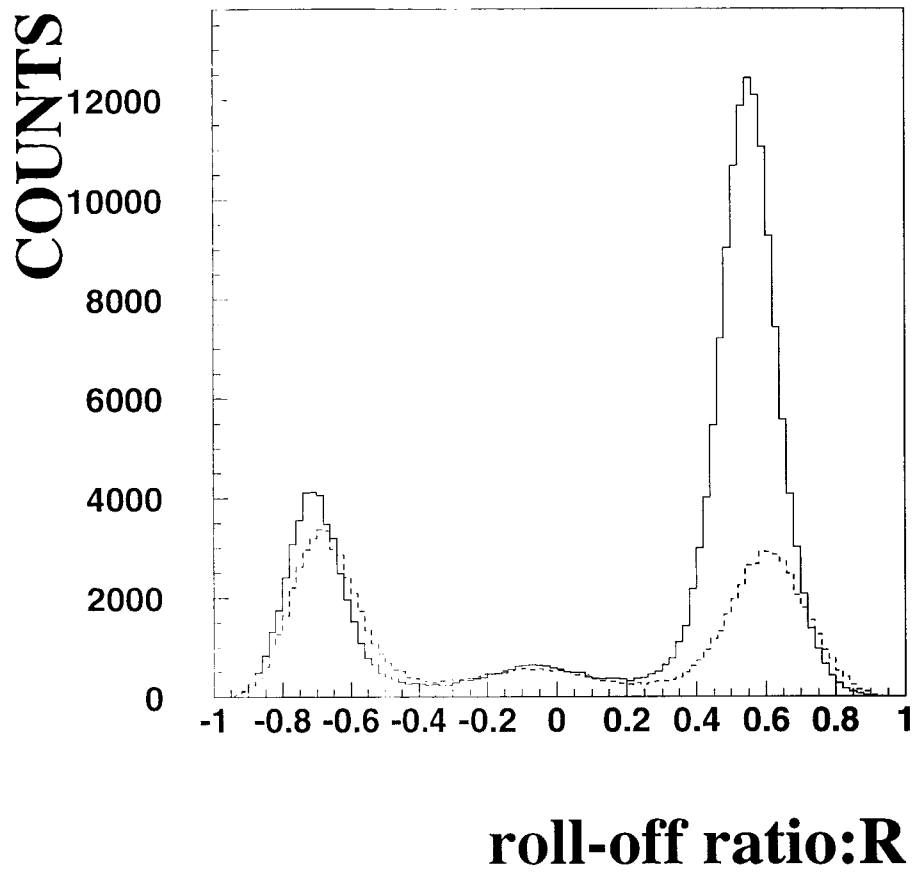
Fig. 6-7 Roll-off spectrum of the module #9 of CaF$_2$, which was obtained after the selection of (ii). This is compared with dashed line, which is roll-off spectrum of the module #14 of CaF$_2$.
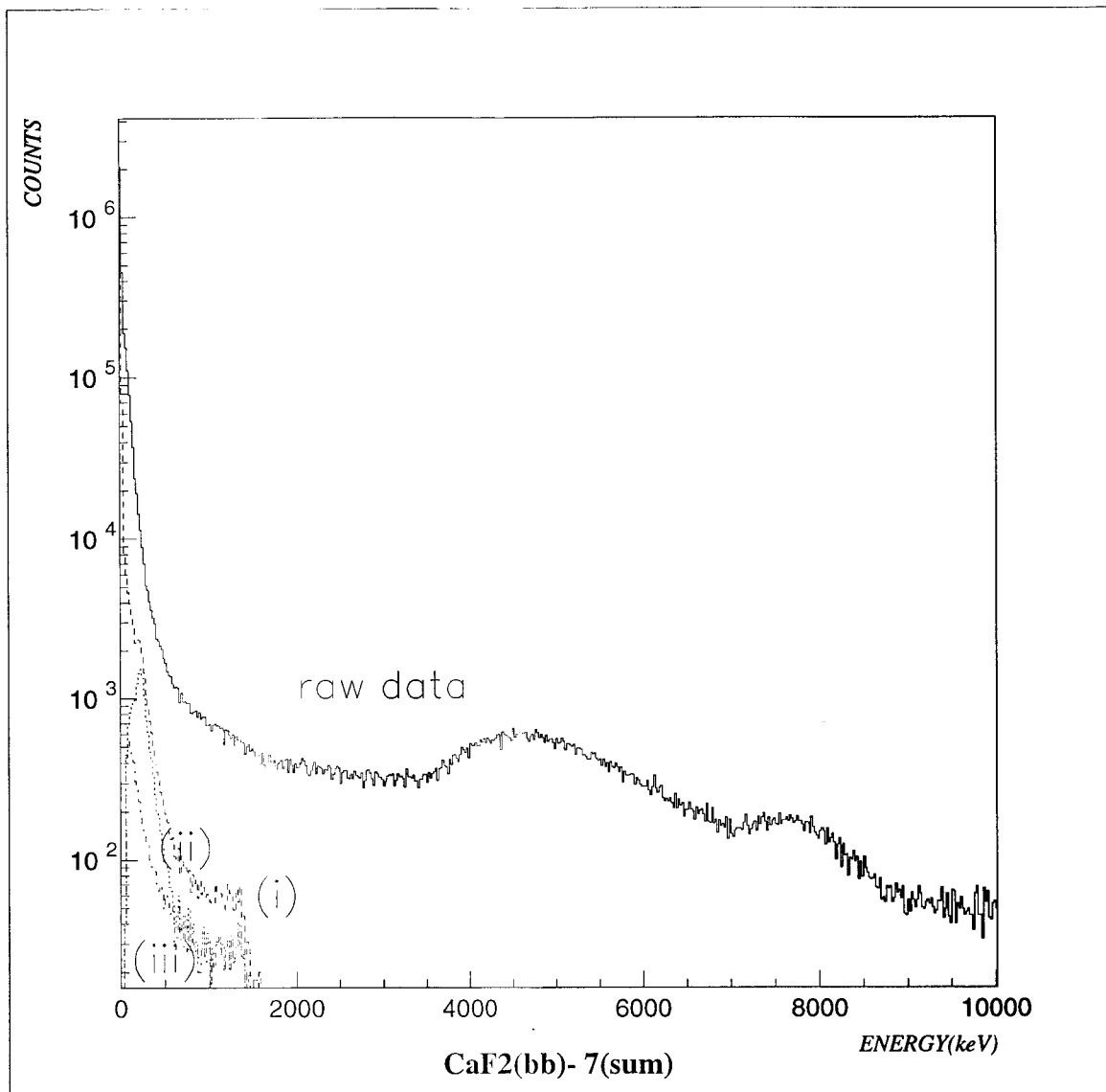
Fig. 6-8 High energy spectrum of the module #7 CaF_2 detector obtained for the study of $\beta\beta$ decays of ^{48}Ca. (raw data) in the full shieldings and N_2 gas circulation, measured for 1.6 days(RUN015-001); the raw energy spectrum, (i) in anti-coincidence with 40 CsI(Tl) detectors, (ii) in anticoincidence with the 40 CsI and 24 CaF_2 detectors, (iii) in anticoincidence with the 40 CsI, 24 CaF_2 detectors, and the light guides of pure CaF_2 scintillators(roll-off cut).

2) Passive shields

All RUNs including the all 25-CaF$_2$ RUNs are listed in Table 6-2, 6-3, 6-4, 6-5.

The effect of the passive shieldings on each process constructing the complete shieldings of ELEGANT VI was shown in Fig. 6-9, 6-10, 6-11, 6-12. The reduction rate of background is quite delicate especially after mounting the Cd sheet. Then the numbers of the residual events summing all energy region of dark matter after the active-veto (iii) at each passive shieldings are given in Table 6-6.

Table 6-6 The numbers of the residual events summing all energy region of dark matter after the active-veto (iii) at each passive shieldings.
number; Counts(CsI&CaF2 veto& roll-off cut)/hour
Energy; DM full range sum($\sim$ 300-500keV)
RUN015-005 is the complete shielding RUN except no LiH-paraffin shield.

Module #	RUN15-8	15-7	11-6	11-7	13-8	14-4	15-5
Condition	no shiled	only Cu	+Pb,LiH	+Cd	+H$_2$O	+H$_3$BO$_3$	no LiH
color	black	black	red	green	blue	pink	sky-blue
live time(h)	10.2	9.90	11.7	12.7	13.7	24.9	29.6
7(10)	381±6.1	72.6±2.5	53.1±2.0	51.6±1.9	46.0±1.4	41.2±1.2	83.7±2.9
8(20)	441±6.6	79.7±2.6	56.1±2.1	55.7±2.0	44.2±1.3	44.6±1.2	77.3±2.8
9(12)	723±8.4	135±3.4	73.5±1.6	78.3±2.4	71.5±1.7	69.9±1.5	136±3.7
12(2)	548±7.3	104±3.0	57.5±2.1	59.3±2.1	55.3±1.5	53.9±1.3	99.3±3.2
13(9)	729±8.5	132±3.4	86.5±2.6	83.2±2.5	73.5±1.7	70.9±1.5	119±3.5
14(5)	686±8.2	128±3.3	74.0±2.4	75.6±2.3	64.6±1.6	65.8±1.5	122±3.5
17(14)	484±6.9	98.7±2.9	62.4±2.2	60.6±2.1	47.8±1.4	42.0±1.2	76.9±2.8
18(25)	837±9.1	161±3.7	91.2±2.7	91.0±2.6	87.1±1.9	81.8±1.7	137±3.7
19(15)	653±8.0	121±3.2	78.0±2.5	76.9±2.4	66.5±1.6	69.0±1.5	123±3.5
average	609±23	115±9.4	70.3±6.8	70.2±6.8	61.8±4.7	59.9±4.2	108±9.9
reduction ratio	(1/1)	1/5	1/9	1/9	1/10	1/10	1/6

The reduction ratio can be achieved to be about one order by using only the passive shield, and the paraffin loaded with LiH is especially effective about an factor$\sim$2. This fact suggest that the conventional passive shieldings such as lead and copper, used for photon attenuation, acts as a strong neutron source, with the neutrons being produced primarily by cosmic ray muon interactions within the lead. Stanford group is also suggested these facts [80]. This was confirmed by the 'background search RUN' which was triggered by 40 CsI detectors and is described in detail in Chapter 7.2.2. And the moderator is a mandatory for slowing down to thermal neutrons. This is expected from the calculation of Fig.2-10 that the

these neutron shield is not effective until the thermal neutrons. **Then the further improvement** of water shieldings is planning in the near future.
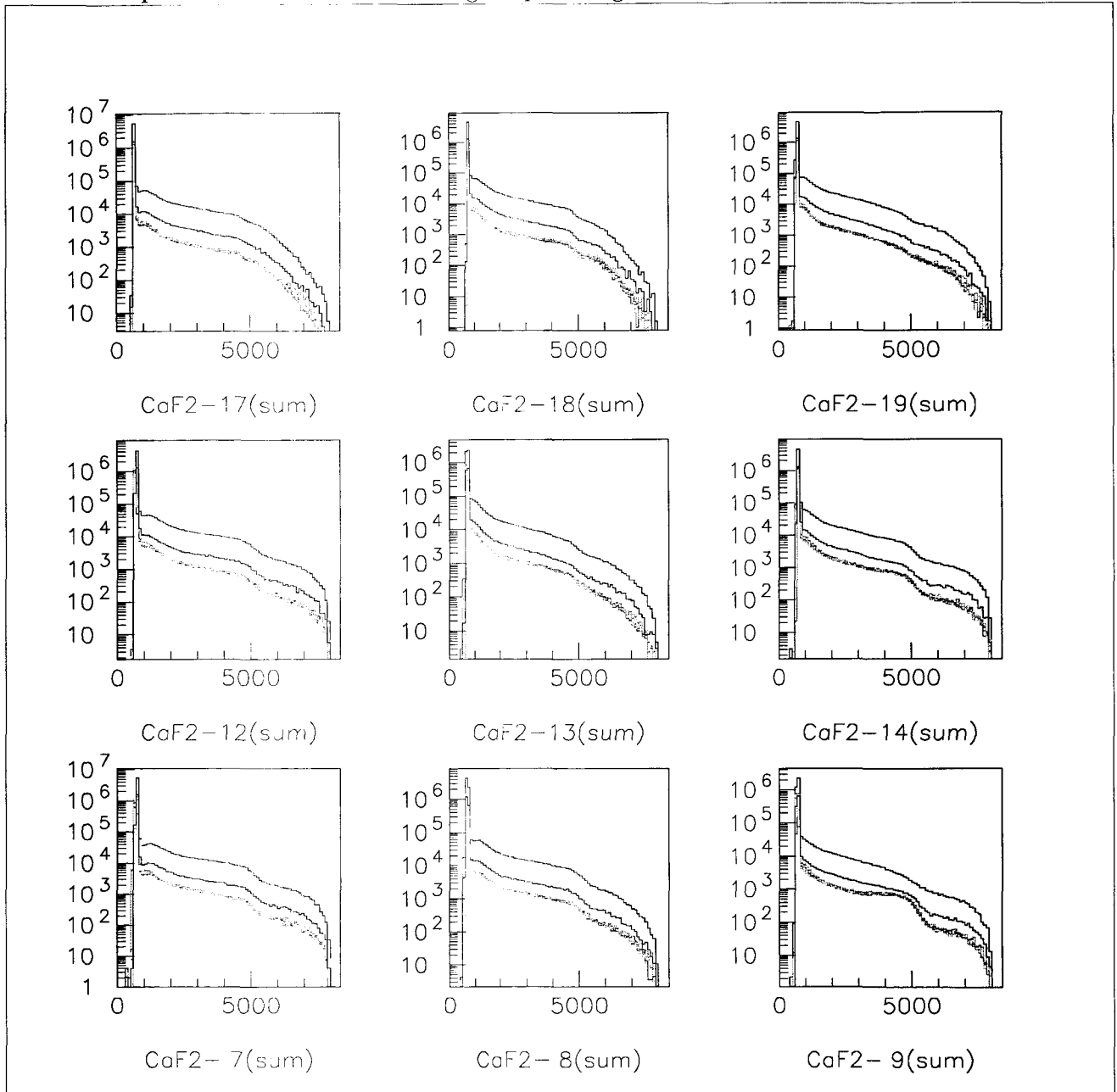
Fig. 6-9 Raw energy spectra of the central 9 CaF_2 detectors obtained at sea-level, Osaka. Black; no shield, Black; only Cu, Red; +Pb, Green; +Cd, Blue; +H_2O, Yellow; +H_2 bottom, Pink: +H_3BO_3, Sky-blue; No-LiH(shiled on). The horizontal axis is channel and the vertical axis is counts/100ch.
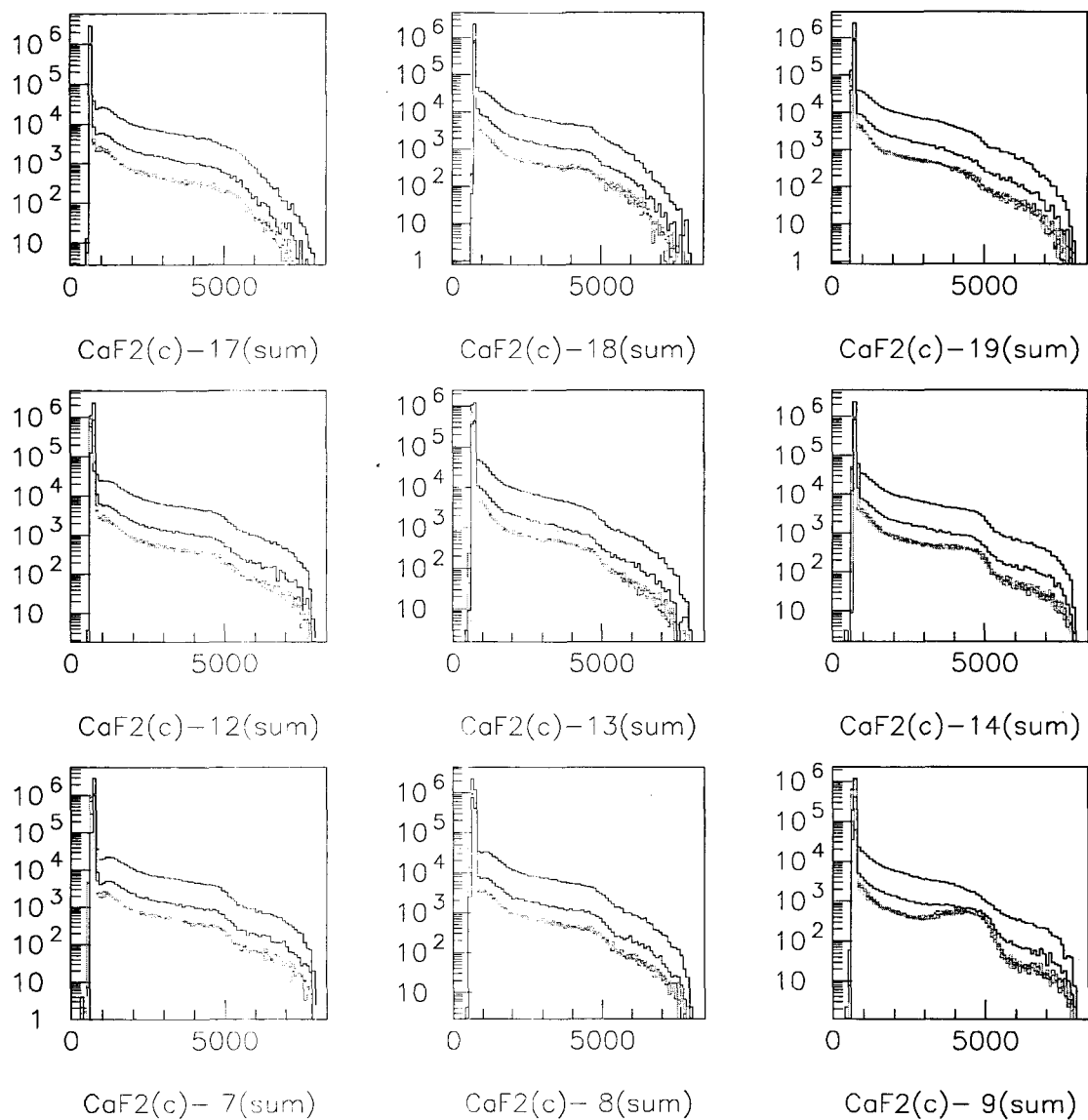
Fig. 6-10 Energy spectra of the central 9 CaF$_2$ detectors obtained at sea-level, Osaka, after the selection of (i) in anti-coincidence with 40 CsI(Tl) detectors. Black; no shield, Black; only Cu, Red; +Pb, Green; +Cd, Blue; +H$_2$O, Yellow; +H$_2$ bottom, Pink; +H$_3$BO$_3$, Sky-blue; No-LiH(shiled on). The horizontal axis is channel and the vertical axis is counts/100ch.
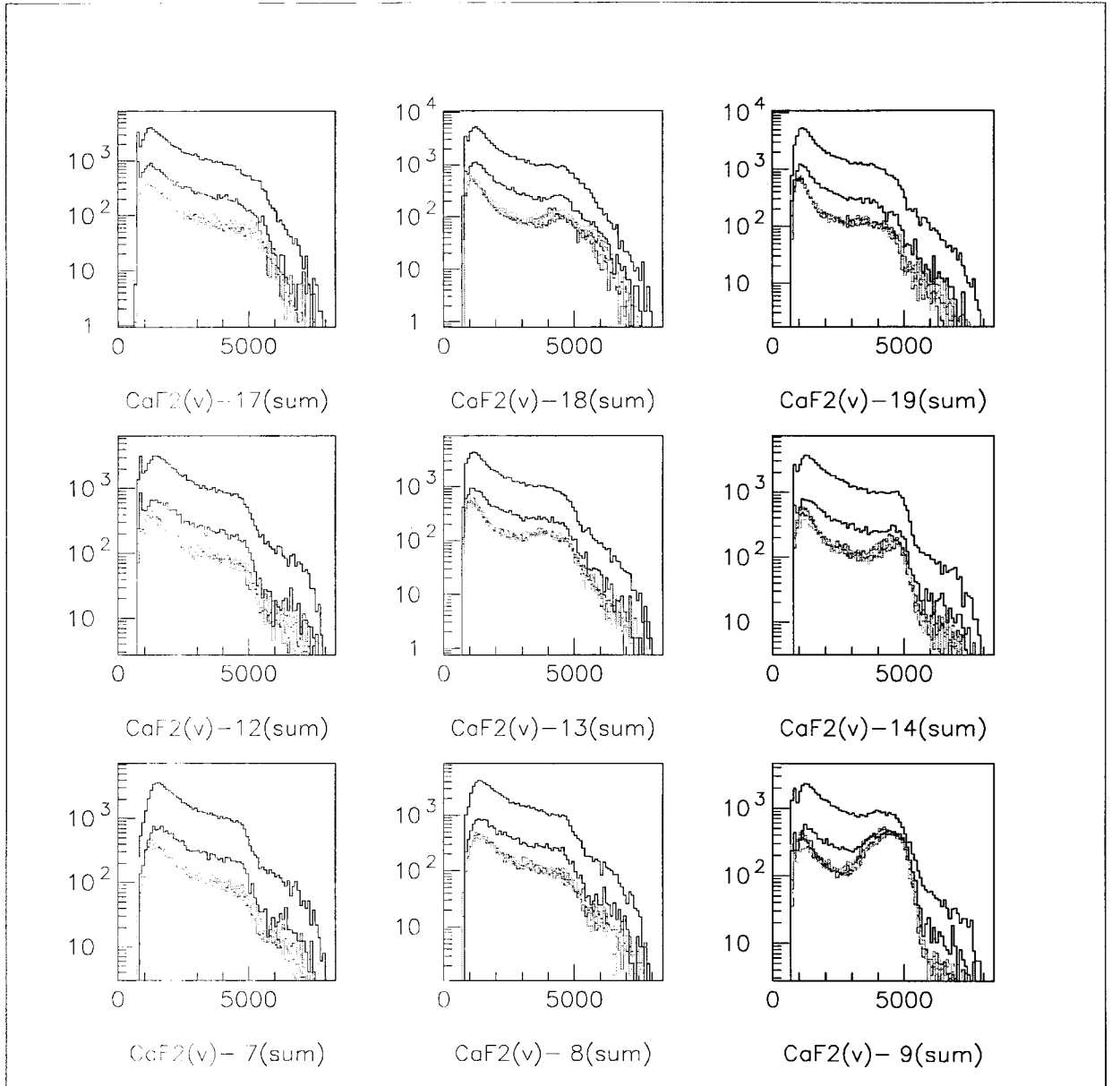
Fig. 6-11 Energy spectra of the central 9 CaF_2 detectors obtained at sea-level, Osaka, after the selection of (ii) in anticoincidence with the 40 CsI and 24 CaF_2 detectors, Black; no shield, Black; only Cu, Red; +Pb, Green; +Cd, Blue; +H_2O, Yellow; +H_2 bottom, Pink; +H_3BO_3, Sky-blue; No-LiH(shiled on). The horizontal axis is channel and the vertical axis is counts/100ch.

98
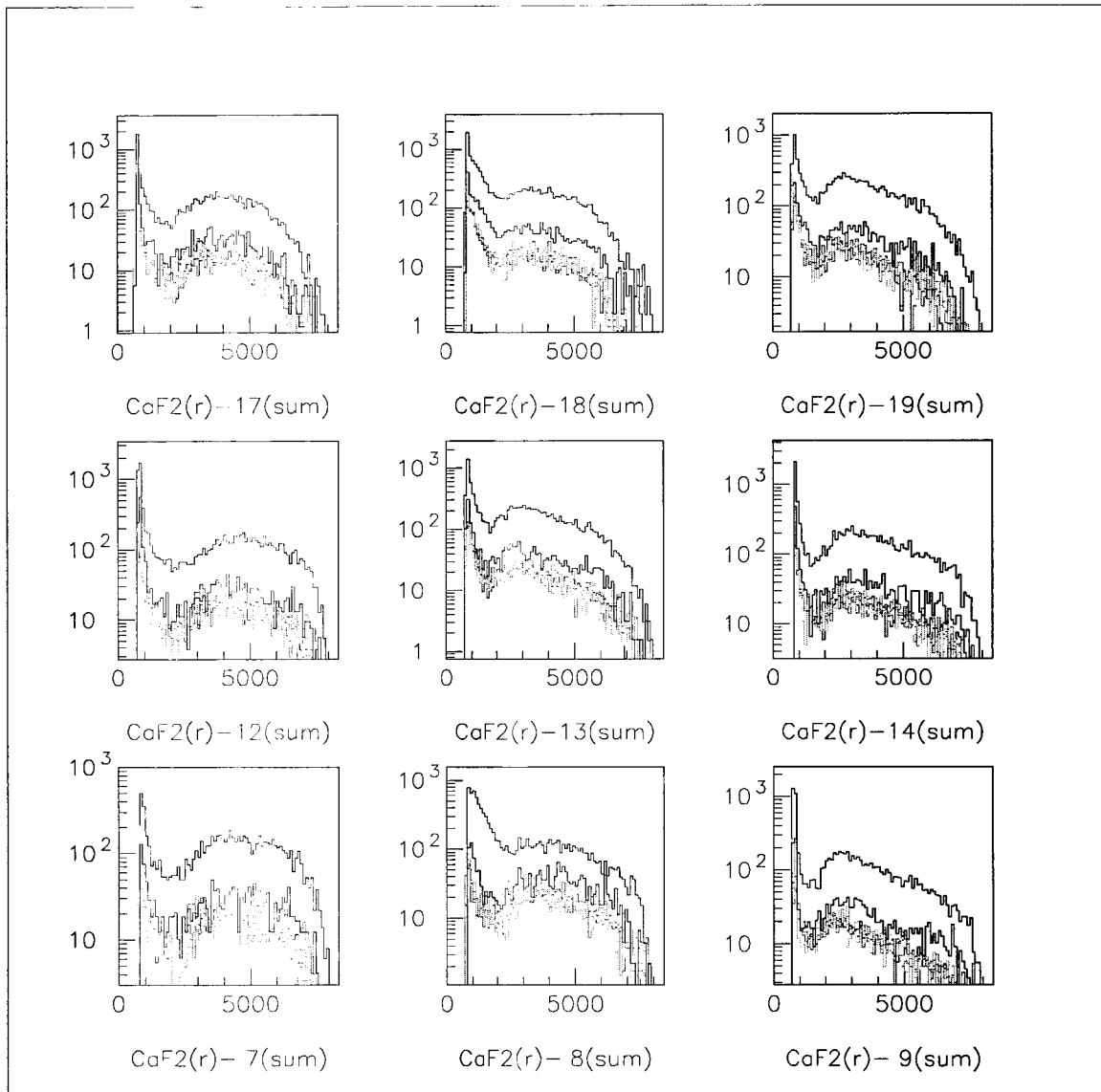
Fig. 6-12 Energy spectra of the central 9 CaF_2 detectors obtained at sea-level, Osaka, after the selection of (iii) in anticoincidence with the 40 CsI, 24 CaF_2 detectors, and the light guides of pure CaF_2 scintillators(roll-off cut). Black; no shield, Black; only Cu, Red; +Pb, Green; +Cd, Blue; +H_2O, Yellow; +H_2 bottom, Pink; +H_3BO_3, Sky-blue; No-LiH(shiled on). The horizontal axis is channel and the vertical axis is counts/100ch.

99

6.2.4 Limits on spin coupled cold dark matter

Based on the results of background reduction which was described in the previous section, the RUN-014 series;(b) was selected to analyze the recoil events of dark matters. Followings are the sum data of RUN014-004~-011.

RUN014-004~-011 ;

Total trigger rate : 84 counts per sec

Trigger rate of central 9 CaF_2 : 65cps (~7cps/1module)

Trigger rate of outer layer of 16 CaF_2 : 19cps (~1cps/1module)

Trigger rate of 40 CsI : 796cps (~20cps/1module)

Trigger rate of 2nd(delayed α) : 10cps (2nd/1st=10/84=12%)

Number of the acquired events : 33956389

Live time : 703390 seconds (~8.14 days)

Dead time : 39%

It is noted here that in these trigger rate of CaF_2, the 10Hz of the LED is included as usual. Since the signals of 4 LEDs are divided into 25 modules of CaF_2, the actual rate of the LED is 10/4=2.5 counts per second. N_2 gas is introduced with an average input-flow of 203 cc/min. Those are summarized in the Table 6-2, 6-3, 6-4 and 6-5.

The hitpattern and multiplicity of 25 CaF_2 and 40 CsI detectors for RUN014-004~-011 are shown in Fig 6-13 and 6-14, respectively.

100
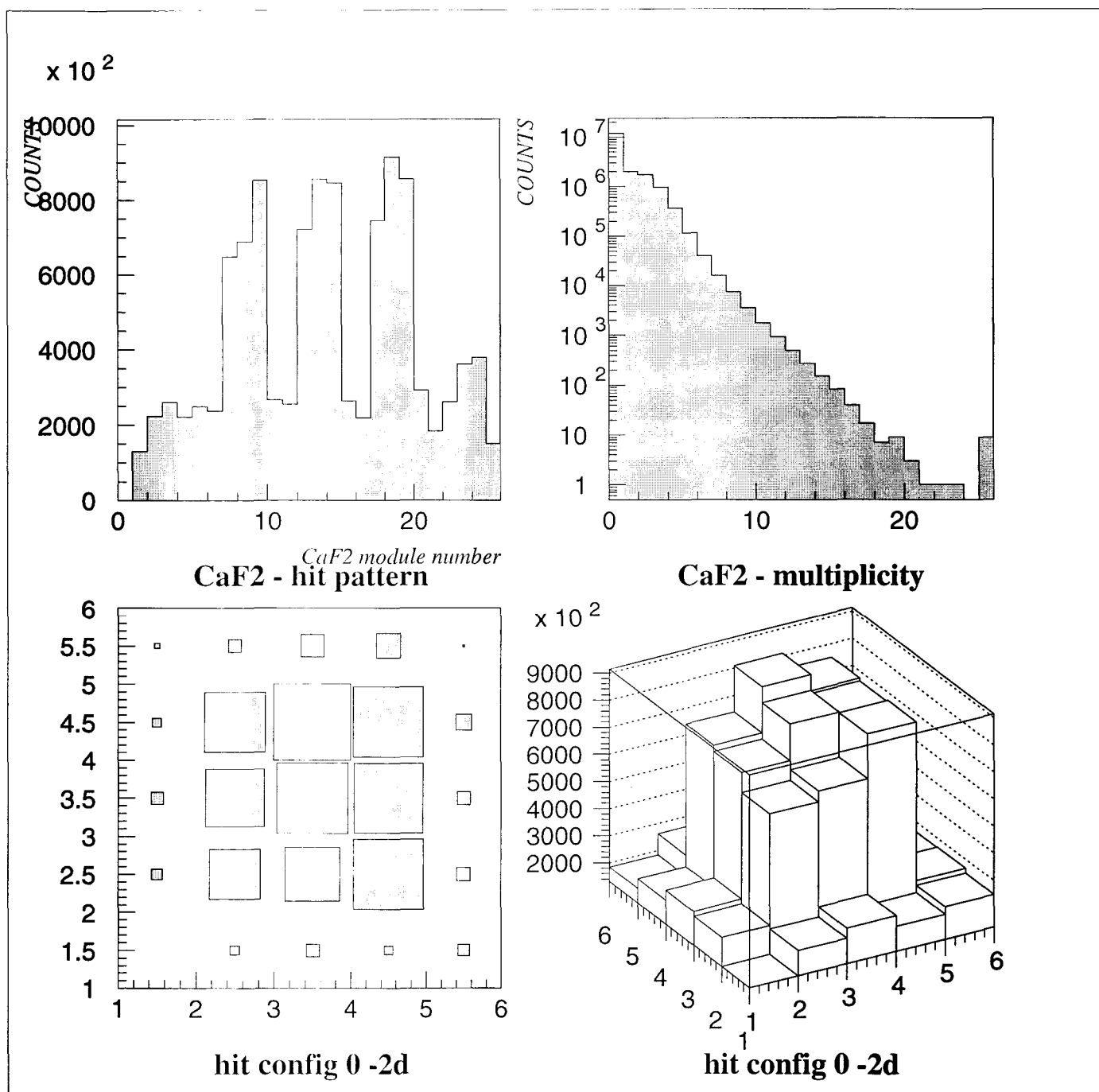
Fig. 6-13 The hitpattern and multiplicity of 25 CaF_2 for RUN014-004~-011. The **lower-left** figure is the side view of ELEGANT VI, which corresponds to the Fig. 6-5.

x 10 ^{2}

COUNTS

5000

4000

3000

2000

1000

0

0   10   20   30   40

CsI module number

CsI - hit pattern

COUNTS

10 ^{7}

10 ^{6}

10 ^{5}

10 ^{4}

10 ^{3}

10 ^{2}

10

0   10   20   30   40

CsI - multiplicity

7

6

5

4

3

2

1

2   4   6

hit config 0 -2d

x 10 ^{2}

8000
7000
6000
5000
4000
3000
2000
1000
0

6   4   2   2   4   6

hit config 0 -2d
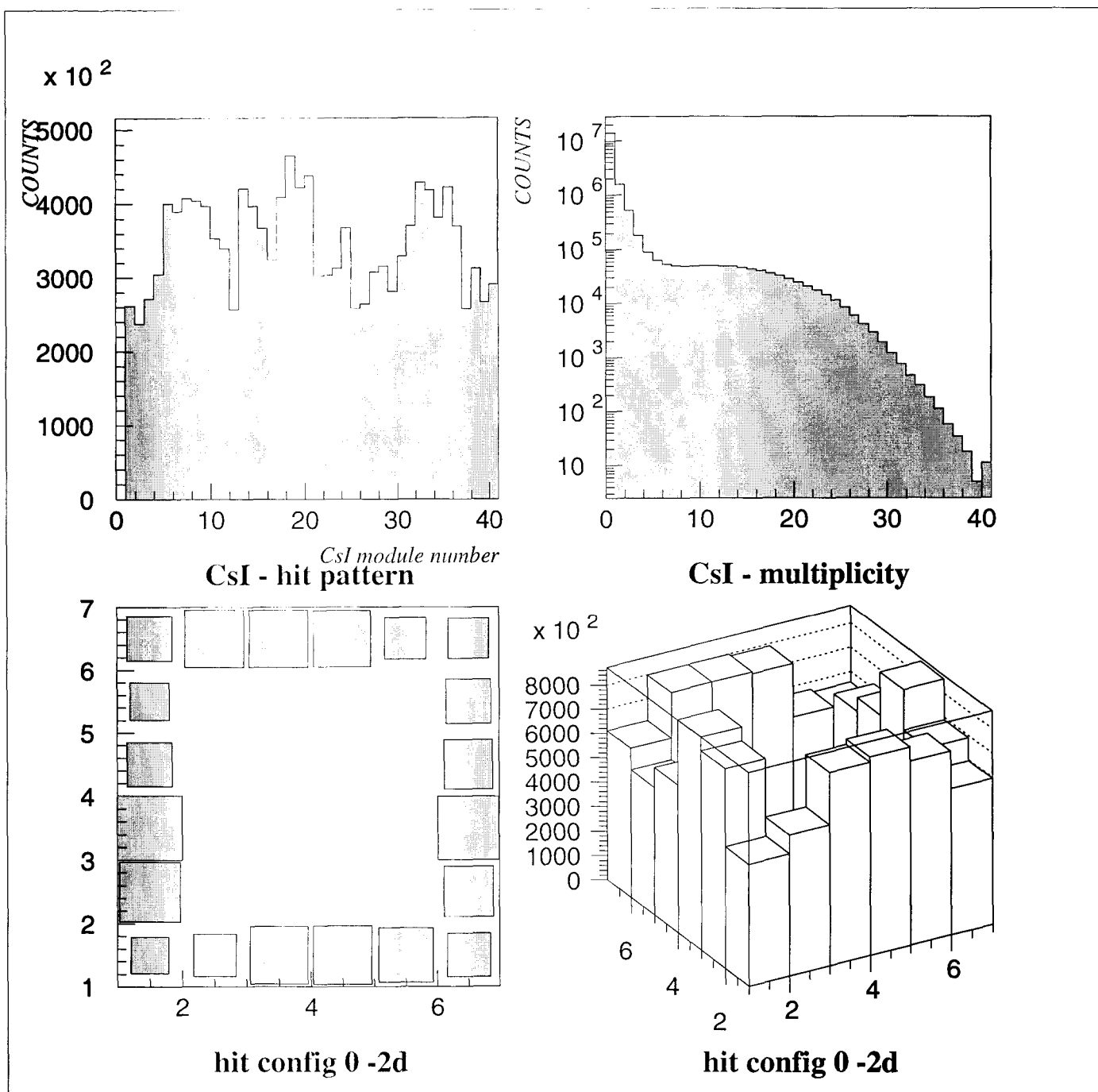
Fig. 6-14 The hitpattern and multiplicity of 40 CsI for RUN014-004∼-011. The lower-left figure is the side view of ELEGANT VI, which corresponds to the Fig. 6-5.

102

Figure 6-12 shows that it is not favorable to sum the energy spectrum of all the 9 CaF$_2$ modules, unfortunately. Evaluating the limit on the maximum halo density of the DM's, the energy spectrum of module #7 was selected and the observed spectrum, which was shown in Fig.6-15, was analyzed in terms of the recoil spectrum of ^{19}F with the conversion f-factor. Excluded region by the present measurement is shown in Fig. 6-16.

In the calculation of the axial vector coupling(g_A) constant, we have used single particle shell model (see Table 1-7) and the most recent analysis of the EMC result for the calculation of g_A [39] (see Table 1-8).
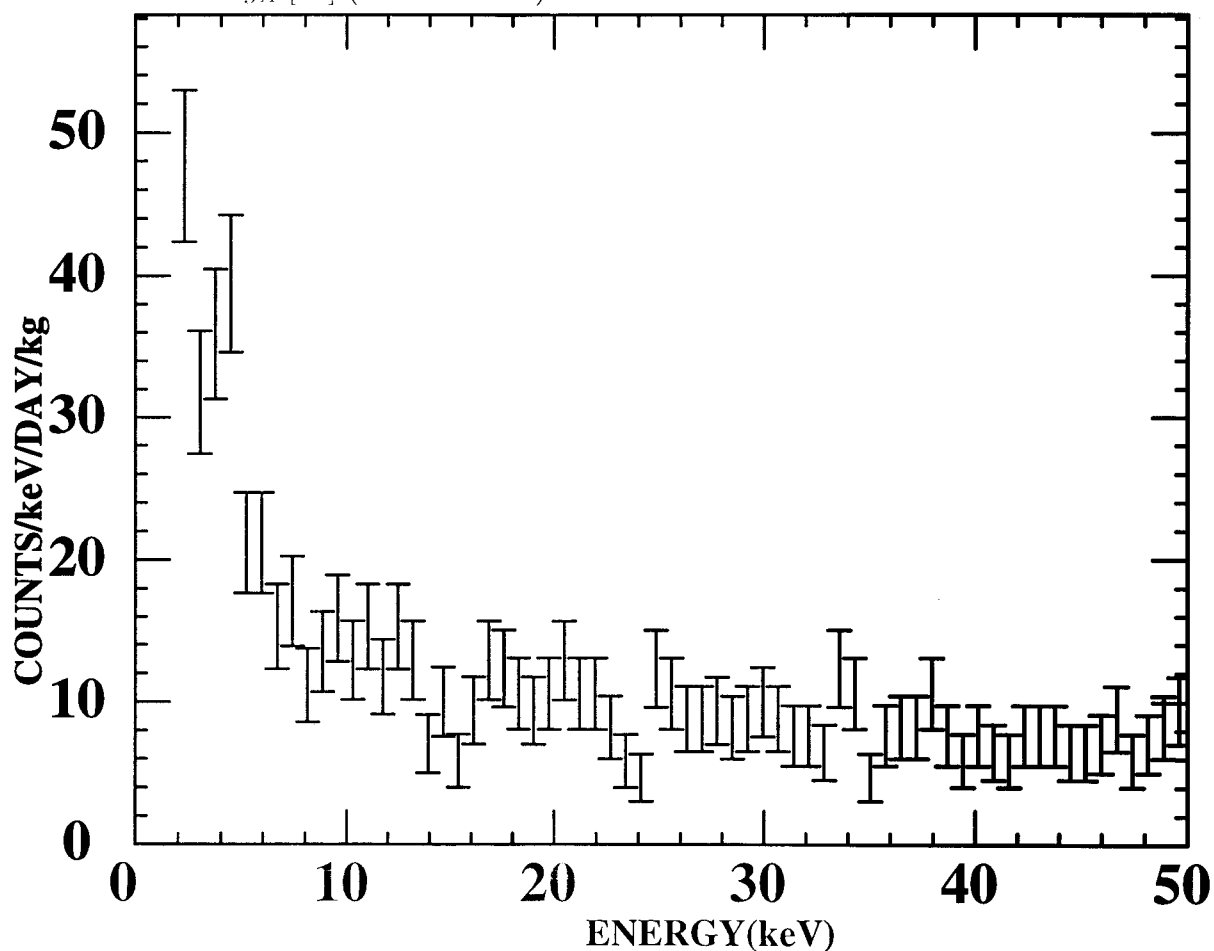
Fig. 6-15 A spectrum of the CaF$_2$ detector (module number#7) taken at the laboratory of Osaka Univ.(sea level). The quoted errors are statistical (1σ).
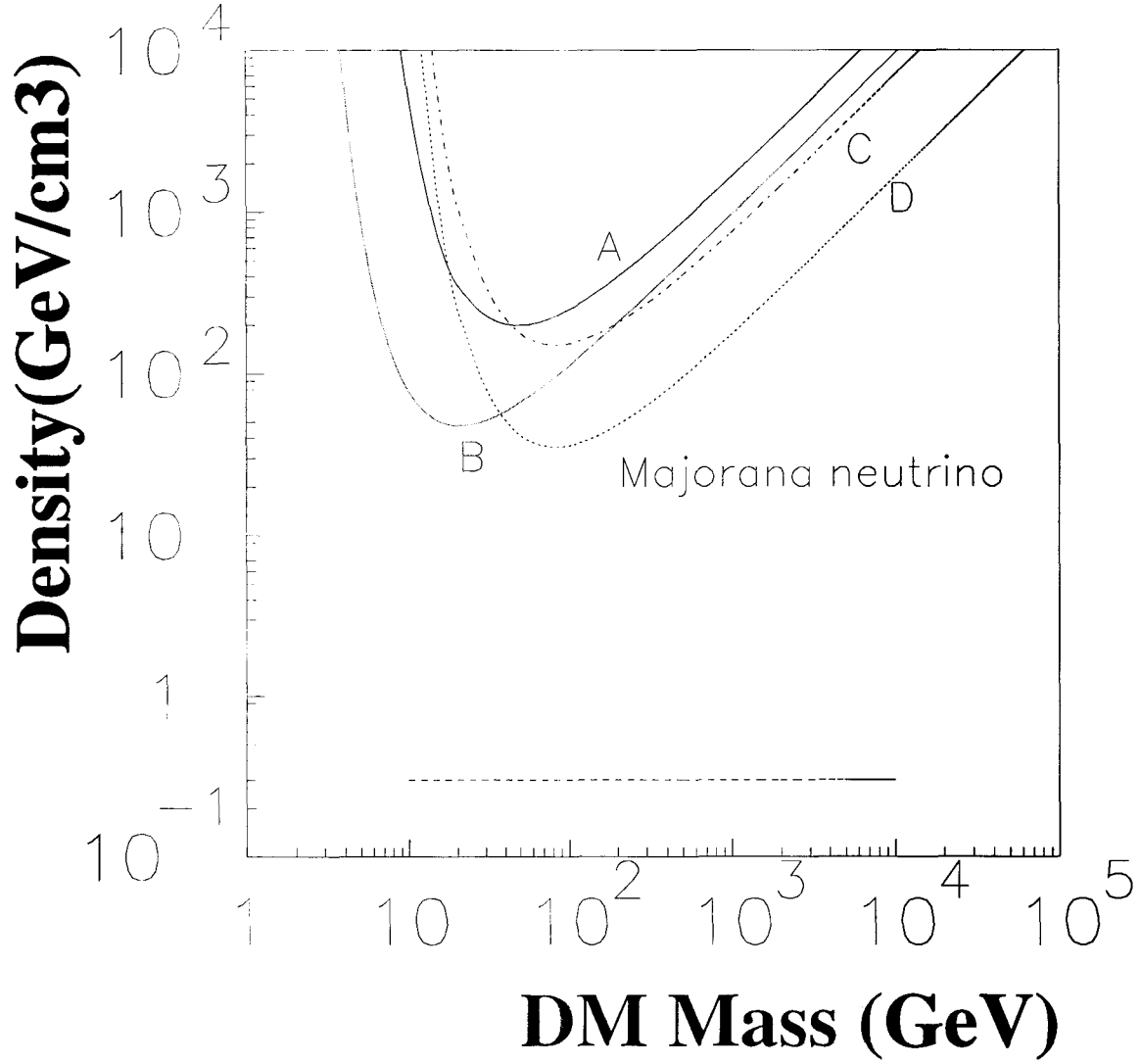
Fig. 6-16 The observed counting rate is converted to the **halo density of Majorana neutrino** (ν_M). Upper region from the lines are excluded. **(A) shows the result of test-RUN** using only 8 CaF_2 modules [65]. (B) shows the present result of **ELEGANT VI at Osaka**. (C) shows the result of BPRS Collaboration at Gran Sasso [44]. **(D) shows the result of DAMA** Collaboration at Gran Sasso [81]. The dashed line indicates the critical density of $0.3GeV/cm^3$.
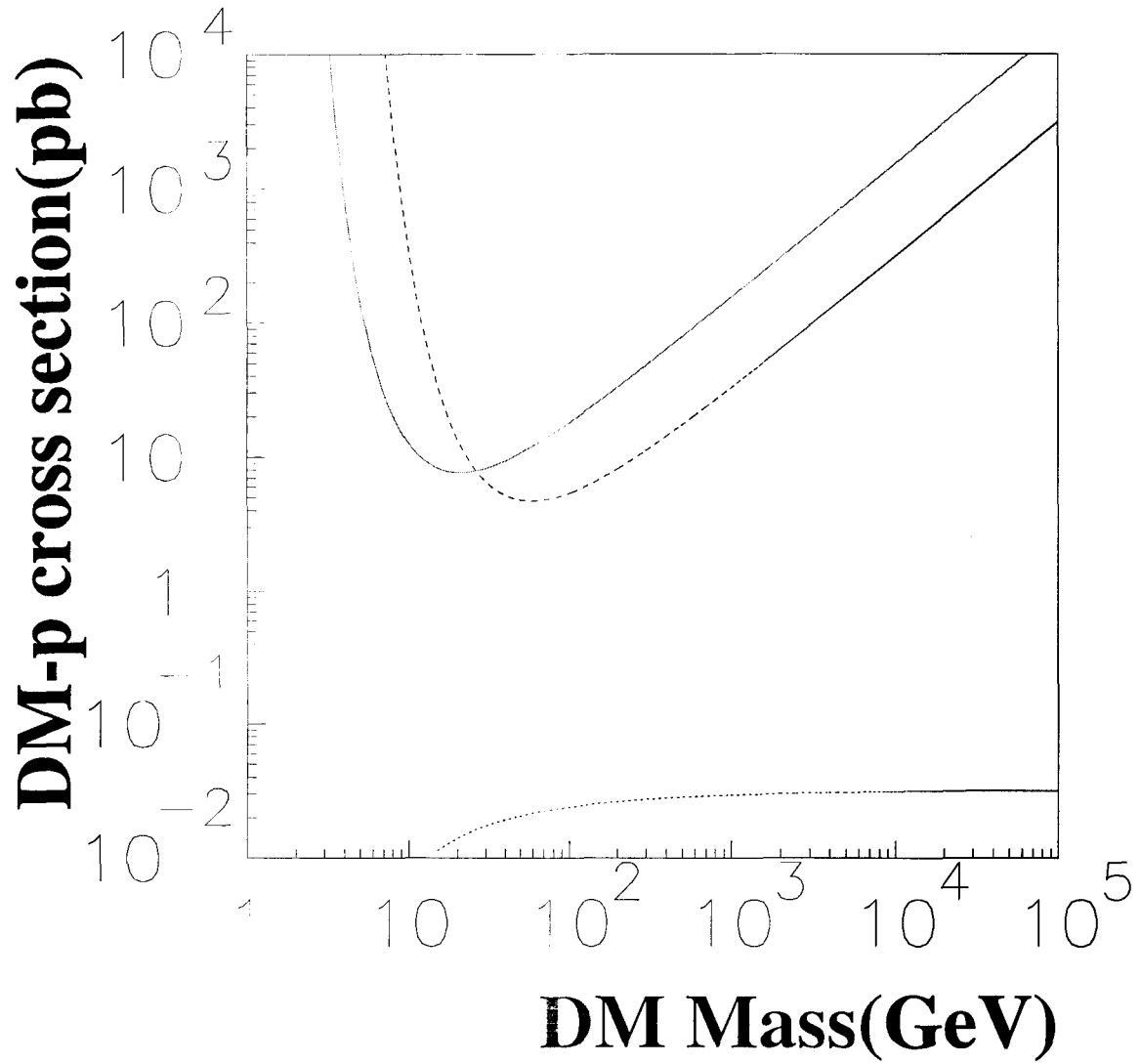
Fig. 6-17 Exclusion plot in the cross section versus the mass plane. Upper region from the lines are excluded. Solid line shows the present result of ELEGANT VI at Osaka. Dashed line shows the result of DAMA Collaboration at Gran Sasso [81]. Dotted line shows the predicted cross section for Majorana neutrino.

105

In the case of neutralino the limit depends on the mixing of photino, Higgsino, and Zino. Hence the exclusion plot was shown in the case of Majorana neutrino, which has an almost comparable and unambiguous cross section (see Chapter 1-3(2) and Table 1-6). Recently DAMA Collaboration presented improved limits on WIMP-^{19}F elastic scattering by using a low radioactive $CaF_2(Eu)$ scintillator at Gran Sasso National Laboratory (LNGS) [81]. However, the present new result already has similar precision as the improved limit of DAMA Collaboration.

It is noted that the present result is obtained by the subset of ELEGANT VI at the sea level. We expect much better results when the detector is operational at the underground laboratory. The prospects on the operation at the underground is described in Chapter 7.3.

Table 6-2 Summary of the condition of RUN001~006 (all 25-CaF$_2$ RUN).

RUN #	Date	Condition	time(s)	record
001-001	3/20-3/21	front&back no shield		2482499
001-002	3/21-3/22	Pb&Cu&LiH	47714.212	2125736
001-003	3/22-3/23	Cd&24-H2O dis=10mVall	44337.867	1961170
001-004	3/23-3/24	dead include tape dump	58316.74	1959525
001-006	3/25-3/26	dis=50/30,#21/24up	57017.606	1820956
001-007	4/1-4/2	no-N2,dis=60,#25up	72493.739	2574163
001-008	4/3-4/4	no-H2O tanno-N2	57548.74	2053435
002-007	4/9-4/10	no-Cd	47110.196	1847448
002-010	4/11-4/12	power down stop(no-Pb)		
003-002	4/14-4/15	no-Pb	55697.132	
004-001	4/16-4/17	no-Cu,monitor shield new	40700.199	1969721
005-001	4/17-4/18	no-LiH except under	36494.619	
006-001	4/22-4/23	only no LiH(Pb&Cu set)	33537.003	

RUN #	CaF2 trig	CsI trig	2nd trig	Temp.(°C)	N2(ml/min)	LED(Hz)
001-001				21.7/21.1	388(36)	1
001-002	7074442	9069041	2124107	21.8/21.1	380(48)	1
001-003	?18337190	?85712798	1959891	21.4/21.0	420(37)	1
001-004	8853300	519697287	1289817	21.5/21.0	430(53)	1
001-006	8280983	521303011	1188440	21.8/21.0	460(63)	1
001-007	11860517	?93705045	1771013	22.3/21.1		1
001-008	10154564	?64426573	1489790	22.7/21.3		1
002-007	9926465	?84304826	1434826	23.4/21.8		1
002-010				23.2/21.8		1
003-002	18825881	?10338334	21297713		1	
004-001	38010176	504529284	1928659	24.2/22.2		10
005-001	31882229	?29590878	1717100	24.1/22.0		10
006-001	?06816132	25868661	1451874	24.0/25.5		10

Table 6-3 Summary of the condition of RUN011~013;selected 9-CaF$_2$ RUN (a).

011-001	6/5-6/6	no-front/back Pb.Cu,N2,LiH	58648.43	1988185
011-002	6/6-6/7	LiH on(except door side)	67092.88	2220612
011-003	6/8-6/9	N2-in	59740.06	1990813
011-004	6/9-6/10	front&back Cu	74509.26	2101347
011-006	6/10-6/11	Cu&Pb complete	78309.04	2165833
011-007	6/11-6/12	Cd on	84698.41	2352551
011-008	6/12-6/14	24-H2O on	160359.45	4436882
011-009	6/15-6/16	same as 11-8	148631.61	4147740
012-001	6/18-6/20	noise down	153155.29	4246815
012-003	6/22-6/23	dis(L/R;out16=400up)	158064.82	
012-005	6/25-6/27	dis=200,I/O Reg=400,10ms	175665.17	5064220
012-006	6/27-6/29	44(29.15)H2O up	148138.95	4239190
012-007	7/1-7/3	conversion 100K(clock)	148630.62	4222430
012-008	7/3-7/5		171445.66	5087426
013-002	7/8-7/10		139137.74	4238218
013-003	7/10-7/12		160492.38	4880458
013-004	7/12-7/14	138479.72	4164361	
013-005	7/14-7/16		170486.15	5026336
013-006	7/16-7/18		168057.62	
013-007	7/20-7/22	61(31. 30)H2O up	179271.64	5070484
013-008	7/22-7/24	bottom(6+4)H2O up	147965.88	4233962
013-009	7/25-7/27	power all down;reboot		

RUN #	CaF2 trig	CsI trig	2nd trig	Temp.(°C)	N2(ml/min)	LED(Hz)
011-001	6862131	30763604	168184	24.0/21.0		10
011-002	7156874	158431365	184307	23.5/21.0		10
011-003	6748021	137963234	163128	23.5/20.5	440(32)	10
011-004	6204348	121997033	192551	23.8/21.2	438(25)	10
011-006	6185639	114063670	206067	25.8/23.0	438(13)	10
011-007	6756268	123852217	220265	25.2/22.2	430(26)	10
011-008	12588783	232735714	415911	24.9/21.9	438(25)	10
011-009	11824498	217336149	387602	25.1/21.8	330(0)	10
012-001	11831554	222058547	390173	25.2/23.2	350(0)	10
012-003	12970851	228244839	417868	25.2/22.2	195	10
012-005	14704444	255613701	1810678	25.2/21.5	210	10
012-006	13161737	215461907	1736838	27.0/24.0	145	10
012-007	12104878	218029231	1435911	26.0/22.3	205	10
012-008	14638015	251104790	1857088	26.2/24.8	200	10
013-002	12157350	204330841	1606852	26.9/24.0	200	10
013-003	13844337	236089325	1816119	26.3/24.0	196	10
013-004	11838438	203834301	1532992	26.2/24.2	205	10
013-005	14208328	252180549	1776013	25.2/22.2	210	10
013-006		250250334	1671649	25.2/22.4	210	10
013-007	14414314	265804214	1703493	25.2/24.0	200	10
013-008	12021538	219971259	1448098	25.8/23.5	205	10

108

Table 6-4 Summary of the condition of RUN014;selected 9-CaF$_2$ RUN (b).

014-001	7/29-7/31	CsI CoinReg– >3		140526.57	4242048	
014-003	8/2-8/3			169755.04	5167764	
014-004	8/6-8/8	H3BO3(4%)+H2O(1260liter)		171512.31	4832189	
014-006	8/10-8/12			157930.54	4722312	
014-007	8/14-8/16	CsI(dis;-20– >7mV)		167830.35	4928698	
014-008	8/19-8/20	CsI(dis;-20mV;reset)		138632.13	4072216	
014-009	8/20-8/22			165247.4	4879723	
014-010	8/22-8/24			162073.09	4809053	
014-011	8/28-9/2	disk(ejdb– >tora+9GB)17GB		473056.73	13794792	
RUN #	CaF2 trig	CsI trig	2nd trig	Temp.(°C)	N2(ml/min)	LED(Hz)
014-001	12064990	109299378	1516753	25.0/22.8	215	10
014-003	14832501	132960609	1897938	25.2/22.3	220	10
014-004	13876206	137223188	1615040	25.2/23.5	225	10
014-006	13703906	125344448	1720422	25.0/23.0	235	10
014-007	14175947	2027935619	1750849	25.5/22.5	150	10
014-008	11645524	109412543	1450720	25.0/23.5	200	10
014-009	13991554	131012324	1746448	25.3/24.0	200	10
014-010	13849115	129790419	1734164	25.1/23.8	200	10
014-011	39580889	379352699	4841915	25.2/22.2	210	10

Table 6-5 Summary of the condition of RUN015; selected 9-CaF$_2$ RUN (c).

015-001	9/3-9/6	2nd trig;25sum:dis=90mV	264874.56	7547395
015-002	9/9-9/10	rate up(116cps)TDC(peak?)	97713.49	3901023
015-003	9/10-9/12	2nd trig(reset-¿10ms)	140332.1	4637703
015-004	9/16-9/17	no LED	63242.49	1478494
015-005	9/17-9/18	no LiH(Pb,Cu,Cd,H3BO3 on)	88494.66	2393556
015-007	9/19-9/20	only Cu	68174.84	2143544
015-008	9/20-9/22	no shield(except bottom)	159573	7103883

RUN #	CaF2 trig	CsI trig	2nd trig	Temp.(°C)	N2(ml/min)	LED(Hz)
015-001	21691692	213056466	82568	24.9/23.9	230	10
015-002	14758181	70858702	68375	28.2/24.9	80	10
015-003	13393783	104447696	2035568	26.9/24.1	88	10
015-004	4366180	49117470	23435	25.2/22.9	100	0
015-005	7026942	65701707	24473	25.5/22.9	105	10
015-007	6956983	104166497	27143	26.0/24.2	105	10
015-008	42276208	1462141932	177423	25.8/24.5	104	10

Chapter 7

PROSPECTS

7.1 Gain monitoring by LED

In an experiment which requires long and continuous running time with a large number of PMTs, performing frequent tests on the system's stability is essential. The LED of NLPB520(Nichia Chemical Industries Ltd.) and optical fibers calibration device enables daily (actually "second"ly) checking of the energy calibrations [63]. The daily energy variations are then corrected off-line by software. However, the scintillation intensity also changes with temperature as shown in Fig. 7-1. Then now we are developing the temperature monitoring system by thermocouple.
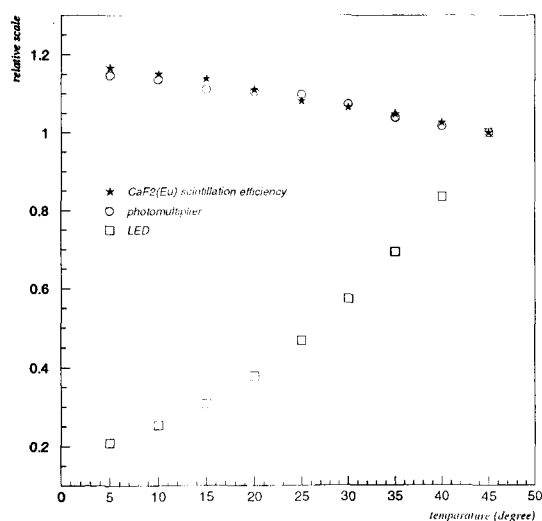
Fig. 7-1 The temperature dependence of the scintillation light output of CaF$_2$(Eu), PMT(H3178MOD) and LED(NLPB520).

At the present overground measurements, the pedestal and **gain shift of the detector
are** monitored by using **the LED,** the peaks of alpha ray around 1 **MeV and muon
minimum** ionization. The fluctuation of the gain shift is less than **10 %.**

7.2 Origin of the background

7.2.1 internal backgrounds

The high energy spectra, **which** was taken simultaneously **for the study of double beta
decays** of ^{48}Ca, exhibit structures around 1 MeV (see Fig. 7-2) **unexpected from gamma-
ray** interactions in the crystal. These spectra are obtained after **the selection of (i), (ii)
and** (iii) which was describe in Chapter 6.2.3. Among 25 spectra of $CaF_2(Eu)$, **module
number#24,** 21 and 5 are especially prominent. These modules **were positioned in the
outer** layer of all CaF_2 modules, because these modules were **high event rates in the all
25-CaF$_2$** RUN.
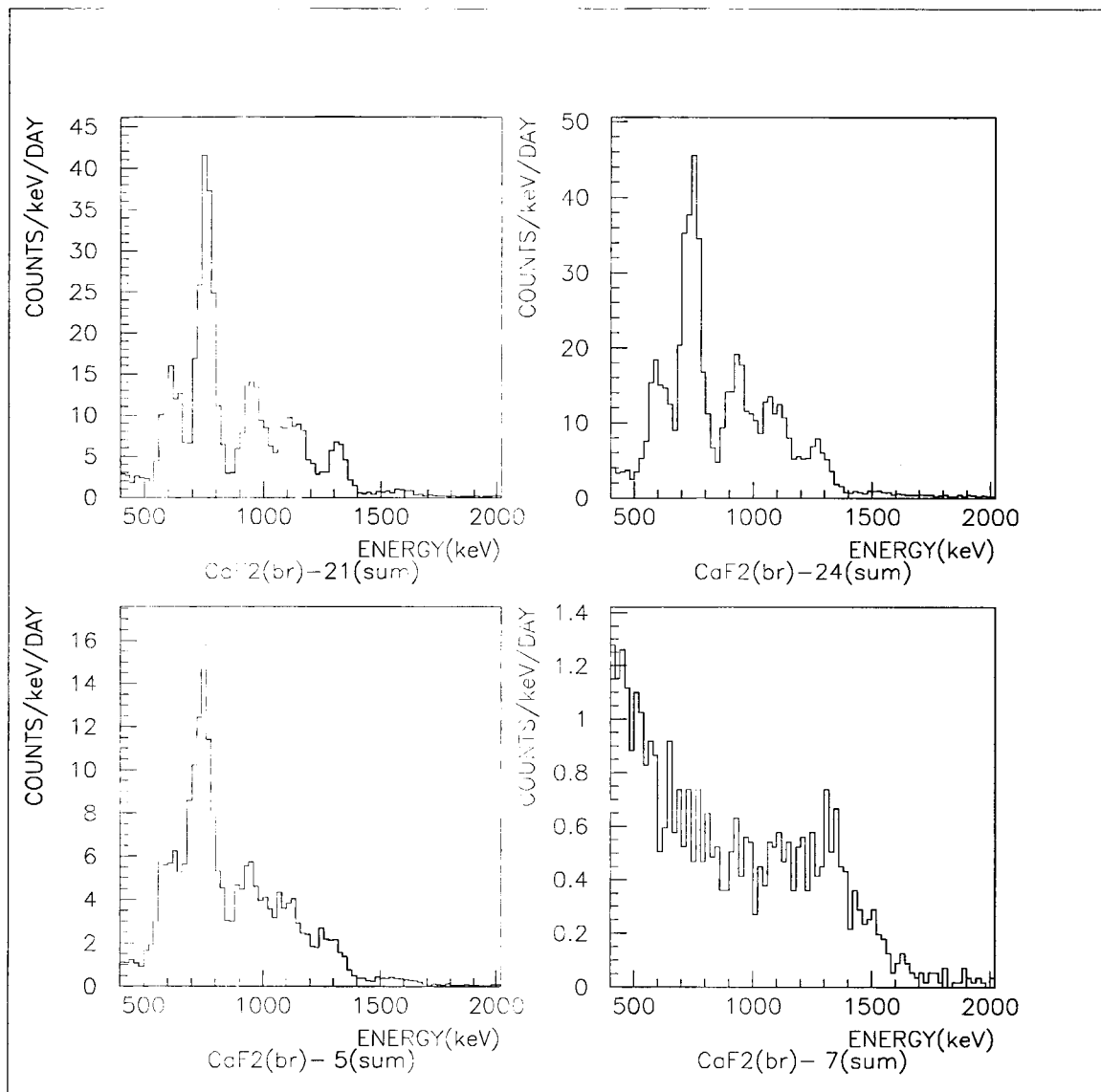
Fig. 7-2 High energy spectra of the module number#24, 21 and 5 in the RUN015-001 (the live time of 1.6 days) after the selection of (i), (ii) and (iii). These are compared with the module number#7.

Taking into account the scintillation efficiency for alpha's relative to electrons, of about 17% [82], the mean energy of these prominent peaks correspond to be around 5 MeV. Simulations with alpha sources confirm that these events are caused by alpha particles generated inside the crytal. Their origin is attributed to decays of ^{238}U and ^{232}Th and their daughters. The observed spectrum has been fitted with the hypothesis of a mixture of U and Th chains, with ^{226}Ra out of equilibrium. Result of the fit for

113

the module number#24, which is shown in Fig. 7-3, indicate that ^{226}Ra are strongly out of equilibrium ($\sim$25 times of U concentration) and that the alpha's are coming in different proportions from U ($\sim$8 ppb) and Th ($\sim$0.5 ppb) chains. On the assumption of equilibrium except for ^{226}Ra, equivalent concentrations for ^{238}U (U) and ^{232}Th (Th) are obtained. In this fit, eight parameters are used as follows,

P1 ; equivalent concentration for Th (ppb)

P2 ; equivalent concentration for U (ppb)

P3, P4 ; scintillation efficiency for alphas relative to electrons, The Birks law is used as the parametalization of $E = E_\alpha/(\text{P3-P4}\times E_\alpha)$

P5 ; correction of the resolution: $\Delta E(\text{FWHM})/E(\%) = \text{P5}\times a/E$, where a is obtained for each module by the γ-ray calibration.

P6, P7 ; a continuum component with exponential function of exp(P6+P7$\times$E) are included.

P8 ; out of equilibrium of ^{226}Ra, concentration of ^{226}Ra (ppb) is obtained by P2$\times$P8.

The dominent elements in both chains are ^{226}Ra (U) and ^{232}Th, ^{228}Th to ^{212}Po section (Th) (^{212}Po is accompanied with 2.25 MeV beta ray, then this peak are broadened. [83]).

114

χ^2/ndf 31.96	/	48
P1	8.165 $\pm$	1.200
P2	0.4505 $\pm$	0.4624
P3	9.207 $\pm$	0.6093E-01
P4	0.5481E-03 $\pm$	0.1109E-04
P5	0.3663 $\pm$	0.2481E-01
P6	1.886 $\pm$	0.5017
P7	-0.1438E-02 $\pm$	0.6107E-03
P8	25.06 $\pm$	28.42
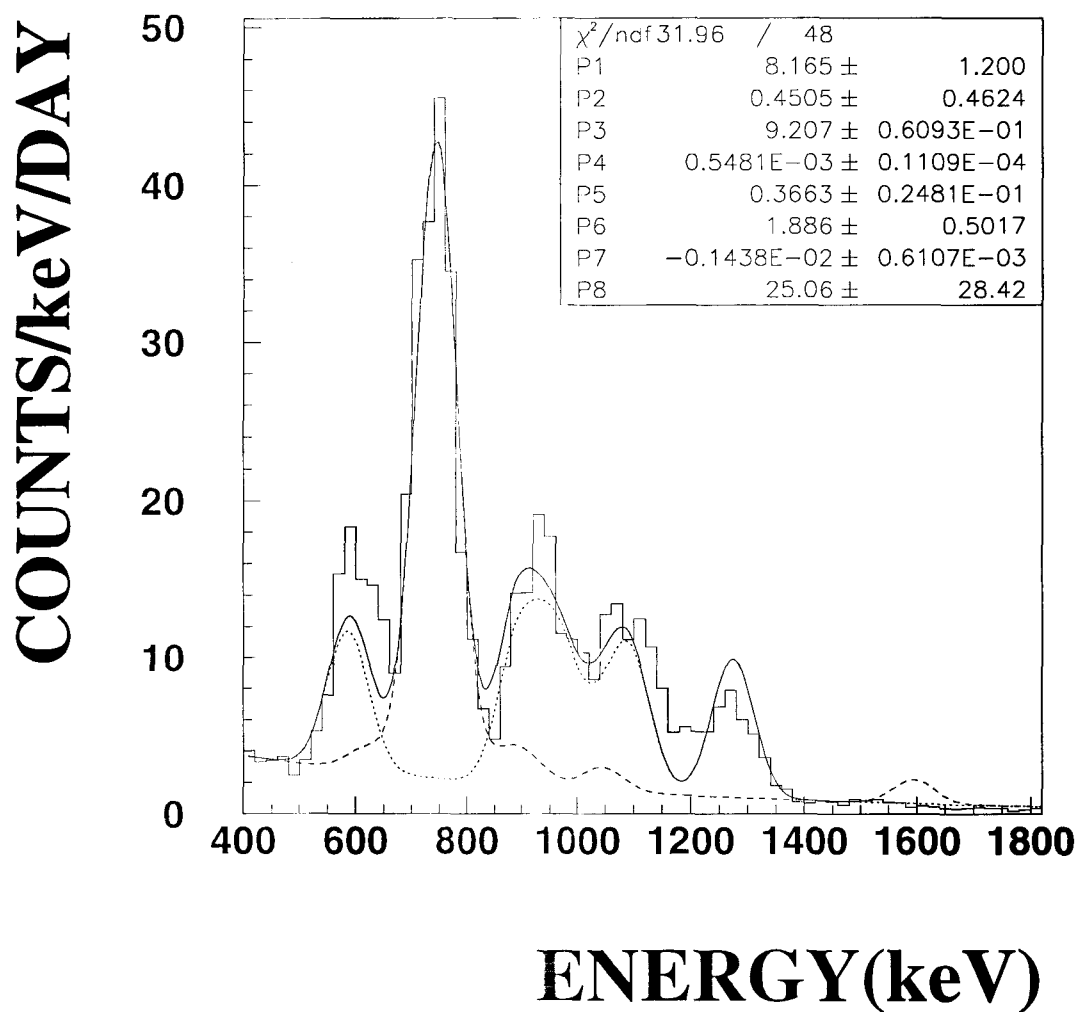
Fig. 7-3 Result of the fit for the module number#24. The solid line is the sum of U and Th. The dashed line is the proportion of U content. The dotted line is the proportion of Th content.

This result suggest that this $CaF_2(Eu)$ crystal of module number #24 is contaminated with ~8 ppb for Th and ~0.5 ppb for U, which are 34 and 9 times of the results of ICPMS (see Table 2-1). And the contamination of ^{226}Ra is ~11 ppb. The same procedure can be applied for other modules and the major concern is especially devoted for the module number #7 in Fig. 7-2. Result of the fit for the module number#7 is 0.5 ppb for Th and 0.05 ppb for U and almost consistent of the result of ICPMS. Then it is found that

115

the contamination of U and Th is largely dependent on each crystal. It is suggested that impurities in a crystal have a tendency to be pushed away to the outside of an ingot on the process of crystal growth [84]. This non-uniformity is expected to be the result of which part in a ingot are cutting down.

The internal background of U and Th chains are confirmed by another signature. There are some characteristic decays in U and Th chains, which are listed in Table 7-1.

Table. 7-1 Characteristic decays in U and Th chains. The sequential decays of $\beta \to \alpha$, $\alpha \to \alpha$; Nuclei-1$\to$Nuclei-2 + particle-1 $\to$Nuclei-3 + particle-2.

Nuclei-1	Nuclei-2	Nuclei-3	particle-1	particle-2
Th-chain				
^{220}Rn	^{216}Po	^{212}Pb	6.288α	6.907α
55.6s	145ms	10.64h		
^{212}Bi	^{212}Po	^{208}Pb	2.25β	8.784α
60.6m	298ns	stable		
U-chain				
^{214}Bi	^{214}Po	^{210}Pb	$1.02,1.51\beta$	7.834α
19.9m	164μs	22.3y	3.26β	

These are special sequential $\beta \to \alpha$, $\alpha \to \alpha$ decays in both series with the short life time less than 1 sec. Therefore it is very interesting to identify such sequential decays to determine whether or not the origins of these prominent peaks appeared in the ultra-low background measurement, is truely due to the Th and U radioactive chains. Among three succeeding decays in Table 7-1, the second one with the life time of $T_{1/2}$=298 ns can not be measured in the ELEGANT VI data taking system, because the gate width of the trigger is 4 μs. Then the data taking system of ELEGANT VI is constructed to measure the first and the third one in Table 7-1.

1) delayed α-ray from ^{214}Po

The tactics of detecting these sequential decays is briefly discussed in the following. After being triggered by the particle-1, at this time the first gate is open with the width of 4 μs, if a sequential second signal is coming within 500 μs the second trigger is open with the width of 4 μs. The 500 μs is enough to detect the life time of 164 μs, because the residual fraction of ^{214}Po is about exp(-164/500)$\sim$ 0.05. This diagram of electronics is shown in the right dashed box of Fig. 2-12.

The energy spectrum triggered secondly within the 500 μs are shown in Fig. 7-4. It is found that only the module number #24, 21 and 5 have the prominent peaks due to the 164 μs delayed alpha from ^{214}Po. This is supported by the simulation

in the Fig. 7-3. In the Fig. 7-3 this delayed α from ^{214}Po did not come within the gate width, then there are no peaks around 1.6 MeV which is plotted by the calculation.

By using the time information of the delayed signal after triggered by the first gate, the decay rate of 164 μs can be obtained. However, the analysis is still in progress and this is not confirmed yet.
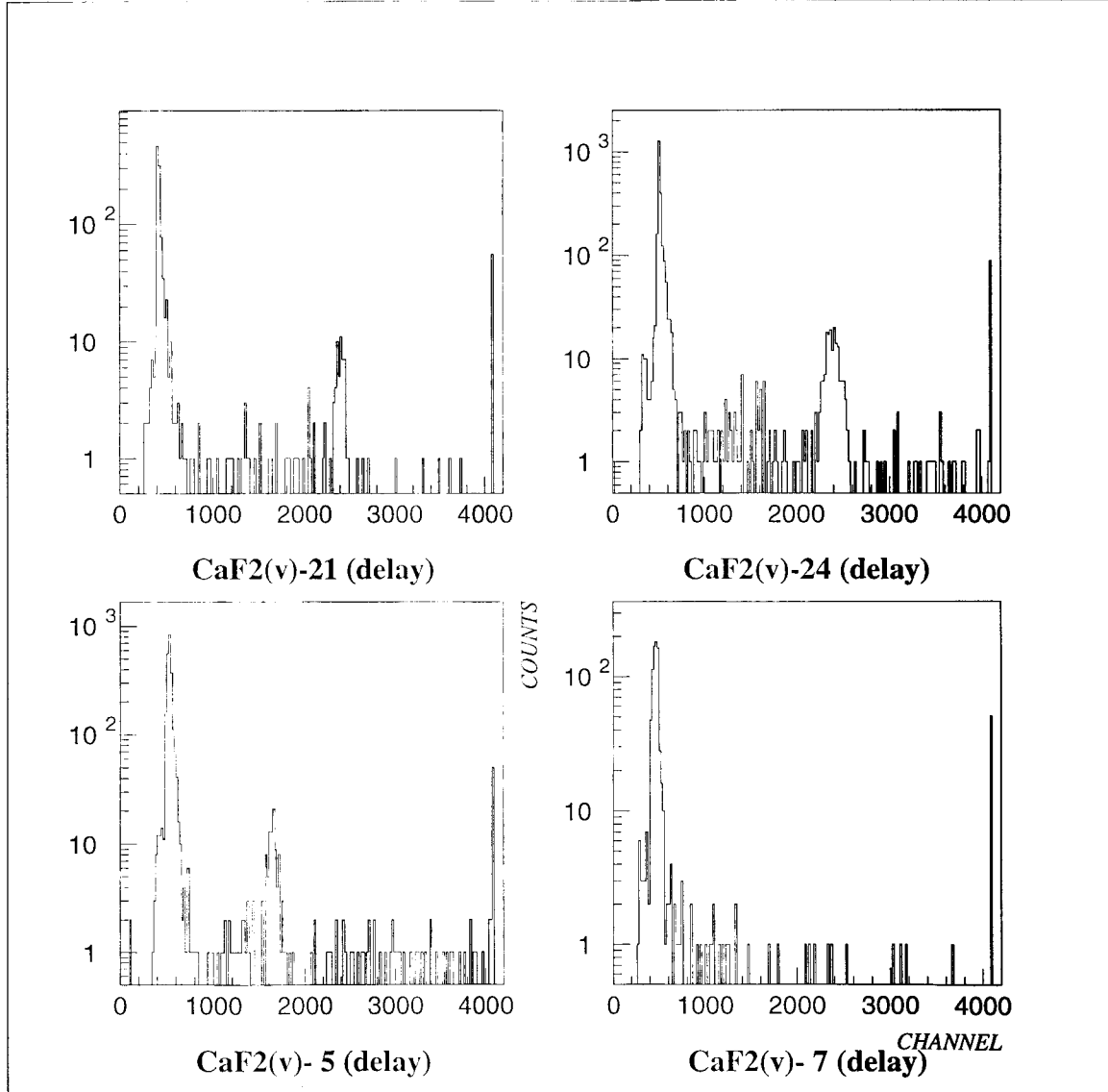
Fig. 7-4 The second triggered energy spectra of the module number#24, 21 and 5 in the RUN015-001 (the live time of 1.6 days) after the selection of (i) and (ii). These are compared with the module number#7.

117

2) delayed α-ray from ^{216}Po

The delayed alpha from ^{216}Po can be measured by the same procedure of (1). However, at this moment the trigger rate of the second gate is only 0.3 counts per second. It is noted here that up to the RUN014-011 the trigger rate of the second gate is about 10 cps and the ratio of 2nd/1st~12%, however, in these RUN, the fake events are dominated. Then we improved the second trigger to be the sum of all 25-CaF2 and raised the threshold level to 900 mV after the RUN015. As a result the second trigger rate is 0.3 cps and the ratio of 2nd/1st is only limited to 0.4%. Above these considerations this measurement is in the next stage.

Another feature of these measurements is the long half life of 164 μs and 145 ms compared with the data taking time. There are some long range TDCs such as LeCroy 4208(time range= ±8.3 ms) and 4204(time range= ±167ms), however, it is not practical to measure 145 ms. then we are using the 24 bit Scaler. If we use the clock signal of 10 MHz (100 ns) and 24 bit Scaler, we can measure the time range of ~1 sec.

Let us go back to the low energy region and consider the influence of these background from U and Th chains. Low energy gamma and beta rays in U and Th chains are listed in Table 7-2. Among these radioactive nuclei, ^{228}Ra and ^{210}Pb are the most likely cause. In the case of NaI(Tl) the large peak at 50 keV are observed and internal ^{210}Pb is suggested as the major background below 100 keV actually [16],[85], [19]. As for CaF$_2$(Eu) there are no prominent peaks below 100 keV and ^{210}Pb is not considered as the major contributor to the background. Then ^{228}Ra could be the major contributor in the internal background. ^{228}Ra decays inside the crystal via a β decay of end-point energy 15 keV followed by a 6.7 keV γ in coincidence, or via a β decay of end-point 39 keV, with branching ratios 60%, 40%, respectively. In order to identify the Th chain, measurement of the sequential decays of ^{216}Po is important. And the simulation of these low energy β and γ rays including all decay-chains is in progress on the assumption of the measured contamination of U and Th.

7.2.2 external backgrounds

At sea level, outside a laboratory, the cosmic rays consist of the following components, measured in particles/cm^2/1000s (NCRP Report, 1975);

Among these particles the major concern are muons and neutrons. At a sea level sites there are three main sources of neutrons.

a) neutrons from natural radioactivity (both (α, n) rections and fission neutrons from the natural U and Th in the surrounding concrete(rock).

118

Table 7-2 Low energy gamma and beta rays with the intensity over 10% in U and Th chains.

Nucleus	γ/β	Energy (keV)	Intensity(%)
Th chain			
^{232}Th	γ	59	23
^{228}Ra	β	39, 15	60, 40
	γ	6.7	100
^{228}Ac	$\gamma(+\beta)$	57.8	36
^{228}Th	γ	84.4	26.7
^{212}Bi	γ	39.9	24
U chain			
^{238}U	γ	49.5	23
^{234}U	γ	53.2	28
^{230}Th	γ	67.7	23.4
^{218}At	γ	53.2	90×0.02(1.8)
^{214}Pb	$\gamma(+\beta)$	53.2	1.1
^{210}Pb	β	61, 15	19, 81
	γ	46.5	81

Muons	19.1	Electrons	5.5	Protons	0.17	Pions	0.0013	**Neutrons**	**7.5**

b) neutrons in the hadronic component of the cosmic rays.

c) neutrons produced by cosmic ray muon interactions.

The estimated neutron production via muons in the lead shield becomes comparable at about 3 m.w.e. and is by far the most dominant source until at the depth of about 100 m.w.e.[86]. Hence, in the following muon induced backgrounds(c) are described in detail.

Negative muons slowing down in matter are finally captured by the Coulomb field of nucleus into a Bohr orbit forming a muonic atom. The muon cascades rapidly, $\approx 10^{-11}$ sec, down to the 1s level from which, through the weak interaction, it either decays

$$\mu^- \rightarrow e^- + \bar{\nu}_e + \nu_\mu \qquad (7.1)$$

or is captured by a proton of the nucleus (Z,A)

$$\mu^- + {}^A_Z X \rightarrow {}^A_{Z-1} X^* + \nu_\mu \qquad (7.2)$$

Nuclear muon capture is usually described within the inpulse approximation. In this approach the interaction between the muon and the nucleus is expressed by an effective hamiltonian which represents the contributions of the elementary process $\mu + p \rightarrow n + \nu_\mu$ summed over all protons in the nucleus. Decay is more probable in materials of low atomic number, but capture is dominating for high Z nuclei. For Z= 20, 80% of the negative muons are captured, and 95 % at Z= 50 (the decay ran from $\approx$ 3% in Pb to $\approx$ 40% in Al), which are listed in Table 7-3 [87].

Table 7-3 Isotopic abundances, nuclear mass(A) difference, muon binding energies (B_μ), total muon-disappearance rates (λ), and decay rates (λ_d).

Target	A	Abundance	Product nucleus	M(Z-1, A) -M(Z,A) (MeV)	B_μ (MeV)	$\lambda \times 10^{-5}$ (1/sec)	$\lambda_d \times 10^{-5}$ (1/sec)	λ_d/λ
$_{13}$Al	27	1.000	$_{12}$Mg	3.129	0.463	11.32	4.54	0.401
$_{14}$Si	28	0.922	$_{13}$Al	5.151	0.535	12.06	4.54	0.376
$_{20}$Ca	40	0.970	$_{19}$K	1.833	1.054	29.6	4.54	0.153
$_{26}$Fe	56	0.917	$_{25}$Mn	4.220	1.72	51.0	4.45	0.087
$_{47}$Ag	107	0.514	$_{46}$Pd	0.546	4.76	118.5	4.16	0.0351
$_{47}$Ag	109	0.486	$_{46}$Pd	1.624	4.76	118.5	4.16	0.0351
$_{53}$I	127	1.000	$_{52}$Te	1.200	5.80	116.1	4.13	0.0356
$_{79}$Au	197	1.000	$_{78}$Pt	1.26	10.10	145.8	3.8	0.0261
$_{82}$Pb	206	0.236	$_{81}$Tl	2.02	10.66	134.9	3.8	0.0282
$_{82}$Pb	207	0.226	$_{81}$Tl	1.953	10.66	134.9	3.8	0.0282
$_{82}$Pb	208	0.523	$_{81}$Tl	5.506	10.66	134.9	3.8	0.0282

The muon capture is a two-body process (μ^-, p). If the proton and muon are at rest, the neutron recoils with about 5.7 MeV of energy and the neutrino carries off the rest, about 100MeV. But since the capturing proton is in a nucleus, it has a momentum distribution. Hence a large momentum transfer is possible and the formed neutron can recoil with an energy larger than 5.7 MeV. This energy is comparable to the neutron binding energy and is typically of the order of 10 MeV. Two possibilities can be assumed: first, that the neutron escapes directly from the nucleus (direct neutron emission), and second (evaporation neutron emission), that this energy is shared between the other nucleons and a compound nucleus $_{Z-1}^{A}X^*$ is formed, whose excitation depends on the momentum distribution of the capturing proton.

1) evaporation component

The compound nucleus de-excites mostly by neutron emission. In fact, measurements of the neutron multiplicity give about 1.5 neutrons per muon capture, which

indicates that excitation energies are moderate, about 15 MeV. It is highly probable that γ-rays accompany the neutron emission, about 80% of the time a muon is captured [88] [89]. The emission of protons and charged particles in general occurs very infrequently, 2 % of the time for protons and 0.5 % for α. The evaporation neutrons follow a spectrum of the form.

$$dN(E) \approx (E/1MeV)^{5/11} exp(-E/\theta)dE (E < 4.5MeV) \qquad (7.3)$$

The nuclear temperature, θ, has been found to be 1.22±0.06 MeV for Pb.

2) direct component

As pointed out by Singer [90], the direct neutron emission following the muon capture is not negligible. The direct emission must be high for low A, a·exp(-b ·$A^{1/3}$), according to the calculations of Singer, where a and b are constant. This emission probability is about 0.22 per muon capture for silver target. The inclusive energy spectra have been measured for neutrons emitted after muon capture in O, Si, Ca and Pb by T. Kozlowski et. al. [91]. They are consistent with an exponential dependence on the neutron energy given by the expression

$$dN(E) \approx exp^{-E/T} \qquad (7.4)$$

The neutron yields and exponential constants T are deduced from the spectra in the energy range from 10 MeV to 50 MeV are compared to those of ref.[92],[93] in Table 7-4.

Table. 7-4 Neutron yield per calculated muon for 10 MeV threshold and the exponential constant resulting from a fit of the exponential N(E)=$N_0 e^{-E_n/T}$ to the neutron spectra in the energy range 10-50 MeV.

Nucleus	Yields for 10MeV threshold			T[MeV]		
	[91]	[92]	[93]	[91]	[92]	[93]
O	0.26			16		
Si	0.191	0.156		10.3	6.5	
Ca	0.112	0.114	0.102	9.5	6.6	14
Pb	0.106		0.091	8.6		12

The spectrum of neutrons emitted following muon capture for each component in lead and wax are shown in Fig. 7-5.
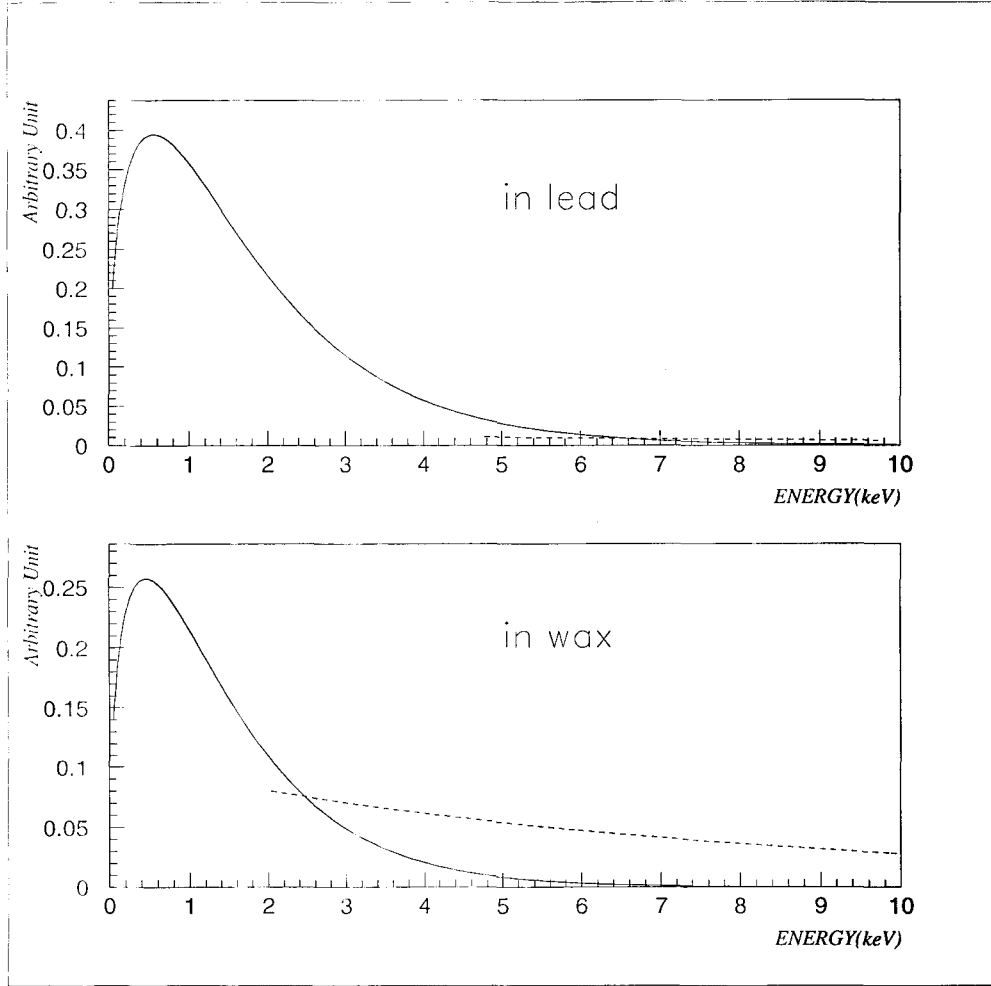
Fig. 7-5 The spectrum of neutrons emitted following muon capture for each component in lead and wax. The solid line is an evaporation component. The dashed line is an direct component. The direct emission is high for low A (wax).

The category (b) only contribute to the fast neutron flux. And the neutron yield from hadron cascades is approximately one half of the yield (at all energies) from muon interaction [94]. The spectrum of neutrons in cascades falls off as $\sim E^{-1/2}$ for energies between 10 and 50 MeV.

In Chapter 6.2.3 it is suggested that the cosmic ray induced neutrons have some contribution to the backgrounds. It is not possible to evaluate the effects of cosmic rays until the measurements are carried out at the sea-level. And an ultra-low background measurement makes it possible to reveal a small signature. Another signature originated in neutron background is observed in 'backgrounds search RUN', which is noted in Chapter 6.2.2.(b). Followings are the data of RUN099-001 which was triggered by 40 CsI(Tl)

122

detector.

RUN099-001 ;

Total Trigger rate of 40 CsI : 793cps (~20cps/1module)

Number of the acquired events : 4228778

Live time : 39109 seconds (~10.9 hours;Aug. 12-13)

Dead time : 45%

It is noted here that the RUN condition is the same as RUN014-004~-011 except triggered by CsI and no-LED. N_2 gas is introduced with an average input-flow of 240cc/min. The 4000ch full range of CsI(Tl) is about ~10 MeV and the threshold level is about 20 mV which corresponds ~300 keV.

The observed CsI(Tl) spectrum of module number #8 as one example is shown in Fig. 7-6, 7-7.
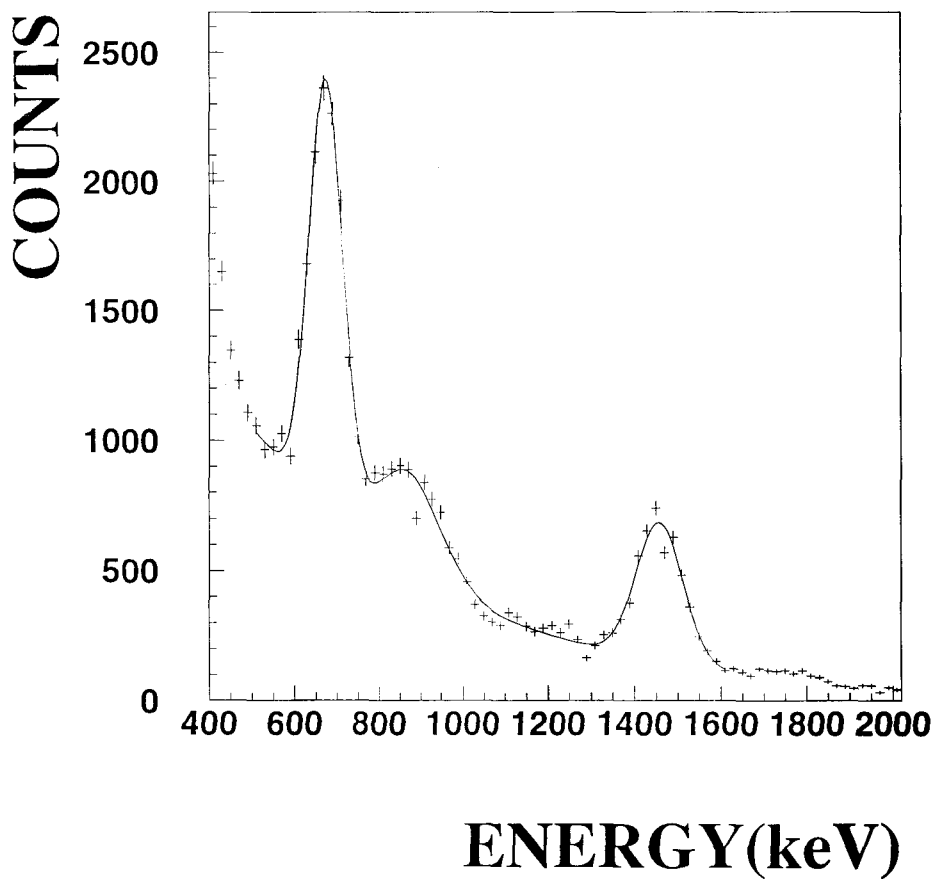
Fig. 7-6 CsI(Tl) energy spectra (400-2000 keV) of the module number#8 in the RUN099-001 (the live time of 10.9 hours) after the selection of multiplicity = 1. And energy was calibrated by the background peaks of ^{40}K (1461 keV) and ^{208}Tl (2614 keV)

ENERGY(keV)
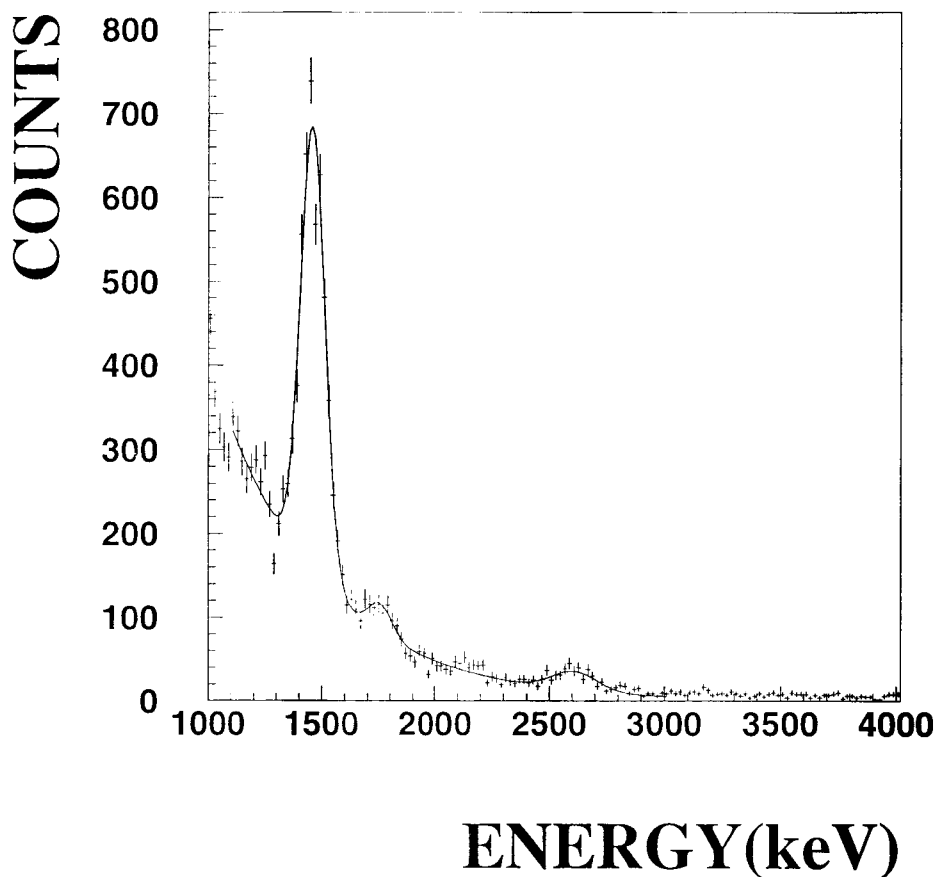
Fig. 7-7 CsI(Tl) energy spectra (1000-4000 keV) of the module number#8 in the RUN099-001 (the live time of 10.9 hours) after the selection of multiplicity = 1. And energy was calibrated by the background peaks of ^{40}K (1461 keV) and ^{208}Tl (2614 keV)

The following backgrounds are identified and listed in Table 7-5.

However, the peak around 670 keV and 850 keV are not explained by these backgrounds.

On the other hands, the background measurements of all materials of **ELEGANT VI** using a low background Ge detector (ELEGANT III) identified the following three peaks for CsI(Tl) crystal (Table 7-6).

Table 7-5 The major backgrounds observed in CsI(Tl) spectrum.

nuclei	energy (keV)		decay	intensity (%)
^{40}K	EC	1461		10.5
^{208}Tl	β	2614		
^{214}Bi	β	609		46.1
		768		4.9
		1120		15.0
		1238		5.9
		1764		15.9
		2204		5.0

Table 7-6 Identified peaks in the spectrum of CsI(Tl) crystal by using a low background Ge detector (ELEGANT III)

nuclei	life(yr)	energy (keV)	decay	intensity (%)	counts/h	Bq/kg
^{137}Cs	30	662	β	85	0.144±0.0337	
^{134}Cs	2.1	605	β	97.6	0.0567±0.0142	0.055
		796	β	85.4	0.0536±0.0146	

The natural abundance of ^{133}Cs is 100% and radiative capture cross section is 30.6 barn. The radioactivity in Table 7-6 is calculated by using this cross section on the assumption of the neutron flux with 1.74×10^{-3} n/cm^2/s at Osaka (sea level). The decay scheme of ^{134}Cs is shown in Fig. 7-8. These five γ-rays ($\gamma_{1\sim5}$) are attributed to the peaks around 670 keV and 850 keV in Fig. 7-6.
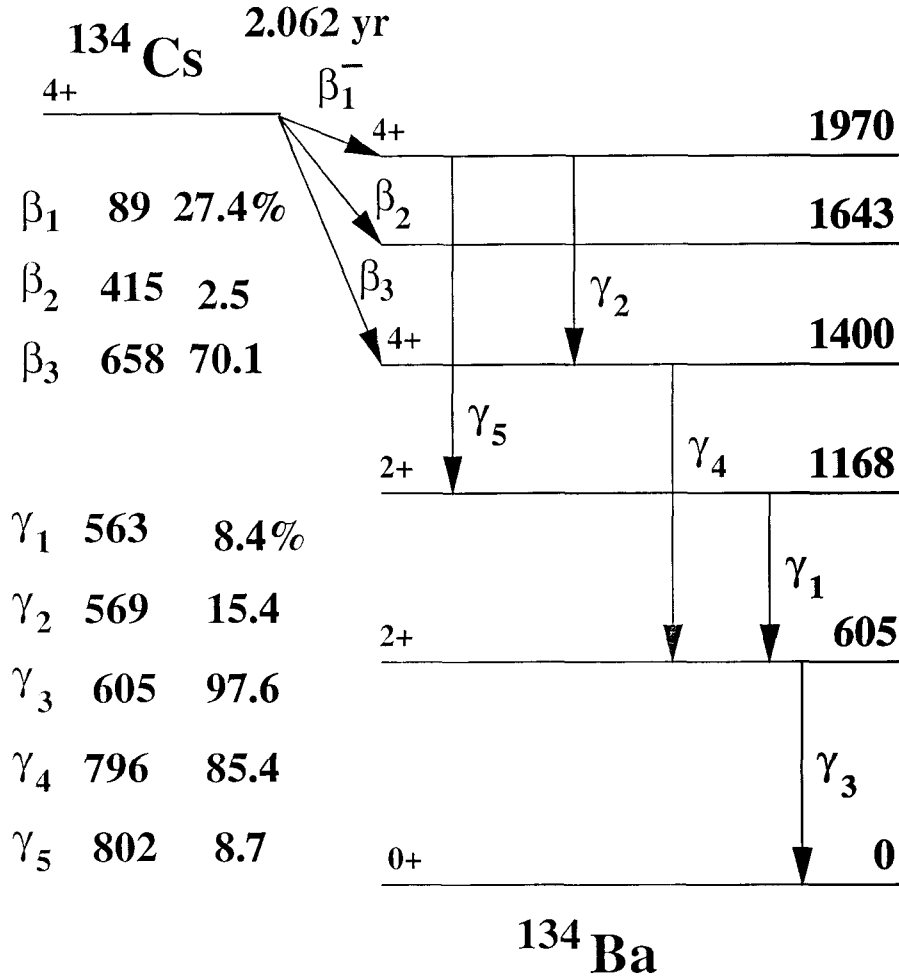
Fig. 7-8 The decay scheme of ^{134}Cs. Energies are given in units of keV.

These facts suggest that the cosmic ray induced background are not small and other lines are listed in Table 7-7 [86].

It is noted here that Eu; the activator of CaF_2, have a large radiative capture cross section. The features are summarized in Table 7-8.

The production rate of ^{152}Eu and ^{154}Eu in Table 7-8 is calculated by using the Eu mass fraction of 0.17% in CaF_2(Eu) crystal on the assumption of the neutron flux with 1.74×10^{-3} n/cm^2/s at Osaka (sea level). The prompt gamma radiation following radiative neutron capture is too energetic, since on the neutron capture process the mass difference of about $\sim$6 MeV is librated by prompt gamma rays. Then this high energy prompt gamma rays are vetoed by surrounding detectors. Hence delayed radioactivity from ^{152}Eu(^{154}Eu) could be a problem. The decay scheme of ^{152}Eu is shown in Fig. 7-8.

126

Table 7-7 Background lines induced by cosmic rays observed in shielded **Ge-detectors** at sea level shallow depth or underground. * denotes excited state of the **respective nuclide.**

Energy (keV)	Isotope(source)	Reaction
72.8	Pb X-rays	excited by muon-induced
75.0		electrons in Pb(also by ^{210}Pb
84.9		via its daughter ^{210}Bi)
87.4		
109.9	^{19*}F	^{19}F(n,n')
186.0	^{66}Cu	^{65}Cu(n,γ)
278.3	^{64*}Cu	^{63}Cu(n,γ), ^{65}Cu(n,2n)
511	β^+	muon-induced pair production
579.2	^{207*}Pb	^{207}Pb(n,n')
669.6	^{63*}Cu	^{63}Cu(n,n')
803.3	^{206*}Pb	^{206}Pb(n,n')
962.1	^{63*}Cu	^{63}Cu(n,n')
1063.6	^{207*}Pb	^{207}Pb(n,n')
1115.5	^{65*}Cu	^{65}Cu(n,n')
1327.0	^{63*}Cu	^{63}Cu(n,n')
1412.1	^{63*}Cu	^{63}Cu(n,n')
1481.7	^{65*}Cu	^{65}Cu(n,n')
1547	^{63*}Cu	^{63}Cu(n,n')
2223	^{2*}H	^{1}H(n,γ)

Table 7-8 The radiative capture cross sections of ^{151}Eu and ^{153}Eu.

Nucleus	Abundance(%)	σ_c	product	life(yr)	production rate (/day)	M(Z, A) -M(Z, A+1)
^{151}Eu	47.9	8700	^{152}Eu	13(9.3h)	1200	6.3 MeV
^{153}Eu	52.1	320	^{154}Eu	8.5(46m)	50	6.4 MeV

	^{152m}Eu	^{152}Eu
γ_1	344 2.4%	26.6%
γ_2	779	13.0
γ_3	122 7.2	28.4
ce	7.8	33.1
γ_4	245	7.5
γ_5	842 14.6	
γ_6	963 12.0	
γ_7	964	14.5
γ_8	1086	10.2
γ_9	867	4.2
γ_{10}	1112	13.6
γ_{11}	1408	20.9
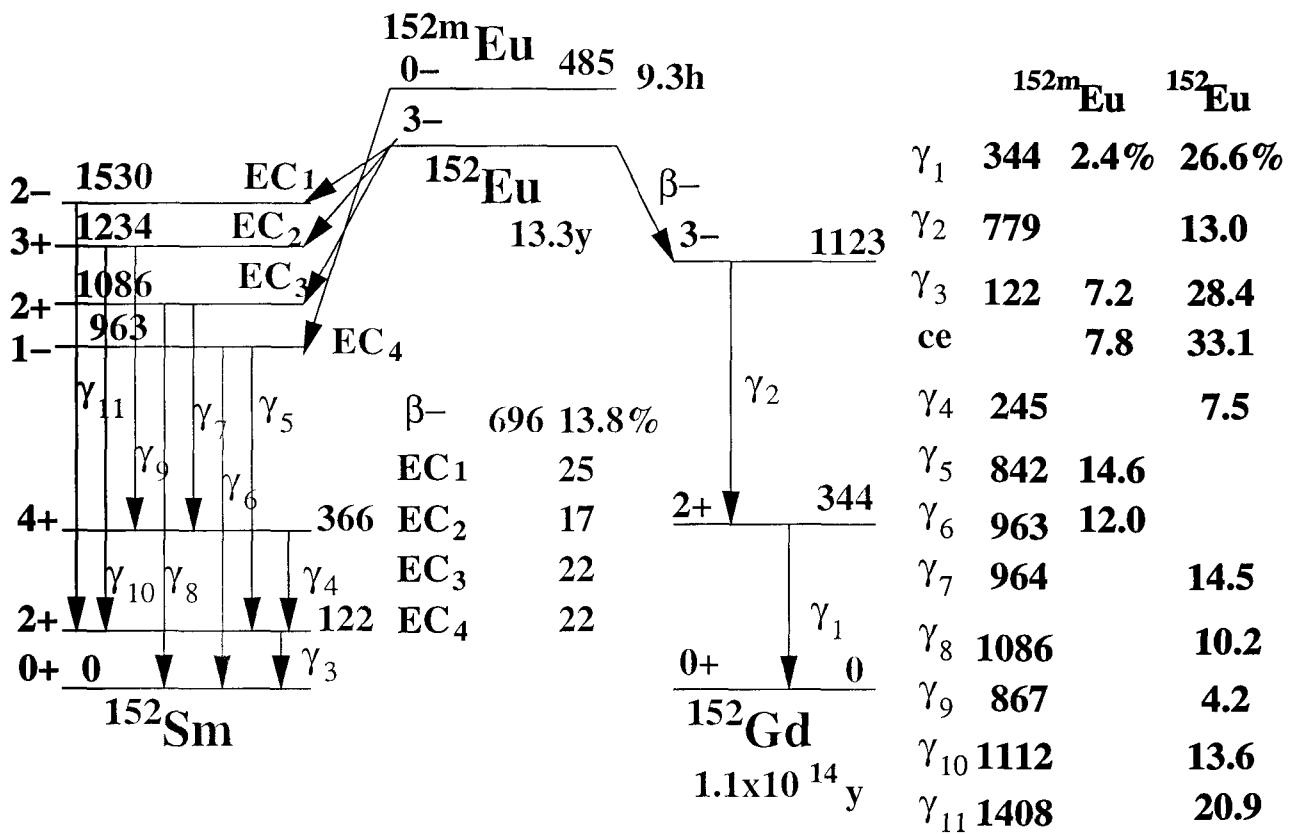
Fig. 7-9 The decay scheme of ^{152}Eu. Energies are given in units of keV.

Up to now there are no prominent peaks in CaF_2(Eu) spectrum except α peaks observed around 1 MeV. The internal conversion electron of 122 keV in Fig. 7-9 will be attributed to the low energy and further analysis are needed to evaluate.

Based on the above consideration, the reduction of cosmic-ray induced neutrons are mandatory at the sea level shallow depth site. However among cosmic ray induced neutrons the evaporation component, which is the majority especially for lead, are almost accompaning γ rays and can be vetoed by anti-coincidence. Then the direct component and the neutrons from hadronic cascades, which are almost fast neutrons should be cared at the sea level.

7.3 Full operation at the underground

The cosmic ray muon flux has both a slow, low energy component and a fast, high energy component, both of which contribute to neutron production. Slow negative muons can be captured to produce neutrons via $\mu^- + p \rightarrow n + \nu_\mu$. Fast muons can produce neutrons as a result of photonuclear (γ, n) or photo-fission (γ, Xn) from both real and virtual photons associated with the muons.

Beyond the depth of about 1000 m.w.e. the cosmic ray produced neutron flux would be less than 1 % of that from (α, n) reactions and fission in the surrounding rocks [86], which is listed in the previous Chapter 7.2.2 (a). In the following let us discuss the fission and (α, n) reactions.

All rocks contain some fraction of U and Th. The production rate depends on the concentration of U and Th present in the rock. Furthermore, the neutron flux that is present also depends on the neutron attenuation properties of the rock itself. The spectra of neutrons from fission and (α, n) reactions have similar shape. The energy spectrum of fission neutrons is represented by the semiempirical equation [95](Fig.7-10).

$$dN(E) \approx (E/1MeV)^{1/2} exp(-E/1.29MeV)dE \qquad (7.5)$$
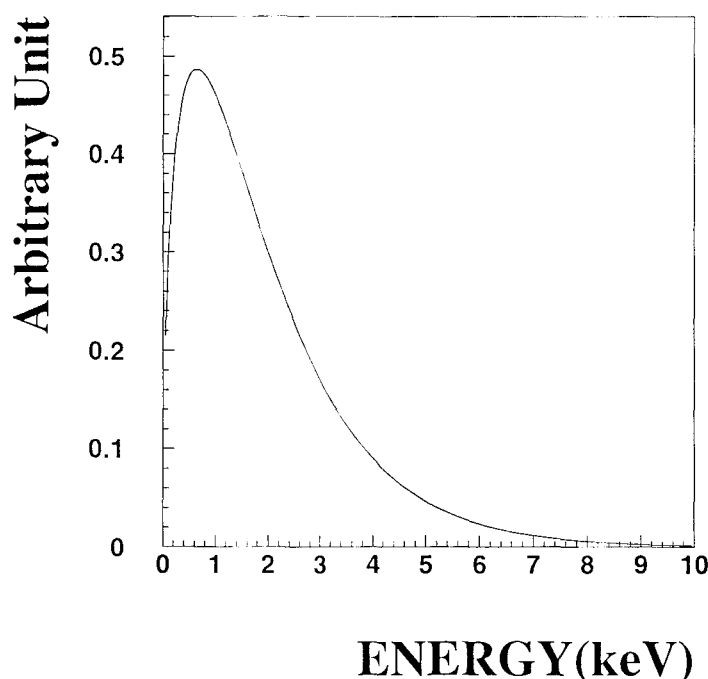
where E is the emitted neutron energy.

ENERGY(keV)

Fig. 7-10 The spectrum of fission neutrons.

129

To evaluate the neutron induced backgrounds quantitatively , the absolute neutron fluxes are needed not only outside the shield, but also inside the shield. Now these absolute neutron fluxes have been measured by using the Boron loaded liquid scintillator. BC-523A (BICRON) liquid scintillator contains boron enriched in ^{10}B to a minimum of 90 % (^{10}B content is 4.41 %). Neutrons that are sufficiently thermalized within the liquid scintillator are likely to undergo the ^{10}B(n, α) capture, which was describe in Chapter 2.3.3.(3). In order to achieve a better S/N ratio, the liquid scintillator is surrounded by four CsI(Tl) detector to get a coincidence with the excited γ ray (478 keV) following the first excited state of ^{7}Li. BC523 liquid scintillator which contains natural boron is also installed inside the CsI(Tl) detector to make a comparison. The measurement has been carried out not only at Osaka (sea level), but also at Oto (underground) with changing the shieldings.

The new underground laboratory "Oto Cosmo Observatory" [96] is constructed at the Tentsuji tunnel with 1200 m.w.e. (water equivalent depth). It is located 100 km south of Osaka. Background rates are very small, $4 \cdot 10^{-7}$/cm^2·sec for cosmic muons, $4 \cdot 10^{-5}$/cm^2·sec for neutrons, and 10 Bq/m^3 for Rn. And some features are listed in Table 7-9 compared with Osaka (sea level), Gran Sasso and Kamioka.

The neutron flux especially for fast neutrons is reduced by an order of two or three orders of magnitude from the Table 7-9. An outside veto shield with a high registration probability for the producing muon is effective in the background suppression of neutron event, especially at shallow depth with predominantly tertiary neutrons. A further reduction in event rate could be achieved by employing a muon veto since most of the neutrons produced by muon interactions are prompt. Hence in other words not only the reduction of hadronic component of the neutrons but also that of muon induced neutrons are expected in the underground. On the contrary to the sea level, a neutron shield is preferred to be placed outside the shields in the deep underground, where the neutron flux is dominated by fission and (α, n) reactions. A Rindi et. al. [99] reported that the measurement of thermal, epithermal and fast neutron flux performed in the Gran Sasso using a set of three large ^{3}He proportional counters. In Table 7-10 the ratios of the fluxes in the three regions are listed.

The neutron fluxes are dependent on the geomagnetic latitute and on the phase in the 11-year solar cycle. This is brought about through a magnetic modulation effect caused by solar plasma, consisting of trapped electrons and protons, moving radially from the sun to great distances. This phenomenon is related to solar eruptions and is inversely correlated to the 11 years period of solar sunspots. In addition to this, a decrease in the cosmic ray intensity that may amount up to 10 % occurs after a solar flare (Forbush effect). The total period of decreased intensity may last a few days,

---

^{12}The average density of the rock was taken as 2.7 g/cm^3 (1 m.w.e. = 100 g/cm^2)

^{13}Ca(27%), O(51%), C(12%), Mg(8%), Si(1%), Al, K, H (< 1%)

Table 7-9 Some features of Oto, Gran Sasso, Kamioka underground laboratory compared with Osaka(sea level).

	Gran Sasso[97]	Oto	Osaka	Kamioka
Rock overburden	3950m.w.e.	~1200[12]		3000
Minumum thickness	3150 g/cm^2		-	
Average thickness	3700 g/cm^2		-	
Mean density	2.71±0.05g/cm^3		-	
<Z>	11.4±0.2		-	
<A>	22.9±0.4		-	
Composition in rel. weight	13	-		
Total γ activity	1.8μRad/h			
Average Rn activity	40Bq/m^3	10		~10$^{2\sim3}$
Muons				
Flux	~1μ/h/m^2	14	~ 10^6	~7
Minimum energy at surface	~1.4TeV			
Mean energy at detector	240GeV			
Primary CR energy(single μ)	>3TeV			
Orimary CR energy(multiple μ)	>20TeV			
Neutron flux		(~0.1)	(~6)	
Thermal	0.0074n/cm^2/h		~5(Hongo)[98]	0.050
Epithermal	0.0046n/cm^2/h		~25(Hongo)	0.090
Fast	0.0092n/cm^2/h		~21(Hongo)	0.012

but full recovery sometimes takes several weeks. The flux fluctuations are quite large, especially for neutrons. Searching for annual modulations of WIMPs needs to minimize these neutron induced fluctuations. Hence the measurements are preferred to carried out at the underground and monitor these fluctuations.

ELEGANT VI will run within a few month at Oto Cosmo Observatory.

The following improvememts are in progress and applied at the underground RUN.

1) materials check by ELEGANT III

Now a low background Ge detector (ELEGANT III) has been used to measure the radioactive contamination of all the materials in ELEGANT VI. These measurements so far revealed that the following materials are highly comtaminated with U and Th chains [45].

i) Alminized Mylar[14] (Toyo metalizing)

ii) Teflon[15] (BICRON)

Table 7-10 Ratios of neutron flux.

	Thermal	Epithermal	Fast
Inside the tunnel	1	0.62	1.25
Outside the tunnel	1	5	4.1

iii) Cobar glass(alloy) in PMT(Hamamatsu H3178MOD)

Although a window material is Quartz, Cobar glass is used for a glass envelope to match the coefficient of thermal expansion between Quartz and Cobar. Quartz window is made from fused silica and this material transmits down to 160 nm and has advantage of low radioactive background with U and Th content less than 5ppb.

Among these materials Aluminized Mylar are replaced with a low background one and the used amount is reduced for Teflon.

2) complete water tank moderator

Only at deep locations, where the neutron flux is dominated by fission and (α, n) reactions, is a neutron shield best placed outside the conventional shieldings.

3) install the third trigger

As described at Chapter 7.2.1(2), the identification of the delayed alpha ray from ^{216}Po is required to evaluate the content of ^{228}Ra in the low energy region. It is expected that the total trigger rate is much reduced at the underground. This makes it possible to enlarge the trigger ratios of 2nd/1st and 3rd/1st and install the third trigger covering 145 ms time range.

4) muon veto by plastic

Although a muon flux is small and cosmic ray induced neutrons are much reduced at the underground, a further reduction will be expected by a veto.

---

[14]Mylar is a polyester film with the composition of $(C_{10}H_8O_4)_n$ and made by Dupont.
[15]Teflon is a Tetrafluoroethylene resin with the composition of $(CF_2)_n$ and made by Dupont.

Chapter 8

CONCLUDING REMARKS

1) A segmented inorganic low background scintillator-ensemble 'ELEGANT VI' has been developed to search for WIMPs by measuring elastic scattering from F nuclei in the CaF_2 scintillators and to study of the double beta decays of ^{48}Ca by using the naturally contents in the CaF_2, simultaneously. It consists of CaF_2 scintillator-complexes for energy and timing of recoil signal and β rays, surrounded by 4π active shield with active light guides and CsI(Tl) scintillators for γ and X rays. All the signals from these detectors are properly used for off-line event selections (cuts) and for evaluation of the background events, which are very crucial for selecting true signals and for rejecting background ones. This system has been developed especially for the background reduction in the low energy region. Since the background rate generally increase exponentially in the low energy due to summing all contributions not only from the Compton scattering of γ and the tails of β rays, but also from the electric noises. And it is not so clear compared with that of a few MeV region for the study of the double beta decays, and so on. The CaF_2 scintillator-complexes, which is unique of ELEGANT VI, is a key detector for selecting true recoil events from the huge background events in the low energy region.

2) The CaF_2 scintillator-complexes has been developed on the basis of new ideas. The central $CaF_2(Eu)$ crystal has light guide of pure CaF_2 crystal which are also sensitive to gamma rays. This design is quite effective to reduce the background from PMTs. Radioassay techniques have considerably advanced, especially in mass spectroscopy, making bulk analysis of all types of materials in parts per trillion (ppt) range feasible. However, the comtamination level of the lowest background glass

133

used for PMT is still in the range of a few 100 mBq/kg(ppb). Hence the care for the background from PMT side is mandatory. In the 'phoswich' case the event is separated by decay times (pulse shape:fast/slow), while in this CaF$_2$(Eu) & CaF$_2$(pure) case the event is separated by optical properties such as emission/transmittance of scintillation light. Then this is a new type of detector using different mechanism.

3) Thus the side crystals of CaF$_2$(pure) combines with the surrounding CsI(Tl) active modules are used as the 4π active shield. They are chosen to make active shield as hermetic as possible since no container is necessary due to nondeliquescence. Besides, the active veto is effective even for X-rays, which has been lossed in energy at housing in the case of NaI. And CaF$_2$ detectors are divided into small segments with dimension of 45mm cube, since true recoil event due to dark matter scattering is confined in a small region in space.

4) The linearity of CaF$_2$(Eu) scintillator in the low energy region below 100 keV is checked and the typical energy resolution as measured with the ^{241}Am 59.5keV γ ray is about $\triangle E/E = 25\%$(FWHM). The time resolution of CaF2(Eu) was measured to be 8 ns in FWHM at $\sim$1 MeV γ ray. As for CsI(Tl) scintillators, covering a large solid angle of 3.2π, 9.8 % FWHM energy resolution is achieved for ^{137}Cs 662 keV γ ray, which corresponds to the light detection efficiency of about 13 %.

5) In order to treat properly the low energy signal, high gain amplifiers with integration circuit and low noise discriminators have been developed. The signals from the two photomultipliers were separately discriminated at the level of one photoelectrons, which energy corresponds to 0.35 keV and circuit noise can be kept below 0.1 keV and then put in coincidence for triggering purposes. The efficiency of the low energy signal has been determined by using the signal from a light emitting diode(LED). It is found that the detector system is sensitive to 2keV signal with 38% and 23% efficiency for before and after roll-off selection, respectively. It is estimated that the light detection efficiency of CaF$_2$(Eu) is about 60 %.

6) The energy dependence of the scintillation efficiency produced in CaF$_2$(Eu) by recoiling calcium and fluorine recoils was measured in the 25-91 keV and 53-192 keV recoil energy intervals, respectively. The scintillation efficiency was found to be 11$\sim$ 20%, and 9$\sim$ 23% for F and Ca respectively. The scintillation efficiencies in CaF$_2$(Eu) crystal increase with decreasing recoil energy, which is firstly suggested by the measurement of Davies et $al.$. It is also suggested that the Eu doping appears to affect the efficiency for nuclear recoils.

7) As for passive shield, two independent systems has been installed. The first is a conventional photon attenuation shield of lead and copper. The second is unique

one and dedicated to shield for neutrons such as a Cd sheet, a paraffin loaded with LiH, and a water tank moderator loaded with H_3BO_3. In dark matter experiments searching for WIMPs, the nuclear recoil can be faked by neutrons. Sufficiently energetic neutrons and WIMPs both scatter elastically from a nucleus in the detector. then neutrons have the same signal signature and cannot be differentiated. It is critical, therefore, that the energetic neutron flux at the experimental site be minimized.

8) The total performance of ELEGANT VI has been studied at the Osaka University sea level laboratory. The complete passive shields and N_2 gas circulation for removing Rn gas in the air were used. It is emphasized that anti-veto is not so effective especially for the low energy region until the off-line veto are applied. An event is not vetoed from zero energy as long as using the hard-veto of any hardware such as discriminators and so on. And the roll-off selection is especially effective of the low energy region below ~200 keV. A run for 8.14 days, with ~7 cps/1 module of the trigger rate, leads to set similar limit as DAMA(BPRS) Collaboration at Gran Sasso underground laboratory on the upper limit of the spin coupled dark matters.

9) Measurements were carried out to examine the background level with changing the passive shields. The reduction ratio can be achieved to be about one order by using only the passive shield, and the paraffin loaded with LiH is especially effective about an factor~2. These measurements demonstrate that passive shielding, used for photon attenuation, act as a strong neutron source, with the neutrons being produced primarily by cosmic ray muon interactions within the shields. As a consequence, the shielding thickness of a detector should be chosen not thicker than necessary to absorb external gamma rays. Any additional high-Z material adds to the neutron producing target. Tertiary neutrons have an evaporation type spectrum and a high energy (direct) component, largely as a result of μ capture at this depth. To effectively absorb tertiary neutrons, the absorber, in this case the paraffin loaded with LiH, should be positioned inside the lead. The sea-level measurements makes it possible to evaluate the effect of these cosmic-ray induced background.

10) The high energy spectra of three CaF_2 detector shows the prominent α peaks around 1 MeV. The simulation of U and Th chains and delayed coincidence of sequential decays in U chain identify these peaks and lead to evaluate the contamination of U and Th. It is found that the level of contamination depends on each crystal. Some are thirty times for Th and ten times for U of the results of ICPMS (0.05 ppb for U and 0.24 ppb for Th). And in these three crystals ^{226}Ra is in out of equilibrium.

11) The neutron induced production of ^{134}Cs (the half-life is two years) is observed in CsI(Tl) crystal by the background spectrum of CsI detector and low background Ge detector (ELEGANT III). The activation component can only be avoided by placing the detector deep underground.

12) ELEGANT VI is installed within a few month at the new underground laboratory 'Oto Cosmo Observatory'. The neutron flux especially for fast neutrons is reduced by an order of two or three orders of magnitude. Only at deep locations, where the neutron flux is dominated by fission and (α, n) reactions, is a neutron shield best placed outside the conventional shieldings. Hence complete water tank moderator is planning to install. These improvements and continous running of more than one year with the LED and thermometer monitoring system will makes it possible to detect the signature of annual modulation, if it exsists.

In this kind of experiments the extremely low experimental rate requires an extremely low background, so that a large effort is needed to get such a goal.

Bibliography

[1] V. Trimble, Proc. First Int. Symp. Sources of Dark Matter in the Universe, ed. D. B. Cline, 1995, World Scientific

[2] M. Drees, hep-ph/9609300 (1996)

[3] T. P. Walker et. al., *Ap. J.*, **376**, 51 (1991); B. D. Fields and K. A. Olive, *Phys. Lett.*, B368, 103 (1996)

[4] K. A. Olive, astro-ph/9605068 (1996)

[5] B. Sadoulet, *Frontiers in Particle Physics: Carg èse 1994*, Plenum Press, New York, 1995

[6] B. Paczyński, *Astrophys. J.*. **304** 1 (1986); B. J. Carr, *Comm. Astrophys.*, **14**, 257 (1990); B. J. Carr, *Annu. Rev. Astron. Astrophys.*, **32**, 531 (1994); J. Shaham and A. Dekel, *Astron. Astrophys.*, **74**, 186 (1979); K. Griest, *Astrophys. J.*, **366** 412 (1991); R. J. Nemiroff, *Astron. Astrophys.* **247**, 73 (1991); A. De. Rujula, P. Jetzer and E. Masso, *Astron. Astrophys.*, **254**, 99 (1992)

[7] Y. Muraki, Proc. Conf. on Neutrino Physics at Hachimantai, Iwate, Japan, Oct 1997, RCNS-97-4(TOHOKU-HEP-97-03), p176

[8] B. Sadoulet, Proc. Int. Workshop on the Identification of Dark Matter(IDM'96), September 1996, Sheffield, UK, World Scientific, p235.

[9] F. De. Paolis, P. Jetzer and M. Roncadelli, *Phys. Rev. Lett.*, **74**, 14 (1995); D. Pfenniger, F. Combes and L. Martinet, *Astron. Astrophys.*, **285**, 79 (1994)

[10] J. Primack et al., *Phys. Rev. Lett.* **74**, 2160 (1995)

[11] S. D. M. White, C. S. Frenk and M. Davis, *Astrophys. J.*, **274**, L1-5 (1983)

[12] M. Spiro, *Frontiers in Particle Physics: Carg èse 1994*, Plenum Press, New York, 1995

[13] For reviews, see, e.g., M. S. Turner, *Phys. Rep.*, **197**, 67 (1990); G. G. Raffelt, *Phys. Rep.*, **198**, 1 (1990) An illuminating pedagogical discussion has also been given recently by P. Sikivie, *Phys. Today*, **49**, 22 (1996)

[14] G. Jungman, M. Kamionkowski and K. Griest, *Phys. Rep.* **267** 195(1996).

[15] M. Beck, *Phys. Lett.* **B336**, 141(1994)

[16] K. Fushimi et al., *Phys. Rev.* **C47**, R425 (1993)

[17] A. Watson, *Science*, **VOL. 275** March 21 1997, p1736

[18] A. K. Drukier, K. Freese and D. N. Spergel, *Phys. Rev.* **D33**, 3495 (**1986**); K. Freese, J. Frieman and A. Gould, *Phys. Rev.* **D37**, 3388 (1988)

[19] M. L. Sarsa et al., *Phys. Lett.* **B 386**, 458 (1996) ; *Phys. Rev.* **D 56, 1856 (1997)**

[20] K. Fushimi et al., Proc. 2nd RESCEU Int. Symp. on Dark Matter **in the Universe** and its Direct Detection, November 1996, Tokyo, Universal **Academy Press Inc.**, p115

[21] M. W. Goodman and E. Witten, *Phys. Rev.* **D31**, 3059(1985)

[22] J. Ellis, R. A. Flores and J. D. Lewin, *Phys. Lett.* **B 212**, 375(1988)

[23] H. Ejiri et al., *Phys. Lett.* **B317**, 14 (1993)

[24] P. Belli, *Phys. Lett.* **B387**, 222 (1996)

[25] S. Orito, Proc. Conf. on Neutrino Physics at Hachimantai, Iwate, **Japan, Oct 1997**, RCNS-97-4(TOHOKU-HEP-97-03), p211

[26] M. Mori et al, *Phys. Lett.* **B 289**, 463(1992); M. Mori et al, *Phys. Rev.* **D 48**, 5505(1993)

[27] J. Rich. Proc. Int. Workshop on the Identification of Dark Matter(IDM'96), **September** 1996, Sheffield, UK, World Scientific, p300.

[28] J. Ellis, Proc. Int. Workshop on the Identification of Dark Matter(IDM'96), **September** 1996, Sheffield, UK, World Scientific, p285.

[29] T. Numao, Proc. XIV Int. Conf. on Particles and Nuclei (PANIC'96), **CEBAF**, USA, May 1996, World Scientific, p80.

[30] S. Adler et al., *Phys. Rev. Lett.* **79**, 2204 (1997)

138

[31] M. Shiozawa, Proc. Conf. on Neutrino Physics at Hachimantai, **Iwate, Japan, Oct** 1997, RCNS-97-4(TOHOKU-HEP-97-03), p351

[32] J. R. Primack, D. Seckel and B. Sadoulet, *Anuu. Rev. Nucl. Sci.* **38**, 751(1988); **P. F.** Smith and J. D. Lewin, *Phys. Rep.*, **187**, 203 (1990)

[33] R. A. Flores *Phys. Lett.* **B215** , 73 (1988)

[34] E. I. Gates, G. Gyuk and M. S. Turner *Ap. J.* **449** , L123 (1995)

[35] J. D. Lewin and P. F. Smith, *Astroparticle Phys.* **6** 87(1996)

[36] F. Halzen and A. D. Martin, Quarks and Leptons, John Willey **and Sons, 1984**

[37] J. Ellis et al., *Nucl. Phys.* **B238** 453 (1984); B. A. Campbell et al., *Phys. Lett.* **173B** 270 (1986)

[38] J. Engel, S. Pittel and P. Vogel, *Int. J. Mod. Phys.* **E1** 1(1992).

[39] J. Ellis and M. Karlner, *Phys. Lett.* **B341** 397(1995)

[40] J. Ellis and R. A. Flores, *Nucl. Phys.* **B307**, 883(1988)

[41] J. Ellis and R. A. Flores, *Phys. Lett.* **B263**, 259(1991)

[42] A. Gould, *Ap. j.* **321**, 571(1987)

[43] M. Minowa et al.. Proc. of 2nd RESCEU Int. Symp. on "Dark Matter **in the Universe** and its Direct Detection", Univ. Academy Press, Tokyo, Japan, **1996, p77.**

[44] BPRS Collaboration, *Astroparticle Phys.* **2** 117(1994)

[45] S. Shiomi, Master thesis (1997).

[46] H. Ohsumi et al., Proc. of FRONTIER'96 , Osaka, Japan, **March 1996, World** Scientific, p274.

[47] P. Belli et al., Proc. Int. Workshop on the Identification of Dark **Matter(IDM'96),** September 1996, Sheffield, UK, World Scientific, p415.

[48] L. A. Hamel et al., Proc. Int. Workshop on IDM'96, September 1996, **Sheffield, UK,** World Scientific, p569.

[49] P. Belli et al., Proc. Int. Workshop on IDM'96, September 1996, **Sheffield, UK,** World Scientific, p563.

[50] T. Shutt et. al., *Phys. Rev. Lett.* **69**, 3425, 3531(1992)

[51] H. R. Philip and E. A. Taft, *J. Phys. Chem. Solids* **1** 159 (1965); **3 1 (1957)**

[52] P. Belli et al., *Nucl. Instr. and Meth.* **A336**, 336(1993)

[53] G. J. Davies et al., *Phys. Lett.* **B322** 159(1994)

[54] R. Hazama et al., Proc. Int. Workshop on the Identification **of Dark Mat-ter**(IDM'96), September 1996, Sheffield, UK, World Scientific, p397.

[55] N. J. C. Spooner et al., *Astroparticle Phys.* **5** 299(1996)

[56] D. Reusser et al.. *Phys. Lett.* **B255**, 143(1991

[57] G. J. Davies et al., *Phys. Lett.* **B320** 395(1994)

[58] Y. Messous, *Astroparticle Phys.* **3** 361(1995)

[59] H. Wang et al., Proc. Int. Workshop on IDM'96, September 1996, **Sheffield, UK,** World Scientific, p427.

[60] J. H. Hubbell, *Int. J. Appl. Radiat. Isot.* **33**, 1269 (1982)

[61] T. Kishimoto et al., OULNS Annual Report, 12(1993)

[62] N. Suzuki, Mater Thesis, Osaka Univ.(1996)

[63] H. Miyawaki et al., paper in preparation; Mater Thesis, Osaka Univ. **(1997)**

[64] G. Kunitomi, private communication (1996)

[65] R. Hazama et al., Proc. Weak and Electromag. Int. Nuclei (WEIN'95), **Osaka, June** 1995, World Scientific, p635.

[66] J. Menefee, C. F. Swinehart and E. W. O'Dell, IEEE Trans. **Nucl. Sci. 13, no. 1** 720(1966)

[67] M. Kobayashi et al., preprint (1994)

[68] R. Hazama et al., OULNS annual report, 11(1994)

[69] T. Mizuta, private communication (1994)

[70] See, e.g. J. B. Birks, Theory and practice of scintillation conuting **(Pergamon, Ox-ford**, 1964); W. H. Tait, Radiation detection (Butterworths, London, **1980); G. F.** Knoll, Radiation detection and measurement (Wiley, New York, **1979)**

[71] P. F. Smith et al., Phys. Lett. **B379** 299(1996).

[72] G. Gerbier, Proc. Int. Workshop on IDM'96, September 1996, Sheffield, **UK, World** Scientific, p378.

[73] Y. Nagai, M. Igashira, K. Takeda, N. Mukai, F. Uesawa, S. Motoyama, **H. Kitazawa,** and T. Fukuda., *Astrophys. J.* **372** 683(1991)

[74] W. R. Burrus and V. V. Verbinski, *Nucl. Instr. and Meth.* **67** 181**(1969)**

[75] C. M. Bartle and P. A. Quin, *Nucl. Phys.* **A216** 90(1973)

[76] R. B. Murray and A. Meyer, Phys. Rev. **122** 815(1961)

[77] R. Hazama et al., Proc. XIV Int. Conf. on Particles and Nuclei (PANIC'96), **CEBAF,** USA, May 1996, World Scientific, p477.

[78] H. Ejiri et al., Proc. Int. Workshop on Aspects of Dark Matter in **Astro- and Particle** Physics, September 1996, Heidelberg, Germany, World Scientific, **in press.**

[79] T. Kishimoto et al., Proc. 2nd RESCEU Int. Symp. on Dark Matter **in the Universe** and its Direct Detection, November 1996, Tokyo, Universal **Academy Press Inc.,** p71.

[80] A. Da Silva et al., *Nucl. Instr. and Meth.* **A354,** 553(1995)

[81] DAMA Collaboration, Astroparticle Phys. **7** 73(1997)

[82] R. Hazama, Master Thesis, Osaka University (1994)

[83] U. Kilgus and R. Kotthaus, MPI-PhE/95-09 preprint April (1995)

[84] T. Konishi (OKEN), private communication (1994); C. M. Rozsa (**BICRON), private** communication (1995)

[85] J. J. Quenby et al., *Phys. Lett.* **B351** 70(1995)

[86] G. Heusser, *Nucl. Instr. and Meth.* **B83** 223(1993); *Annu. Rev. Nucl. Part. Sci.* **45** 543(1995)

[87] B. Macdonald et al., *Phys. Rev.* **139** B1253(1965)

[88] G. Backenstoss et al., *Nucl. Phys.* **A162** 541(1971)

[89] S. Charalambus, *Nucl. Phys.* **A166** 145(1971)

[90] P. Singer, *Phys. Rev.* **124** 1602(1961)

[91] T. Kozlowski et al., *Nucl. Phys.* **A436** 717(1985)

[92] R. M. Sundelin and R. M. Edelstein, *Phys. Rev.* **C7** 1037(1973)

[93] M H. Krieger, thesis, Columbia Univerity (1969)

[94] M. Chen, V. M. Novikov and B. L. Dougherty, *Nucl. Instr. and Meth.* **A336** 232(1993)

[95] E. Segrè, Nuclei and Particles, 2nd ed. (Benjamin and Cummings, **Massachusetts,** 1977)p. 586.

[96] H. Ohsumi, et al., Proceeding of FRONTIER'96, Osaka, March **1996, World Scientific,** p274.

[97] M. Fujiwara, MACRO(Michigan Univ.) private communication **(1996)**

[98] K. Otani, Master Thesis, University of Tokyo (1994)

[99] A. Rindi, *Nucl. Instr. and Meth.* **A272** 871(1988)